

Third Sound Resonance Detection of Two Dimensional Superfluid Circulation

by

Hai Luo

A dissertation submitted in partial fulfillment of the requirements
for the degree of Doctor of Philosophy
at Wesleyan University
Middletown, Connecticut
1992

CONTENTS

Acknowledgement

Chapter 1. Introduction.

- 1.1 Helium.
- 1.2 Superfluid helium - 4.
- 1.3 Superfluid helium films.
- 1.4 Rotation of superfluid.
- 1.5 Superfluid circulation and quantization.

Chapter 2. The Third Sound.

- 2.1 The two fluid model.
- 2.2 Propagation of sound waves in helium II.
- 2.3 Third sound theory and experiment.
- 2.4 Discussion of results.
- 2.5 Solution for 2 - D circular third sound resonator.

Chapter 3. The Frequency Splitting.

- 3.1 Circulation splitting of a third sound resonator.
- 3.2 Geometric asymmetry splitting.
- 3.3 Total splitting.
- 3.4 Discussion.

Chapter 4. The Rotational Drive Third Sound Resonator.

- 4.1 Introduction.
- 4.2 Calculation of the general responses of the third sound resonator.
- 4.3 Calculation for the rotational drive third sound resonator.

Chapter 5. The Experimental Apparatus.

- 5.1 The refrigeration system.
- 5.2 The cell chamber.
- 5.3 The third sound resonator.
- 5.4 The tunnel diode oscillator.
- 5.5 The phase lock loop.
- 5.6 The detection system of third sound signal.

Chapter 6. Results and Discussion

- 6.1 Results from non - rotational drive technique.
- 6.2 Results for rotational drive technique.
- 6.3 The change of circulation.
- 6.4 Quantization.

Summary

Appendix

- A. Modes configuration of third sound resonator.

- B. The procedure for making a third sound resonator.
- C. Calculation of capacitance change due to the film oscillations.
- D. Calculation of the splitting due to the Doppler shift.
- E. Data taking and fitting program.

References

Acknowledgment

I would like to make a special thanks to my mentor and graduate advisor, Dr. Fred M. Ellis, for his guidance and encouragement throughout my graduate career at Wesleyan, for his critical reading of my thesis and correcting my overwhelming English mistakes.

I would like to thank Dr. Ralph Baierlein, member of my committee, who make a great contribution to this thesis, correcting part of the calculations which reported in appendix D, checking all other calculations and also critical reading this thesis.

I would like to thank Dr. Robert Rollefson, member of my committee, who had to read what I wrote, listen to what I said, and shown his concern to my work.

I would like to thank Dr. Thomas Morgan and Dr. John McIntosh, who always had words of encouragement and shown their support.

I would like to thank Paul Henkiel, David W. Bradley, who spent a lot of time to read my thesis and make a correction.

I wish to express my warmest appreciation to all the members of the Department of Physics, especially the physics office staff, Ana Pirruccio and Anne Stevenson. They always give me a smiling whenever I have any trouble. Thanks also goes to my friend Liping Li, who spent a lot of time to help me analyse the experimental data.

Finally, a special thanks to my wife, Qian He, who stood behind me and encouraged me to achieve my career goal, especially during my final year, who cooked for me everyday, took care of Kevin by herself. Without her support, I could not have completed my thesis. I also have a special thanks to my parents for their unwavering love and support.

Chapter 1 Introduction

This chapter presents a brief introduction of helium, superfluid helium and its physical properties. It also gives some general discussions of superfluid films in order to give some background in this field. More details of this chapter can be found in references at the end of this paper.

1.1 Helium

The helium atom is a particularly simple, stable and symmetrical structure. The nucleus contains two protons and two neutrons and has no resultant momentum or magnetic moment. Helium is the only element which remains in a liquid state near absolute zero. The first successful liquefaction of helium was accomplished by Kamerlingh Onnes(1908). Solid helium cannot be made merely by reducing the temperature of the liquid, but a pressure of 25 atmospheres must also be applied. The cause of this phenomenon is easily understood. Researchers like Simon (1934) have shown that this is a consequence of the large zero-point energy of the liquid and the quantum effects.

Fig.1.1 shows the phase diagram of helium-4 in the PT plane [1.1]. The ordinary triple point between the solid, liquid and gaseous phases does not exist for helium, but there exist two other triple points at the ends of the λ -line which separates liquid helium I from liquid helium II. Liquid He II is called "superfluid " and the other "normal fluid". Helium-4 in the superfluid phase displays many interesting properties which physicists have studied for about 90 years.

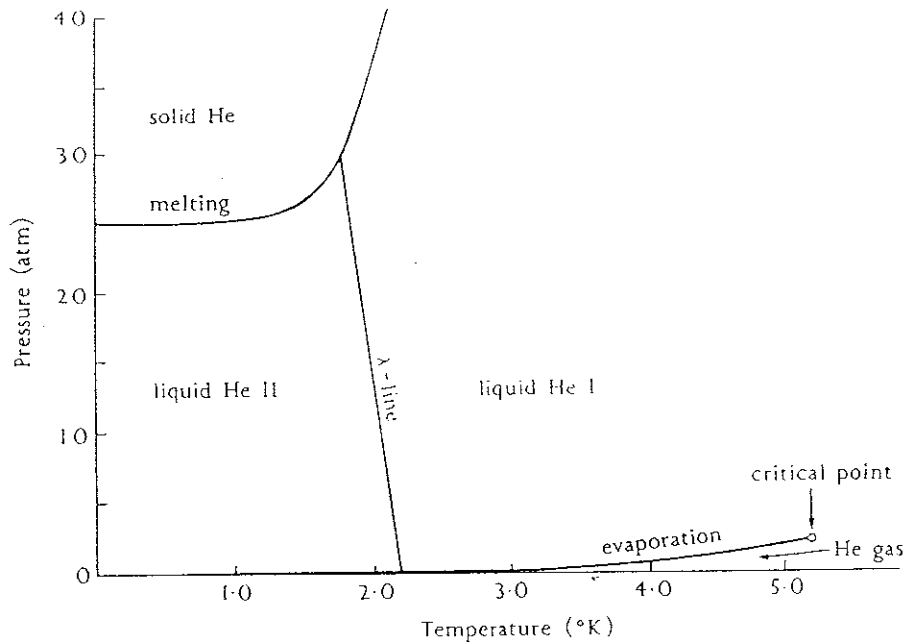


Fig. 1.1 The four states of ^4He in the $P - T$ plane. The λ -line at zero pressure is 2.17 K.

1.2 Superfluid Helium-4

The most remarkable of the properties of liquid He II is its "superfluidity", which was discovered simultaneously by Kapitza and by Allen and Misener (1938). The experimental results show that helium flow through a fine channel does not show any pressure difference between the two ends. This implies that helium has no viscosity in the liquid He II phase ($\eta < 10^{-11}$ poise) [1.2]. This is just like the superconducting phase in metal where electrons move freely, here helium atoms flow freely.

The other properties of He II include the λ shaped heat capacity (see Fig. 1.2) [1.3] and thermomechanical effect. In the former, a peak was observed at the vicinity 2.17K. The shape of the specific heat versus

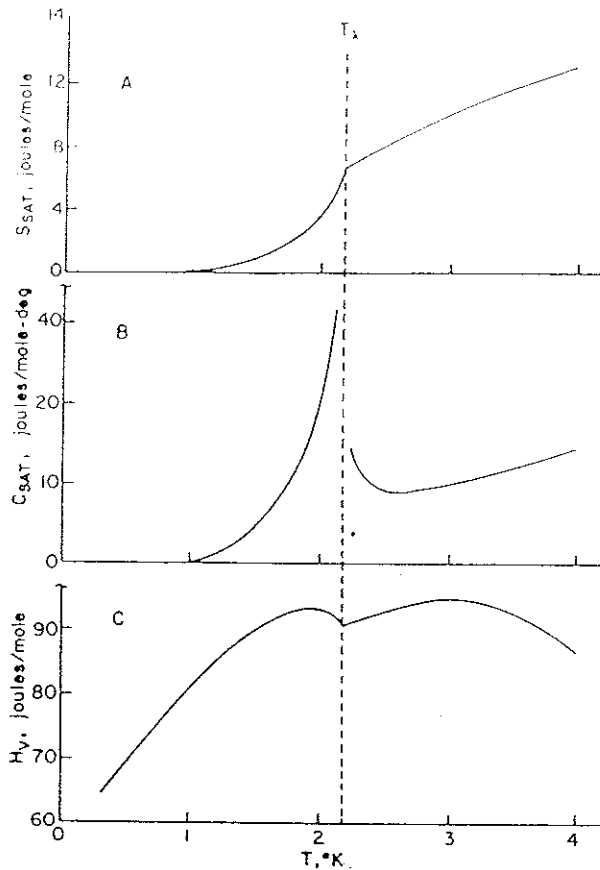


Fig. 1.2 Some thermal properties of liquid helium - 4 along the saturation curve. (a) Entropy; (b) specific heat; and (c) heat of vaporization.

temperature curve resembles the shape of the letter λ and therefore the singular point at this curve is called λ - point. At the λ - point no latent heat, characteristic of a first - order phase transition, was observed. This result was indirectly verified by a wide variety of experiments.

Thermomechanical effect, or Fountain effect, was first observed in 1938 by Allen and Jones [1.4]. Thermomechanical effect is a rise above the bath level of the fluid in a closed capillary which is heated at the open end. For large heat flux, the fluid drops due to increased vapor pressure. For small heat flux, however, the fluid rises above the level of the fluid in the bath. A more

dramatic effect can be seen if the capillary is open at both ends. When the lower end is heated, as by incident radiation, the fluid flows up and out of the other open end, producing a fountain of fluid.

The experimental results shown above give a clear picture that helium II must have some microscopic structure which is different from ordinary liquid, and that quantum mechanics must be considered in the study of helium II.

1.3 Superfluid Helium Films

One of the most spectacular transport properties of liquid helium II was first noticed in 1922 by Kamerlingh Onnens, but not properly identified until nearly 15 years later by Rollin and Simon. This observation was essentially that if an open container is partially immersed in a bath of helium II so that the liquid levels inside and outside the container are initially different, then the two levels equilibrate surprisingly rapidly. This phenomenon is illustrated in Fig. 1.3 for the two possible types of initial conditions.

This means that any solid surface in contact with helium-4 bath will form a helium film, typically about 100 atoms or 30 nm thick. The property of the film which has been of chief interest is its thickness, d , as a function of height above the bulk liquid level and of temperature. Measurements of film thickness, primarily by Jackson and co-workers, have given the following results: In the helium II region, d decreases with H , the height of the film above the liquid surface, according to the relation :

$$d \equiv \left(\frac{\alpha}{gH} \right)^{\frac{1}{n}} \quad (1.1)$$

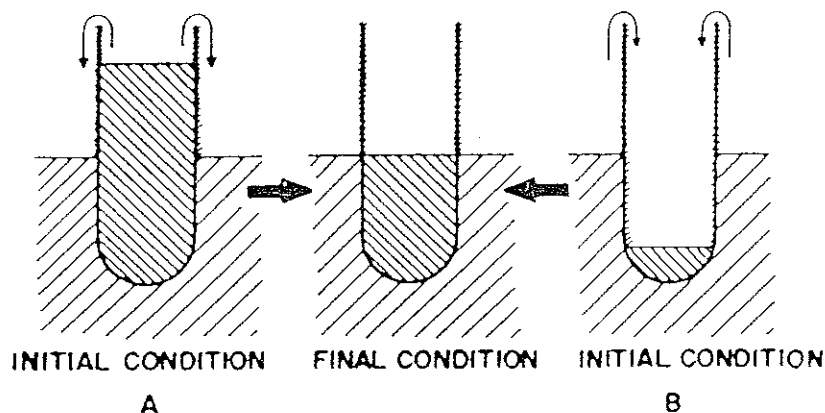


Fig. 1.3 Flow of the mobile He II film in (A) emptying and (B) filling a beaker.

where index n would vary from 3 in very thin films ($d = 1 \text{ nm}$) to 4 in thick films ($d = 30 \text{ nm}$), α being a constant whose value is determined by the material of the wall. The van der Waals forces were dominate in this case since all other forces are small. The conclusion is that helium films can creep anywhere in the superfluid helium II phase.

The property of the film described above gives us a chance to stabilize the film by building a large surface reservoir in a sealed container with a filling line. In this circumstance, a little disturbance like a very small temperature change can not make a big difference inside of third sound resonator. This technique has been used in our experiment to form very stable thin helium films.

The measurement of film thickness is not easy although the definition

of film thickness is quite simple, which is :

$$d = \frac{\text{Volume}}{\text{Area}}$$

This, however, is for the perfectly flat reservoir. The surface of the reservoir always has some capillarity and microscopically. In our resonator, the van der Waals constant must be determined to find the film thickness. The theoretical calculation of this constant with different substrates have been done by Zaremba and Kohn in 1976 [1.5] . Direct measurements of van der Waals constants show that some have a good agreement with theory and some do not [1.6] . Our measurement of the van der Waals constant was in slight disagreement with the theory and previous work done by P. Leiderer (private communication). An accurate knowledge of the film thickness still remains a problem.

1.4 Rotation of Superfluid.

When the two fluid model of helium II was first suggested, it was generally believed that it would be rather difficult to set the superfluid fraction into rotation because superfluid flow was characterized by the irrotationality condition introduced by Landau [1.7]

$$\vec{\nabla} \times \vec{V}_s = 0 \quad (1.2)$$

To see how the above result comes about, we introduce the circulation, which is defined as the integral:

$$\oint \vec{V} \cdot d\vec{l} \quad (1.3)$$

taken over any closed circuit in a fluid. According to Stoke's law, the circulation around any infinitesimal circuit in a liquid may be written as an integral over the surface \vec{S} enclosed by the contour :

$$\oint_L \vec{V} \cdot d\vec{l} = \oiint_s (\vec{\nabla} \times \vec{V}) \cdot d\vec{S} \quad (1.4)$$

and, combining equations (1.2) and (1.4) , we find

$$\kappa = \oint_L \vec{V}_s \cdot d\vec{l} = 0 \quad (1.5)$$

indicating that the circulation for any contour in the continuous field is zero. This condition of zero circulation can only be satisfied if \vec{v}_s vanishes everywhere. However, several experiments have shown that the whole mass of helium II in a bucket can be set into a state of uniform rotation[1.1]. The rotation of the superfluid can be satisfactorily explained by assuming that it is threaded by a series of parallel straight vortex lines. Contours which enclose a solid obstacle or a vortex core can yield a quantized circulation,

$$\kappa = \oint_L \vec{V}_s \cdot d\vec{l} = \oiint_s (\vec{\nabla} \times \vec{V}_s) \cdot d\vec{S} = \frac{n h}{m_4} \quad (1.6)$$

where n is integer, h the Plank constant and m_4 the mass of helium-4.

1.5 Superfluid Circulation and Quantization.

Two experiments strongly suggest that the circulation in helium II is quantized. In the first, by Vinen [1.8], the helium was contained within a

vertical tube, along the axis of which was stretched a fine metal wire. For a perfectly uniform wire, in the absence of circulation, the modes of vibration of the wire are doubly degenerate. If, however, there is a circulation κ around the wire, the associated Magnus force [1.9] will remove the degeneracy, and the wire vibration in two circularly polarized modes differing in frequency can be detected.

Following Vinen, a similar experiment has been made by Whitmore and Zimmermann [1.10]. They show clearly that in a multiply connected region, helium II not only can have circulation but is also quantized.

The fact that bulk superfluid helium - 4 in a superleak could be set into a persistent flow was demonstrated by Mehl and Zimmerman [1.11] and Reppy and Depatie [1.12]. A few years later, persistent bulk flows were confirmed by Van Alphen et al. [1.13] using a different technique. The first observation of persistent flow in a helium film was made on an unsaturated films by Henkal et al. [1.14]. Persistent currents in saturated films have proven to be more elusive. Wagner has reported a failure to observe persistent saturated and unsaturated film currents in his specific geometry [1.15]. This was not without precedent, since Wang and Rudnick have previously reported a failure to observe persistent unsaturated film currents in a specific geometry [1.16]. Several years later, Kim and Glaberson have also claimed they were unable to observe rotation induced persistent currents in a circular third sound resonant cavity [1.17]. Although some groups have reported that they observed persistent currents in helium - 4 films, no one has previously made an observation of persistent currents in any third sound resonator. We have made a successful measurement of circulation of superfluid film in a circular cavity third sound resonator using a rotational drive technique. The primary reason we built this system was to try to detect a single quanta of two dimensional superfluid circulation around the center hole of the resonator. This is actually following Vinen's experiment in

which he found a single quanta of superfluid circulation around a fine wire in bulk liquid helium II [1.18]. Later on, we have utilized this technique to estimate the distribution of vortices and the effect of geometrical asymmetry to the total mode splitting.

This thesis has overviewed almost all former works on superfluid helium films and established our own theory and experimental system on a rotational drive third sound resonator. Chapter 2 introduces the basic ideas of this work. Chapter 3 gives the details of mode splitting mechanisms and some calculations on how the detection system should behave. Chapter 4 presents a calculation of rotational drive technique and gives the theoretical prediction of experimental results. Chapter 5 describes the experimental set up and, finally, chapter 6, discusses experimental results. The experimental results are exactly what I anticipated in the theory.

Chapter 2 Third Sound

This chapter introduces the two - fluid model, the important postulate which explains almost all phenomena for liquid helium. The next section is about the propagation of sound waves in liquid helium II. Finally, the theory of third sound will be derived from the equations of motion of liquid helium. The early experiments of third sound are also discussed here.

2.1 The Two - Fluid Model

Many properties of helium II have already been introduced in chapter 1. All those can be understood in term of the two - fluid model. This was first proposed by Tisza [2.1] on the basis of London's application of Bose - Einstein condensation to helium- 4 . The basic two-fluid equations of motion were originally put forward by Landau [2.2] . The two - fluid model postulates that liquid helium II behaves as if it were a mixture of two fluids freely intermingling with each other without any viscous interaction. These two fluids are termed the normal fluid and the superfluid, and have densities ρ_n and ρ_s such that

$$\rho_n + \rho_s = \rho \quad (2.1)$$

where ρ is the ordinary density of liquid helium. The normal density ρ_n is a function of temperature, and increases from zero at absolute zero, to the value ρ at the lambda point. Conversely, the superfluid density is zero at the lambda point and increases to the value ρ at low temperatures. This is illustrated in Fig. 2.1 as the ratio of these densities. Note that the liquid is almost entirely superfluid below 1 K [2.3]. London noted that the ideal

Bose gas Bose - Einstein condensation transition temperature (3.12K) was remarkably close to the superfluid transition temperature (2.17K) in helium-4 and suggested that the superfluid component was the Bose condensation. [2.4]. The normal fluid, then, is a gas of quasipartical excitations in the helium-4.

In addition, the model also postulated that superfluid carries zero entropy, and has no resistance whatever to its flow. The essential parameters of the model are shown in the following table,

Normal fluid	ρ_n	$\eta = \eta_n$	$S_n = S_{lk}$
Superfluid	ρ_s	$\eta = 0$	$S_s = 0$

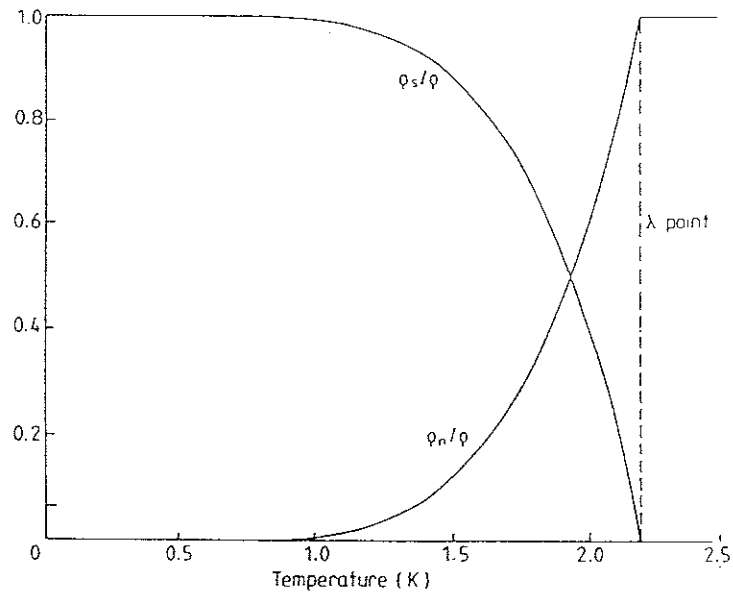


Fig. 2.1 Andronikashvili's experimental result for the ratio of fluid density versus temperature.

where η is viscosity. Although the two-fluid model is phenomenological, its equations of motion have been extremely successful in providing explanation for the remarkable properties of helium-4.

2.2 Propagation of Sound Waves in Helium -4

Liquid helium is capable of supporting several sorts of waves motion. In order to simplify notation applicable to the various modes, all are called "sound" but are differentiated by a numerical prefix. Thus, the an ordinary acoustic waves -- is called "first sound", with a velocity C_1 given by:

$$C_1^2 = \left(\frac{\partial P}{\partial \rho} \right)_s \quad (2.2)$$

It is characterized by a density oscillation at approximately constant entropy with the two fluids moving together. The first measurement was made by Findlay, Pitt, Grayson - Smith and Wilhelm [2.5] using a standing wave technique.

Second sound -- an oscillation of the superfluid fraction with respect to the normal fraction makes this wave a temperature wave, propagates at almost constant total density , and is given by

$$C_2^2 = \frac{\rho_s}{\rho} \frac{TS^2}{C_p} \quad (2.3)$$

The two fluids move in antiphase in order to keep the net flow of mass at zero [2.6]. Second sound in helium II was observed first by Peshkov in 1944.

Atkins predicted the existence of two more propagating waves modes in helium II [2.7] , third sound and fourth sound. We start to describe

fourth sound first because it is closely related to the first and second sound. Fourth sound is a pressure wave in helium II inside a porous medium where the normal component is viscosity locked to the substrate and only the superfluid is in motion.

The velocity of fourth sound is given by :

$$C_4^2 = \frac{\rho_s}{\rho} C_1^2 + \frac{\rho_n}{\rho} C_2^2 \quad (2.4)$$

Fourth sound has been observed by Rudnick and Shapiro in 1962 [2.8] . It has been used to study persistent superfluid currents of helium II [2.9] and as a crucial demonstration of the superfluidity of liquid helium-3. These sound velocities in helium II as a function of temperature are illustrated in Fig. 2.2 .

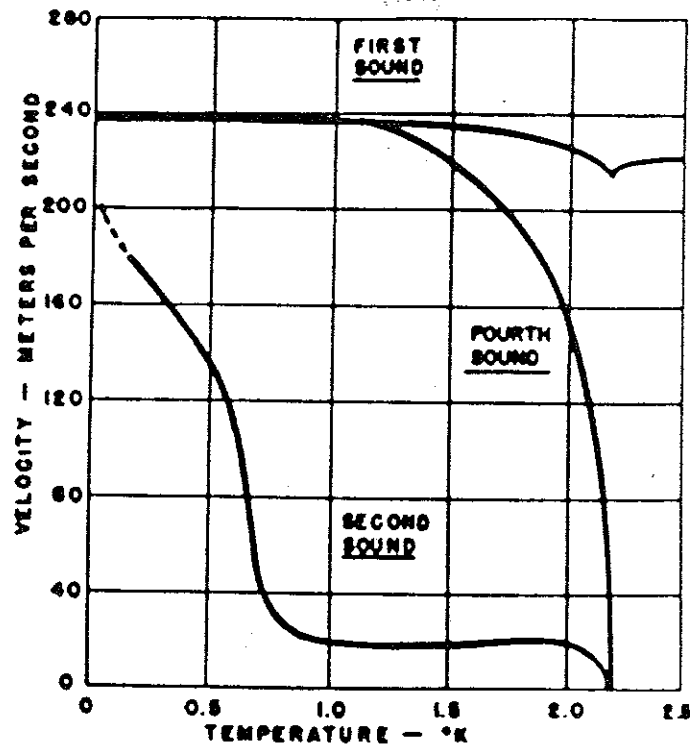


Fig. 2.2 The sound velocities in the helium II versus temperature.

Surface waves on liquid helium II film, is called third sound. The study of this wave is the basis of this thesis.

2.3 Third Sound Theory and Experiment

Surface waves on bulk liquid helium were first discussed by Atkins [2.10], in order to explain the variation of surface tension with temperature. A few years later, he published an article which discussed the possible existence of an undetected type of wave propagation in liquid helium II [2.11]. In 1964, "third sound", a surface wave on thin films of superfluid helium, had been demonstrated experimentally. Now third sound is used as a powerful technique to measure other properties of superfluid helium. For instance, the measurement of Van der Waals force between helium atoms on different substrates, the study of spin polarized hydrogen, and the nonlinearity of helium films.

Third sound is a surface wave on a helium film, in which the superfluid component oscillates while the normal component remains locked to the wall. The free surface of the third sound relieves the compression that characterizes fourth sound. Fig 2.3 shows a fixed substrate with a third sound wave. The forces on the film include gravity, surface tension and Van der Waals force. The latter dominates both gravity and surface tension forces when the films are thin and the wavelengths are long and is the only restoring force considered in this treatment. This attractive force is due to the induced dipole moments between the substrate and the film atoms.

The attractive part of the energy well in which a helium atom sits above a flat substrate is: [2.12]

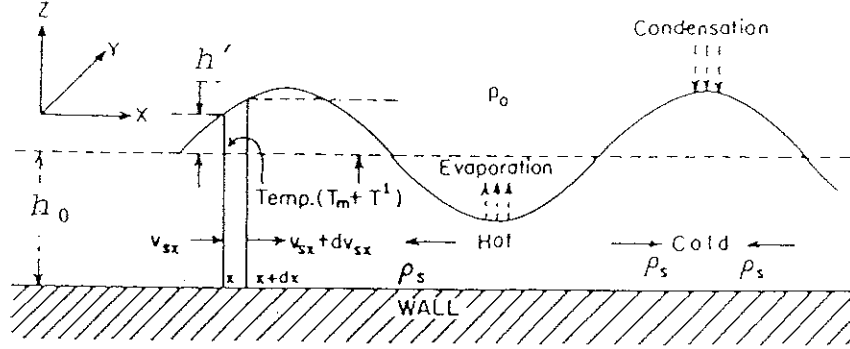


Fig. 2.3 Third sound wave propagate in the liquid helium film.

$$V = - \frac{\alpha}{d^3} \quad (2.5)$$

where α is the van der Waals constant, d is the distance between atom and substrate. Therefore, the restoring force will be :

$$f = - \left(\frac{\partial V}{\partial d} \right) = - \frac{3\alpha}{d^4} \quad (2.6)$$

This restoring force, however, will allow an oscillation in the thickness of the film with variations in pressure and temperature. Third sound is therefore somewhat similar to classical shallow -water waves, but the superfluidity of liquid helium is essential to its existence since such a wave would be rapidly attenuated in a thin film of an ordinary viscous liquid.

The next section, the two-fluid equations are presented which predict a

traveling surface wave, the third sound wave.

As we have already discussed before, we can treat a superfluid helium as composite of two inseparable fluids, a superfluid part and a normal part. The densities of the two component fluids sum to the total density of the helium fluid.

$$\rho = \rho_s + \rho_n \quad (2.7)$$

Each of these fluid components possess a velocity field: \vec{V}_s, \vec{V}_n . [2.13] The total mass current for the fluid is :

$$\vec{J} = \rho_s \vec{V}_s + \rho_n \vec{V}_n \quad (2.8)$$

and so mass conservation is expressed as

$$\frac{\partial \rho}{\partial t} = - \nabla \cdot \vec{J} \quad (2.9)$$

Since entropy is only carried out by normal fluid, we can write entropy conservation equation like:

$$\frac{\partial (\rho S)}{\partial t} = - \vec{\nabla} \cdot (\rho S \vec{V}_n) \quad (2.10)$$

where S is the total entropy per unit mass.

The Navier - Stokes equation for the total fluid is [2.14]

$$\rho_s \left[\frac{\partial \vec{V}_s}{\partial t} + (\vec{V}_s \cdot \vec{\nabla}) \vec{V}_s \right] + \rho_n \left[\frac{\partial \vec{V}_n}{\partial t} + (\vec{V}_n \cdot \vec{\nabla}) \vec{V}_n \right] = -\vec{\nabla} P + \eta \nabla^2 \vec{V}_n \quad (2.11)$$

where P is the pressure in the fluid and η is the viscosity of the normal fluid.

The Navier - Stokes equation for the superfluid should not have a viscosity term since the superfluid flows without viscosity. The superfluid component has been found to respond to both temperature and pressure gradients. This suggests that chemical potential of the fluid drives the fluid. These considerations result in an Euler equation for the superfluid [2.14]

$$\frac{\partial}{\partial t} \vec{V}_s + (\vec{V}_s \cdot \vec{\nabla}) \vec{V}_s = -\nabla \mu = -\frac{1}{\rho} \nabla P + S \nabla T \quad (2.12)$$

Equation (2.11) and (2.12) imply the Navier - Stokes equation for the normal fluid to be

$$\rho_n \left[\frac{\partial \vec{V}_n}{\partial t} + (\vec{V}_n \cdot \vec{\nabla}) \vec{V}_n \right] = -\frac{\rho_n}{\rho} \vec{\nabla} P + \rho_s S \vec{\nabla} T + \eta \nabla^2 \vec{V}_n \quad (2.13)$$

These are simplified equations for the two - fluid model. More general equations are discussed in Landau and Lifshitz [2.15] and in Khalatnikov [2.16] . The velocity of a third sound wave can be calculated from the two - fluid equations outlined above.

As we discussed previously, the velocity of the superfluid component \vec{V}_s is parallel to the substrate that we assume here is X-direction, which is also the direction of propagation of the third sound (Fig. 2.3). Assume also

that the motion of the superfluid is irrotational everywhere [2.17], so that V_{sx} does not vary in the Z direction perpendicular to the wall and the surface. The width of the film in Y - direction is W , the height of the surface above its equilibrium position is $h'(x)$ and the temperature of the liquid is $T=T_0 +T'(x)$, where T_0 is the mean temperature and $T'(x)$ is the temperature oscillation when third sound is propagating.

The equation for conservation of mass is derived from the following : consider a slab of the film between x and $x + \delta x$. The rate of flow of mass of superfluid across the interfaces at x and $x + \delta x$ is

$$\frac{dm}{dt} = - \langle \rho_s \rangle W d \left(\frac{\partial V_{sx}}{\partial x} \right) \delta x \quad (2.14)$$

We do not include that the slab loses mass by evaporation at its surface. In fact, the amount of evaporation at lower temperature , say below 0.2 K , is negligible, but at temperature around 0.5K begins to be noticeable. [2.18]

The net change in mass of liquid in the slab due to flow does not change the density but does change the height of the surface h

$$\frac{dm}{dt} = \rho \frac{\partial h}{\partial t} W \delta x \quad (2.15)$$

combining equations (2.14) and (2.15), the equation expressing conservation of mass is finally found to be

$$\rho \frac{\partial h}{\partial t} + \langle \rho_s \rangle h \frac{\partial v_{sx}}{\partial x} = 0 \quad (2.16)$$

The equation of conservation of entropy must contain the assumption made by the two - fluid model that the normal fluid component carries

entropy and superfluid component does not. In our case, normal fluid is locked on the substrate, so , if you look at the surface of the film from the top, it is easy to conclude that the entropy per unit area is not dependent on time, because there is no lateral entropy flow. This means

$$\frac{d}{dt} (\rho S h) = 0 \quad (2.17)$$

S is entropy per unit mass, h is thickness of the film. Therefore, assuming the fluid as a whole is incompressible,

$$S \frac{dh}{dt} + h \frac{dS}{dt} = 0 \quad (2.18)$$

Introducing a thermodynamic relationship

$$dS = \frac{C}{T} dT$$

$$\frac{dS}{dt} = \frac{C}{T} \frac{dT}{dt} \quad (2.19)$$

where C is heat capacity per unit mass, inserting this into (2.18), results in

$$\frac{S}{h} \frac{dh}{dt} + \frac{C}{T} \frac{dT}{dt} = 0 \quad (2.20)$$

The equation which approximately describes the dynamics of the superfluid film is known as Euler's equation. It is the linearized version of (2.12) which relates the horizontal acceleration of the surface wave to the pressure and temperature gradients which cause this acceleration.

$$\frac{\partial V_s}{\partial t} = - \frac{1}{\rho} \nabla P + S \nabla T \quad (2.21)$$

The pressure change here is just the hydrostatic change in the van der Waals field,

$$\delta P = \rho f \delta h \quad (2.22)$$

If we consider only the x - component of equation (2.21) and using (2.22), we get

$$\frac{\partial V_{sx}}{\partial t} = - f \frac{\partial h}{\partial x} + S \frac{\partial T}{\partial x} \quad (2.23)$$

Equations (2.16) , (2.20) and (2.23) are three equations for the three unknowns h , T and V_s . One can solve the equations by assuming some travelling wave solutions.

If one considers a plane wave moving through the film and that the film parameters have only small oscillations, then we can write solutions like :

$$\begin{aligned} h &= h_0 + h' e^{i(kx - \omega t)} & h' &\ll h_0 \\ V_s &= V_0 + V' e^{i(kx - \omega t)} & V' &\ll V_0 \\ T &= T_0 + T' e^{i(kx - \omega t)} & T' &\ll T_0 \end{aligned} \quad (2.24)$$

Substituting (2.24) into equations (2.16), (2.20) and (2.23) , we get three homogeneous linear equations. They have non-zero solutions only if the determinant of the coefficient matrix is set equal to zero. That is :

$$\omega^2 = \frac{\langle \rho_s \rangle}{\rho} \left[f h_0 + \frac{T S^2}{C} \right] \quad (2.25)$$

Therefore, C_3 , the third sound velocity, is defined as

$$C_3 \equiv \frac{\omega}{k} = \sqrt{\frac{\langle \rho_s \rangle}{\rho} \left[f h_0 + \frac{T S^2}{C} \right]} \quad (2.26)$$

where the inside of the square root, the first term corresponds to the substrate restoring force, and the second term represents the thermomechanical restoring force. Usually, the second term is much smaller than first term. For instance, at a warm temperature of 0.5 kelvin and an 8 layer film, the thermomechanical force is still only about 100 times smaller than the restoring force. Therefore, in this thesis, I disregarded all thermodynamic terms.

2.4 Discussion.

From equation (2.20) we can easily get

$$\frac{h'}{h_0} = -\frac{C}{S} \frac{T'}{T} \quad (2.27)$$

This equation clearly shows that the surface wave is accompanied by a temperature wave which is out of phase with it. This means the fluid in a third sound wave is cold at the crest of the wave and warm in the trough. In the other words, the higher temperature corresponds to the smaller film thickness. This also shines some light on the attenuation mechanism. If

there is any heat conduction between the film and substrate, the surface wave will decay. Film evaporation and lateral heat conduction are the other attenuation mechanisms. In all cases the surface wave's energy is reduced. The very low experimental temperatures made both film evaporation and lateral heat conduction are very small. Therefore, these processes were neglected in the calculations.

Another important point is that all second and higher order terms have been omitted during the calculation. The details of this calculation, which include dissipation terms can be found in Bergman (1971) [2.19] .

2.5 Solution for 2 - D Circular Third Sound Resonator

The calculations in section 2.3 are based on the one dimensional case, so the solutions of equation of motion are plane waves. In fact, the third sound resonators that were used in our laboratory are disk shaped circular resonators. The solution for this case is not a simple plane wave, but more complicated, it is a combination of Bessel functions and trigonometrical functions. In our resonator, the film is adsorbed onto the inner surface formed by two circular disks joined at their perimeter. The normal modes of the thickness oscillations of the third sound wave are given by,

$$h(r, \phi) = h_0 + h_{nm} J_m(k_{nm} r) e^{im \phi} \quad (2.28)$$

where r and ϕ are polar coordinates, a is the radius of the resonator, and k_{nm} and m determine the modes configuration. For our resonator

$$k_{nm} = \frac{X_{nm}}{a} \quad (2.29)$$

Here x_{nm} is a zero of the derivative of a Bessel function, $J'_m(x)$. The static film thickness is h_0 . There are two modes associated with $+m$ and $-m$. These modes are degenerate and have the same resonant frequency.

Appendix C describes the simple coupling of these modes to capacitive transducers. Chapter 4 describes the coupling to a more complicated drive capacitor.

Chapter 3 The Frequency Splitting

This chapter deals with the basic idea of frequency splitting. It turns out that the frequency splitting is determined not only by the Doppler shift which is caused by the film flow but also the geometric configurations of distortions in the shape of the resonator. Both of these effects are shown to determine the normal modes.

3.1 Circulation Splitting of a Third Sound Resonator

In a geometrically perfect resonator with no circulation, there will be no frequency shift, since the eigenstates of the mode are degenerate. But if either of these conditions - perfect geometry and no circulation - is not be satisfied, frequency splitting can not be avoided. The circulation of helium film in a two dimension system was discovered long ago. Doppler shifted third sound pulses have served for years as a probe of the flow state in these films. Here, a thermal drive transducer is flanked by pick-up bolometers upstream and downstream from a drive heater and the difference in arrival times of a third sound pulse determines the film flow speed. The development of third sound resonator [3.1, 3.2] greatly improved the potential precision of these measurements because of the intrinsically superior accuracy of resonance techniques over time-of-flight measurements. Unfortunately, the closed and restricted geometry of resonators does not lend itself easily to persistent current applications. Earlier experiments incorporating third sound resonators of various geometries on rotating cryostats have failed to show the expected splitting of resonant modes even when the presence of a film flow was evident by other means [3.3 ,3.4] . Persistent current splitting of other superfluid sound modes have been

observed [3.5] but not in two-dimensional films.

Our work with the third sound resonator described in chapter three has shown clearly this splitting in the two dimensional case. The frequency associated with the third sound velocity which we try to detect was

$$\omega = C_3 k \quad (3.1)$$

where k is a wave vector which is dependent on the mode configuration and the radius of the cell.

$$ka = X_{nm} \quad (3.2)$$

Here a is the radius of the cell as before, and X_{nm} in this case is the zero of the derivative of $J_m(x)$, so we can rewrite the frequency

$$\omega_0 = \frac{C_3 X_{nm}}{a} \quad (3.3)$$

The modes with m having opposite signs are degenerate in the ideal case. The degeneracy may be lifted because of the Doppler shift if there is a background film flow. The resulting resonant frequency shifts for arbitrary resonator geometries and flow field are difficult to calculate but for small flow speed perturbation technique can be used. For the circular resonator with the curl free, symmetric flow field

$$v(r) = v_0(r) = \frac{a}{r} v_0(a) \quad (3.4)$$

the shift for small v_0 can be written as

$$\frac{\Delta\omega}{\omega_0} = \gamma_{nm} \frac{v_0(a)}{C_3} \quad (3.5)$$

where γ_{nm} is a constant which represent the weighing of the Doppler shift within each mode and includes a factor of ρ_s/ρ , the superfluid fraction. In order to get this constant γ_{nm} , we have to work on the equations of motion again and use perturbation technique. First, recall Euler's equation for flow field with velocity \vec{v} , which is

$$\frac{\partial \vec{v}_s}{\partial t} + (\vec{v}_s \cdot \nabla) \vec{v}_s = -f \nabla h \quad (3.6)$$

here we must keep the convective derivative term $(\vec{v}_s \cdot \nabla) \vec{v}_s$ because of the steady state flow.

Another equation we can get from the condition for the incompressible fluid, is:

$$\nabla \cdot \vec{v}_s = 0 \quad (3.7)$$

One can express this equation in a two dimensional form,

$$\nabla_{xy} \cdot \vec{v}_s(x, y) + \frac{\partial v_{sz}}{\partial z} = 0 \quad (3.8)$$

Now, integrating both sides of equation (3.8) along z-direction,

$$\int_0^h \nabla_{xy} \cdot \vec{v}_s(x, y) dz + \int_0^h \frac{\partial v_{sz}}{\partial z} dz = 0 \quad (3.9)$$

and assuming the lateral velocity is not dependent on z-direction, we can

treat the function inside the first integral as a constant. Therefore, (3.9) yields,

$$h(\vec{\nabla}_{xy} \cdot \vec{v}_s) + v_z|_0^h = 0 \quad (3.10)$$

The velocity in z-direction at the substrate should be zero because the fluid can not go anywhere, but at the surface of the film the velocity should be the same as the height oscillation of the film, this implies,

$$\frac{\partial h}{\partial t} = - h(\vec{\nabla} \cdot \vec{v}_s) \quad (3.11)$$

(3.6) and (3.11) are the equations we are going to use to get the constant γ_{nm} . Now, if we assume the solutions are,

$$h = h_0 + h' \quad (3.12)$$

$$\vec{v}_s = \vec{v}_0(r) + \vec{v}' \quad (3.13)$$

with :

$$\vec{v}_0(r) = \frac{n h}{m_4 r} \hat{\phi} \quad (3.14)$$

obviously, $\vec{v}_0(r)$ is the stationary flow field which is only dependent on the radius r . Its direction is along $\hat{\phi}$, the polar direction. The oscillations h' and \vec{v}' are assumed to be small.

Substituting (3.12) and (3.13) into (3.6) and (3.10), and dropping all second order terms, one finds out,

$$\frac{\partial \vec{v}'}{\partial t} = - f \nabla h' - \vec{\nabla}(\vec{v}_0 \cdot \vec{v}') \quad (3.15)$$

$$\frac{\partial h'}{\partial t} = -h_0(\vec{\nabla} \cdot \vec{v}') - h' \vec{\nabla} \cdot \vec{v}_0 - \vec{v}_0 \cdot \nabla h' \quad (3.16)$$

Since h' and \vec{v}' are time dependent variables, we suppose they have the form $U e^{-i\omega t}$ where U represents both h' and \vec{v}' as a 3 - D vector. Perturbation theory tells us that we can suppose both of them like this :

$$U = (U_\alpha + \delta U) e^{-i(\omega_\alpha + \Delta\omega)} \quad (3.17)$$

where U is the solution for (3.15) and (3.16) with $v_0 = 0$. Putting this back to the equations (3.15) and (3.16), one finds (private communication with Dr. Ralph Baierlein, see appendix D for details) :

$$\frac{\Delta\omega}{\omega_0} = \frac{v_0(a)}{C_3} \frac{2mX_{nm}}{(X_{nm}^2 - m^2)J_m^2(X_{nm})} \left[\int_0^{X_{nm}} \frac{J_m^2(x)}{x} dx - \frac{1}{8}\delta_{m1} \right] \quad (3.18)$$

So the weighing of the Doppler shift within each mode can be written,

$$\gamma_{nm} = \frac{2mX_{nm}}{(X_{nm}^2 - m^2)J_m^2(X_{nm})} \left[\int_0^{X_{nm}} \frac{J_m^2(x)}{x} dx - \frac{1}{8}\delta_{m1} \right] \quad (3.19)$$

then we can have :

$$\frac{\Delta\omega}{\omega} = \gamma_{nm} \frac{v(a)}{C_3} \quad (3.20)$$

Table (3 -1) gives some results of γ_{nm} for several different modes calculated from this expression. It clearly shows that γ_{nm} approaches 1 as m increases. This can be understood in the following manner: since γ_{nm} can be thought as the overlap of the flow field with the modes, when m increases, the modes in the middle section will move toward to the perimeter of resonator. Therefore, $v(r)$ approaches to $v(a)$. This overlapping becomes maximum at the perimeter, so γ_{nm} approaches to 1 .

It is difficult to explain why the (1,1) mode does not follow this role. From the calculation, the (1 ,1) mode has an extra term, which came from the contribution of the flow singularity in the center of the cell. Therefore, it makes a smaller value than the other modes. This behavior of the (1,1) mode was also observed experimentally.

$\begin{array}{c} N \\ \backslash \\ M \end{array}$	1	2	3	4
1	0.709	1.421	1.470	1.494
2	1.170	1.336	1.401	1.438
3	1.129	1.286	1.354	1.395
4	1.106	1.251	1.319	1.362

Table 3 - 1. Some theoretical results of γ_{nm} for several different third sound modes.

3.2 Geometric Asymmetry Splitting.

Initially we did not appreciate the importance of the geometrical asymmetry splitting. But one day we accidentally made a cell where its center hole was not perfectly lined up. We decided to use it anyway. When we did use it, we got a very large splitting which we had never seen before. There was no evidence to show this was a circulation splitting. The total splitting was dominated by hole misalignment, and there was no way to see the circulation splitting because it was so small compared to this. We then decided to switch to an almost identical cell except this time the hole in the center was perfectly aligned. We have not seen such a splitting again even when we have tried different runs and have changed again to other cells. This told us that geometrical asymmetry plays a role in the mode splitting. We then had to reconsider our theoretic model to take this factor into account.

Assume that the geometrical asymmetry is due to a small deviation from a circular perimeter, i.e. , that the radius of the resonator edge is given by

$$r(\phi) = a[1 + \eta(\phi)] \quad (3.21)$$

together with two conditions: $\eta(\phi) \ll 1$, and the angular average of $\eta(\phi)$ equals to zero. Then first order perturbation of boundary conditions of the degenerate modes gives

$$\frac{\Delta\omega}{\omega_0} = \Delta = \pm |\Delta_m| \quad (3.22)$$

$$\Delta_m = \frac{1}{2\pi} \int_0^{2\pi} \eta(\phi) e^{-2i m \phi} d\phi \quad (3.23)$$

There are many other ways that a geometric asymmetry can be represented. Even driving a third sound resonator by a DC voltage can cause a mode to split due to the average attractive force acting on the film. In general, the asymmetries can always be represented in the above form. We then can take into account this effect to the total splitting and quantitatively determine how this will affect our experimental results.

3.3 Total Splitting.

I have already introduced the two parts of the splitting. Now let us think about both of them acting together.

There exist two types of waves inside of a circular resonator. One is a standing wave where the wave can have two modes propagating along either X-direction or Y-direction (see Fig. 3.1) . Both of them represent height oscillation in the Z-direction.

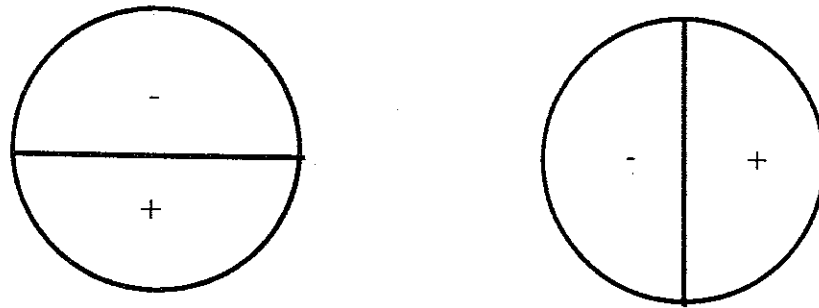


Fig. 3.1 Two possible modes of standing waves.

The other wave is called a travelling wave or rotating wave, which involves both height oscillation and lateral propagation along $\hat{\phi}$ - direction. This wave also can have two modes which are rotating either clockwise or counterclockwise (see Fig. 3.2).

So, basically we have two bases which can be chosen for the calculation of total splitting. For convenience, we decided to use the rotational basis. This analysis is the same as any simple two level system, since the coupling between modes other than the split $\pm m$ mode is negligible. Considering the frequency as the eigenvalues of a 2×2 matrix, the calculated shift given by (3.20) will be diagonal elements in the rotating basis, but geometrical asymmetry splitting must be diagonal in the standing wave basis since it is a consequence of the shape of the fixed resonator. This splitting will appear as off-diagonal elements in the rotating basis. Therefore, for a perfect resonator, i.e. no geometrical asymmetry, and no background film flow, the degenerate state can be associated with the matrix,

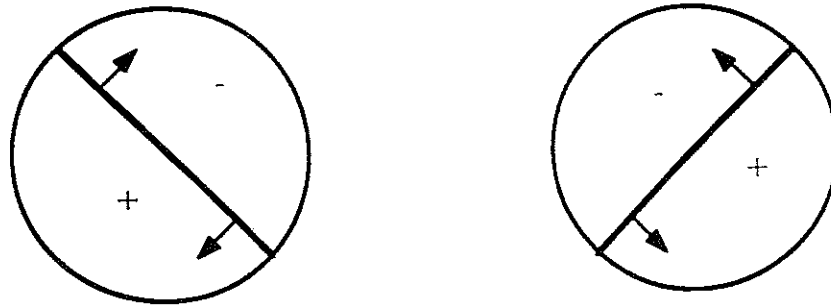


Fig. 3.2 Two possible modes of travelling waves.

$$\begin{bmatrix} \omega_0 & 0 \\ 0 & \omega_0 \end{bmatrix} \quad (3.24)$$

The eigenvalues of both eigenstates of course would be the normal resonant frequency ω_0 .

If we take into account for the splitting due to a circulation of fluid, we now have modes determined by the eigenstates of

$$\begin{bmatrix} \omega_0 & 0 \\ 0 & \omega_0 \end{bmatrix} + \omega_0 \begin{bmatrix} \gamma & 0 \\ 0 & -\gamma \end{bmatrix} \quad (3.25)$$

where:

$$\gamma = \frac{\Delta \omega}{\omega_0} \quad (3.26)$$

represents strength of circulation splitting (3.18). Finally, taking into account both the circulation splitting and geometrical asymmetry splitting, we have,

$$\omega_0 \begin{bmatrix} 1 + \gamma & \Delta_m \\ \Delta_m^* & 1 - \gamma \end{bmatrix} \quad (3.27)$$

constructed to give standing waves as eigenstates when $\gamma = 0$ according to (3.24). The eigenvalues and eigenfunctions of this matrix are the resonant frequencies and the two nondegenerate rotational states.

3.4 Discussion.

Having chosen for our basis, the left and right rotational states, the eigenfunction can be expressed as a linear combinations of these states. This will lead to

$$\psi_{\sigma m} = a_{\sigma,+m} e^{im\phi} + a_{\sigma,-m} e^{-im\phi} \quad (3.28)$$

where σ has only two values, which are $+1$ and -1 , representing the higher and lower frequency modes. Here $\pm m$ represent two different rotating states, which are also our basis.

To find the eigenvalues and eigenstates, we must have solve the equation

$$\begin{bmatrix} 1 + \gamma & \Delta e^{i\phi_0} \\ \Delta e^{-i\phi_0} & 1 - \gamma \end{bmatrix} \begin{bmatrix} a_{+m} \\ a_{-m} \end{bmatrix} = \lambda \begin{bmatrix} a_{+m} \\ a_{-m} \end{bmatrix} \quad (3.29)$$

where $\Delta e^{i\phi_0}$ represents the geometrical asymmetry (3.23). Here Δ is a real number and ϕ_0 is some phase shift, which is related to the cell asymmetry orientation only. It is easy to find the eigenvalues from equation (3.29),

$$\lambda_{\pm} = 1 \pm \sqrt{\gamma^2 + \Delta^2}. \quad (3.30)$$

Then we can find our eigenstates, that is,

$$\begin{bmatrix} a_{+m} \\ a_{-m} \end{bmatrix} = N \begin{bmatrix} \Delta e^{i\phi_0} \\ -\gamma \pm \sqrt{\gamma^2 + \Delta^2} \end{bmatrix} \quad (3.31)$$

Where N is the normalization factor. The wavefunction can be chosen to satisfy the normalization condition

$$\frac{1}{2\pi} \int_0^{2\pi} \psi_{\sigma m} \psi_{\sigma m}^* d\phi = 1 \quad (3.32)$$

Substituting (3.28) to (3.32) we have :

$$a_m^* a_m + a_{-m}^* a_{-m} = 1 \quad (3.33)$$

This leads to

$$N = \frac{1}{\sqrt{2(\gamma^2 + \Delta^2) \mp 2\gamma\sqrt{\gamma^2 + \Delta^2}}} \quad (3.34)$$

Therefore, (3.31) can be rewritten as

$$\begin{bmatrix} a_{\sigma m} \\ a_{\sigma -m} \end{bmatrix} = \frac{1}{\sqrt{2\delta^2 - 2\sigma\gamma\delta}} \begin{bmatrix} \Delta e^{i\frac{\phi_0}{2}} \\ (-\gamma + \sigma\delta) e^{-i\frac{\phi_0}{2}} \end{bmatrix} \quad (3.35)$$

where $\delta = \sqrt{\gamma^2 + \Delta^2}$ is defined as the total splitting. Note here that we break $e^{i\phi_0}$ into two parts in (3.35), which is fine since it does not change the normalization. The eigenvalues and hence the resonant frequencies are given by

$$\omega = \omega_0 \left[1 \pm \sqrt{\gamma^2 + \Delta^2} \right] = \omega_0 \left[1 \pm \sqrt{\left(\frac{\Delta \omega}{\omega_0} \right)^2 + \Delta^2} \right] \quad (3.36)$$

When we recall equation (3.5), we have

$$\omega = \omega_0 \left[1 \pm \sqrt{\left(\frac{\gamma_{nm} v_0 k}{\omega_0} \right)^2 + \Delta_m^2} \right] \quad (3.37)$$

Equation (3.37), however, represents a clear relationship between two kinds of splitting and resonant frequency. A plot of resonant frequencies versus the circulation speed v_0 can be found in Fig. 3.3. At low circulation speeds the splitting is determined by the geometrical asymmetry. The eigenmodes, similarly, are the standing waves. This can be checked from equation (3.37). When γ is small, the total splitting is about same as geometric splitting, and the two eigenstates tend to be about same but out of phase. This exactly represents the standing wave in the resonator. At high circulation speeds the splitting is as in (3.5) and the eigenmodes are the travelling waves. If we rewrite equation (3.37) like

$$\left(\frac{\omega - \omega_0}{\omega_0} \right)^2 = \left(\frac{\gamma_{nm} v_0 k}{\omega_0} \right)^2 + \Delta_m^2 \quad (3.38)$$

can be noted here that the geometrical splitting from (3.38) is a fixed ratio with respect to the two resonant frequencies whereas the Doppler shift is a fixed difference (see Fig. 3.3). Fig. 3.3 shows that geometric asymmetry splitting can prevent measurement of small circulations. To overcome this problem, a technique which use an applied DC voltage or heat to cancel out the geometric asymmetry splitting is being developed. This is because the

third sound wave is both a temperature and a height oscillation and perturbations to either may be made to cancel the degeneracy. Preliminary results were favorable, more information of this technique can be found in Reference [6.3].

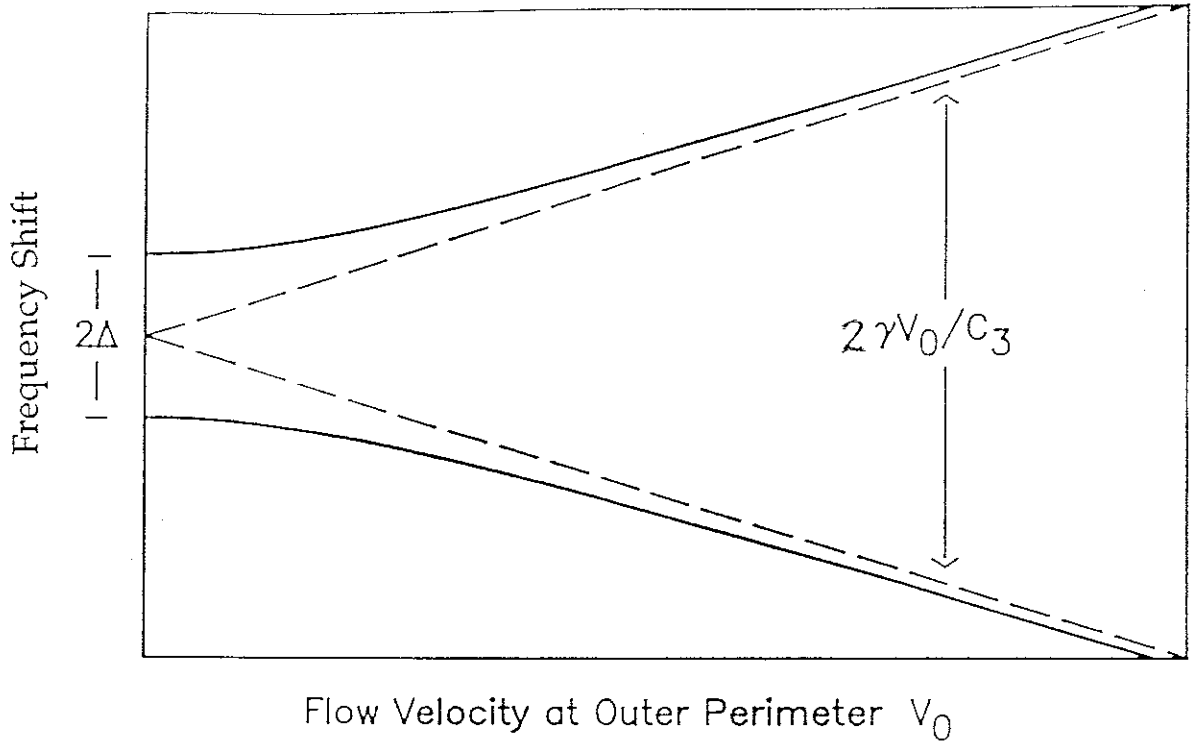


Fig. 3.3 The solid lines show the normalized resonant frequencies vs. the size of the circulation calculated from equation (3.38). The dashed lines represent only the Doppler shift. Small circulations would be obscured by the asymmetry shift Δ . For the $n=1, m=3$ mode, $\Delta = 9.4 \times 10^{-4}$. The frequency scale is offset to emphasize the splittings.

Chapter 4 Rotational Drive Third Sound Resonator

This chapter discusses details of the rotational drive third sound resonator and the principle of measuring small film flow velocities by this technique. The response of the rotational drive third sound resonator is also calculated and it show unique results.

4.1 Introduction

It was first thought by us that the technique of rotational drive third sound resonator could be used to detect persistent currents in the helium film. The disadvantages of the usual way to measure film flow velocities which we will discuss in chapter 6, are obvious. For example, you have to watch for the splitting changes in order to have full confidence that you actually see a film flow instead of other mechanisms which lead to splittings such as geometrical asymmetry splitting inside of the third sound resonator. This is particularly difficult when there is no way to control the circulation velocities.

The rotational drive , however, has lead to a great advantage in detecting small film flow in the third sound resonator. It is simple to rule out the geometrical asymmetry splittings since it shows no difference when the driving directions are switched. However, persistent current measurements will show a difference as different directions were driven. The actual rotational drive configuration is shown in Fig. 4.1.

Fig. 4.1 shows the picture of the top plate of the third sound resonator. The whole surface was deposited with gold except for crossed lines which isolated regions from each other by the shadows cast by 50 μm wire masks during the gold deposition. The four parts of the cell are drive plates 1 and 2 ,

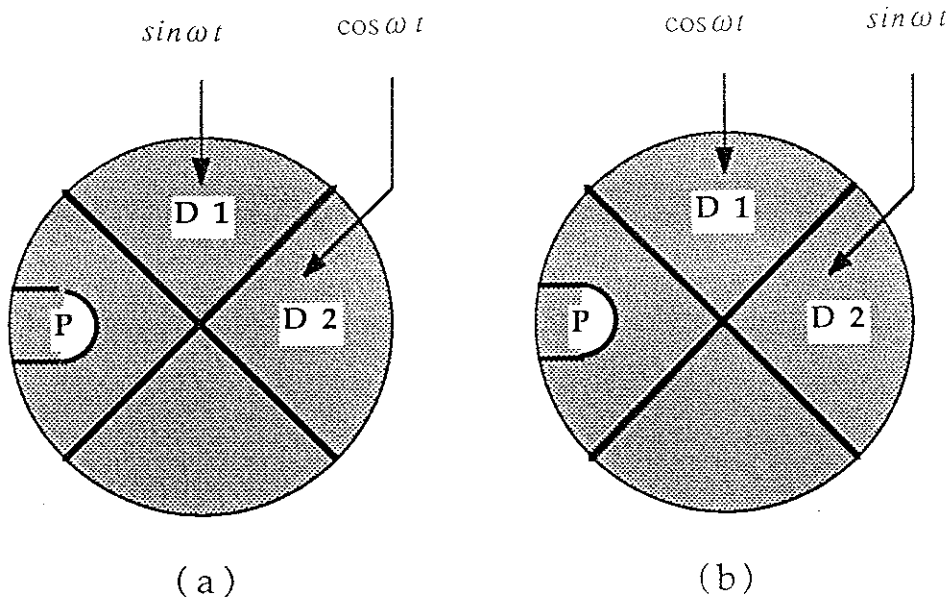


Fig. 4.1 The schematic drawing of the definition of the rotational drive. (a) Right hand drive (RHD); (b) Left hand drive (LHD). P is the pick - up area.

the pick-up area, and ground respectively. The right hand drive which we used in this thesis is defined in such a way that if drive voltage at drive 2 is $\cos \omega t$, drive 1 is 90 degree phase difference in respect to drive 2, hence $\sin \omega t$, as shown in Fig. 4.1 (a). The definition of left hand drive is opposite to (a) shown in Fig. 4.1(b). It is obvious that you can get a stronger signal if the drive direction is same as the direction of film flow. There are a total of four different setting situations as stated before. In principle, the rotational drive technique can distinguish all odd plus and minus modes. But due to the geometrical symmetry of the even modes, it would not be able to detect the differences for right hand drive and left hand drive conditions. This prediction was also proved by the experimental results.

4.2 Calculation of the General Responses of The Third Sound Resonator

In this section we will calculate the actual responses of the third sound resonator for an arbitrary drive configurations. To calculate the amplitude for a particular mode for any drive configurations, we can start from the equations of motion for the superfluid film [4.1]. Those are

$$\frac{\partial h}{\partial t} = -h_0 \frac{\rho_s}{\rho} \vec{\nabla} \cdot \vec{v} \quad (4.1)$$

$$\frac{\partial \vec{v}}{\partial t} = -f \nabla h + \vec{g} \quad (4.2)$$

where \vec{g} is the driving force which depends only on the transducer geometry. We already known from chapter 3 that the eigenvalues of the rotational states are :

$$\omega = \omega_0 \left[1 \pm \sqrt{\gamma^2 + \Delta^2} \right] \quad (4.3)$$

The correction due to the circulation of the film and geometrical asymmetry of the cell has been carried out by the perturbation method. From the chapter 3, the eigenfunctions can be written as

$$\vec{a}_\sigma = \frac{1}{\sqrt{2}} \begin{bmatrix} \sqrt{1 + \sigma \sin \theta} e^{i \frac{\phi_0}{2}} \\ \sigma \sqrt{1 - \sigma \sin \theta} e^{-i \frac{\phi_0}{2}} \end{bmatrix} \quad (4.4)$$

where we have defined

$$\sin \theta = \frac{\gamma}{\delta} \quad \text{and} \quad \delta^2 = \gamma^2 + \Delta^2 \quad (4.5)$$

and δ is the total splitting. The factor σ has only two values $+1$ and -1 which represents plus and minus modes. These eigenfunctions are the actual modes of the film inside the third sound cell. Since the calculations are complicated if all modes are involved, we will restrict our calculations to a two dimensional space, representing two of the usually degenerate modes for a particular unperturbed frequency, which are $+m$ and $-m$. By this way, we can define

$$h = h_0 + \eta = h_0 + \eta_{\sigma m} J_m(kr) \psi_{\sigma m} \quad (4.6)$$

where η also has an $e^{-i\omega t}$ time dependence which we have dropped it for simplicity. The wave function is

$$\psi_{\sigma m} = a_{\sigma, m} e^{im\phi} + a_{\sigma, -m} e^{-im\phi} \quad (4.7)$$

and

$$\vec{v} = \vec{v}' + \vec{v}_0 \quad (4.8)$$

where \vec{v}_0 has been set to zero now so that the proper eigenmodes have been determined, and η is the oscillation part of the film, $\eta_{\sigma m}$ are the amplitude of the state being considered in (4.5), which distinguish the different modes. Both η and \vec{v}' are small since they represent the oscillation of the film.

The time-derivative of equation (4.1) is

$$\frac{\partial^2 h}{\partial t^2} = -h_0 \frac{\rho_s}{\rho} \frac{\partial}{\partial t} (\vec{\nabla} \cdot \vec{v}) \quad (4.9)$$

The divergence of equation (4.2) is

$$\vec{\nabla} \cdot \frac{\partial \vec{v}}{\partial t} = -f \nabla^2 h + \vec{\nabla} \cdot \vec{g} \quad (4.10)$$

combining (4.9) and (4.10) yields

$$\begin{aligned} \frac{\partial^2 h}{\partial t^2} &= \frac{\rho_s}{\rho} h_0 f \nabla^2 h - \frac{\rho_s}{\rho} h_0 \vec{\nabla} \cdot \vec{g} \\ &= C_3^2 \nabla^2 h - \frac{\rho_s}{\rho} h_0 \vec{\nabla} \cdot \vec{g} \end{aligned} \quad (4.11)$$

In the next step, we are going to derive the driving force \vec{g} . Based on the cell geometry, the energy change per unit volume for a dielectric material moving into an electric field is

$$u = - \frac{\epsilon - \epsilon_0}{2\rho} E^2 \quad (4.12)$$

where E is electrical field which we apply to the resonator. Driving force per unit mass therefore is

$$\vec{g} = - \nabla u = \frac{\varepsilon - \varepsilon_0}{2\rho} \vec{\nabla} (E^2) \quad (4.13)$$

Since the electric field can be written as a voltage applied to capacitor plates, we can define it like

$$E^2 = \frac{V_d^2}{2d^2} G(r, \phi) \quad (4.14)$$

where V_d is the voltage across the capacitor and d is the gap between the capacitor plates. The factor "2" in the denominator comes from the square of the alternating drive voltage and DC terms have been dropped. The function $G(r, \phi)$ is a unitless function which describes spacial distribution of the electric field. The driving force per unit mass can be written as

$$\vec{g} = \frac{1}{4} \eta_0 f \vec{\nabla} G \quad (4.15)$$

with

$$\eta_0 = \frac{\varepsilon - \varepsilon_0}{\rho f} \frac{V_d^2}{d^2} \quad (4.16)$$

It should be noted that η_0 represents the static thickness change associated with a DC voltage of V_d .

Substituting (4.15) into (4.11) yields

$$\frac{\partial^2 \eta}{\partial t^2} = C_3^2 \nabla^2 \eta - \frac{1}{4} \eta_0 C_3^2 \nabla^2 G \quad (4.17)$$

where I have used

$$C_3^2 = \frac{\rho_s}{\rho} f h_0. \quad (4.18)$$

Along with equation (4.6) , we have

$$\frac{\partial^2 \eta}{\partial t^2} = -\omega^2 \eta \quad (4.19)$$

and

$$\nabla^2 \eta = -k_{nm}^2 \eta \quad (4.20)$$

substituting (4.19) and (4.20) into (4.17) yields,

$$-\omega^2 \eta = -k_{nm}^2 C_3^2 \eta - \frac{1}{4} \eta_0 C_3^2 \nabla^2 G \quad (4.21)$$

The spacial function G can be written as a Fourier - Bessel series

$$G = \sum_{n,m} G_m J_m(kr) e^{im\phi} \quad (4.22)$$

where k should be always k_{nm} inside of Bessel function and so on. As we said before, we only consider $\pm m$ states in this calculation, so G can be represented by

$$G = J_m(kr) \left(G_m e^{im\phi} + G_{-m} e^{-im\phi} \right) \quad (4.23)$$

with

$$G_m = \frac{\int_{\text{Drive}} G(r, \phi) J_m(kr) e^{-im\phi} dA}{\int_{\text{Cell}} J_m^2(kr) dA} \quad (4.24)$$

We can now write

$$\nabla^2 G = -k_{nm}^2 J_m(kr) \left(G_m e^{im\phi} + G_{-m} e^{-im\phi} \right) \quad (4.25)$$

Substituting (4.25) into (4.21) leads to

$$\left(\omega_{nm}^2 - \omega^2 \right) \eta_{\sigma m} \psi_{\sigma m} = \frac{1}{4} \omega_{nm}^2 \eta_0 \left(G_m e^{im\phi} + G_{-m} e^{-im\phi} \right) \quad (4.26)$$

where we canceled $J_m(kr)$ in both sides of the equation (4.26) and used the fact of $\omega_{nm}^2 = C_3^2 k_{nm}^2$.

Multiplying both sides of the equation (4.26) by $\psi_{\sigma m}^*$ and then integrating over ϕ with the normalization condition

$$\frac{1}{2\pi} \int_0^{2\pi} \psi_{\sigma m} \psi_{\sigma m}^* d\phi = 1 \quad (4.27)$$

leads to

$$\left(\omega_{nm}^2 - \omega^2 \right) \eta_{\sigma m} = \frac{1}{4} \omega_{nm}^2 \eta_0 \frac{1}{2\pi} \int_0^{2\pi} \psi_{\sigma m}^* \left(G_m e^{im\phi} + G_{-m} e^{-im\phi} \right) d\phi \quad (4.28)$$

After dividing by ω_{nm}^2 in both sides of the equation (4.27) , and using the definition of normalization of $\psi_{\sigma m}$, the result is

$$\eta_{\sigma_m} = \frac{\eta_0}{1 - \frac{\omega^2}{\omega_{nm}^2}} \frac{1}{4} \left(a_m^* G_m + a_{-m}^* G_{-m} \right) \quad (4.29)$$

If we define

$$\left(\vec{a}_\sigma^* \cdot \vec{D} \right) = \frac{1}{4} \left(a_m^* G_m + a_{-m}^* G_{-m} \right) \quad (4.30)$$

From (4.24) we obviously have, for components of \vec{D}

$$D_\pm = \frac{1}{4} \frac{\int_{\text{Drive}} G(r, \phi) J_m(kr) e^{\mp i m \phi} dA}{\int_{\text{Cell}} J_m^2(kr) dA} \quad (4.31)$$

Therefore

$$\eta_{\sigma_m} = \frac{\eta_0}{1 - \frac{\omega^2}{\omega_{nm}^2}} \left(\vec{a}_\sigma^* \cdot \vec{D} \right) \quad (4.32)$$

Substituting (4.32) into (4.6) gives the general response of the film inside third sound cell for any mode chosen. For each particular mode it also accounts for the shifted up and down modes of the lifted degeneracy into modes denoted by σ .

Equation (4.32) looks exactly like the equation for the amplitude of motion of a mass on the spring except that there is no dissipation term in the denominator, so we can add the dissipation term to each individual mode by analogy with mass on the spring. The frequency dependence of a third sound resonance mode is same as the mass on the spring. Therefore,

$$\eta_{\sigma} = \frac{\eta_0}{1 - \frac{\omega^2}{\omega_{\sigma}^2} - \frac{i\omega}{Q\omega_{\sigma}}} \left(\vec{a}_{\sigma}^* \cdot \vec{D} \right) \quad (4.33)$$

Here I have changed ω_{nm} to ω_{σ} properly account for the perturbation discussed in chapter 3 which is not included in equations of motion here.

If we go back to the very beginning to look at the equation (4.6), we can write the height oscillation of the helium film as

$$\eta(r, \phi) = \eta_{\sigma} J_m(kr) \psi_{\sigma m} \quad (4.34)$$

So the total capacitance change of a capacitive pickup can be written as

$$C = \frac{2\epsilon_0 \left(1 - \frac{\epsilon_0}{\epsilon} \right)}{d^2} \int_{Pickup} \eta(r, \phi) dA \quad (4.35)$$

Substituting (4.7) and (4.34) into (4.35) yields

$$C_{\sigma} = \frac{2\epsilon_0 \left(1 - \frac{\epsilon_0}{\epsilon} \right)}{d^2} \int_{Pickup} \eta_{\sigma} J_m(kr) \left(a_m e^{im\phi} + a_{-m} e^{-im\phi} \right) dA. \quad (4.36)$$

where C_{σ} is the capacitance change due to only a particular mode σ . This capacitance change gets converted to a frequency change f_{σ} in our detecting system. This is

$$\frac{f_{\sigma}}{f_0} = -\frac{1}{2} \frac{C_{\sigma}}{C_{\text{Total}}} \quad (4.37)$$

where f_0 is the frequency of the LC oscillator used to sense the capacitor change.

Again we are concerned with only two states which are $\pm m$. Combining (4.36) and (4.37) we have

$$f_{\sigma} = \eta_{\sigma m} \frac{\partial f}{\partial h} (\vec{a}_{\sigma} \cdot \vec{P}) \quad (4.38)$$

Where the "pickup" overlap \vec{P} can be defined as

$$\vec{P} = \frac{1}{\int_P dA} \left[\int_P J_m(kr) e^{im\phi} dA \right] \quad (4.39)$$

also if we define

$$\frac{\partial f}{\partial h} = -\frac{f_0}{d} \left(1 - \frac{\epsilon_0}{\epsilon} \right), \quad (4.40)$$

as the DC sensitivity of the LC detector to uniform film thickness changes. Finally, according equation (4.33), (4.38) can be rewritten as

$$f_{\sigma} = \frac{\eta_0 (\vec{a}_{\sigma}^* \cdot \vec{D}) (\vec{a}_{\sigma} \cdot \vec{P})}{1 - \frac{\omega^2}{\omega_{\sigma}^2} - \frac{i\omega}{Q\omega_{\sigma}}} \frac{\partial f}{\partial h} \quad (4.41)$$

Equation (4.41) is the general result for an arbitrary drive and pick-up

configurations. Again η_0 is the response to the DC voltage applied to the cell. The term $(\vec{a}_\sigma^* \cdot \vec{D})$ is the mode overlapping to the drive, and $(\vec{a}_\sigma \cdot \vec{P})$ is the overlapping to the pick - up. For a particular cell we now can calculate these integrals. In the next section, we will apply this result to our cell and actually calculate the drive response.

4.3. Calculations for the Rotational drive TSR.

As we discussed before, the rotational drive is made up of two separate drive regions as shown in Fig. 4.1 . In this section, we will calculate the responses of the driving signal for both right hand drive and left hand drive acting on either the $\sigma = 1$ or $\sigma = -1$ modes. This would be an application of equation (4.41). There are actually four different cases, where σ represents plus and minus modes and vector \vec{D} contains two different drive situations. We can rewrite equation (4.41) as

$$f_\sigma = F(\vec{a}_\sigma \cdot \vec{P})(\vec{a}_\sigma^* \cdot \vec{D}) \quad (4.42)$$

with

$$F = \frac{\eta_0}{1 - \frac{\omega^2}{\omega_\sigma^2} - \frac{i\omega}{Q\omega_\sigma}} \frac{\partial f}{\partial h} \quad (4.43)$$

In the next step, we will apply the rotational drive to our third sound cell, and look at what are the results from equation (4.42).

The definition of \vec{a}_σ is

$$\vec{a}_\sigma = \frac{1}{\sqrt{2}} \begin{bmatrix} \sqrt{1 + \sigma \sin \theta} e^{i \frac{\phi_0}{2}} \\ \sigma \sqrt{1 - \sigma \sin \theta} e^{-i \frac{\phi_0}{2}} \end{bmatrix} \quad (4.44)$$

and the vector \vec{D} from equation (4.31) is

$$\vec{D} = \frac{1}{4} \frac{1}{\int_{\text{cell}} J^2 dA} \begin{bmatrix} \int_{\text{Drive}} G(r, \phi) J e^{-im \phi} dA \\ \int_{\text{Drive}} G(r, \phi) J e^{+im \phi} dA \end{bmatrix} \quad (4.45)$$

Referring to the definition of rotational drive in Fig. 4.1 and we can define $G(r, \phi)$ now. For the right hand drive, it is

$$G(r, \phi) = \begin{cases} 1 & -\frac{\pi}{4} < \phi < \frac{\pi}{4} & 0 < r < a \\ i & \frac{\pi}{4} < \phi < \frac{\pi}{4} & 0 < r < a \\ 0 & & \text{Elsewhere} \end{cases} \quad (4.46)$$

and for the left hand drive, it defines like

$$G(r, \phi) = \begin{cases} i & -\frac{\pi}{4} < \phi < \frac{\pi}{4} & 0 < r < a \\ 1 & \frac{\pi}{4} < \phi < \frac{\pi}{4} & 0 < r < a \\ 0 & & \text{Elsewhere} \end{cases} \quad (4.47)$$

The factors of i result in $\sin \omega t$ time dependence when the assumed $e^{-i\omega t}$

factor is considered. Both of these can be combined to

$$G_q(r, \phi) = \begin{cases} e^{i\frac{\pi}{4}(1-q)} & -\frac{\pi}{4} < \phi < \frac{\pi}{4} & 0 < r < a \\ e^{i\frac{\pi}{4}(1+q)} & \frac{\pi}{4} < \phi < \frac{3\pi}{4} & 0 < r < a \\ 0 & \text{Elsewhere} & \end{cases} \quad (4.48)$$

where $q = 1$ denotes right hand drive, and $q = -1$ denotes left hand drive. The components of \vec{D}_{\pm} are then

$$D_{q,\pm} = \frac{1}{4} \frac{\int_{\text{Drive}} G_q(r, \phi) J_m(kr) e^{\mp im \phi} dA}{\int_{\text{Cell}} J_m^2(kr) dA} \quad (4.49)$$

Substituting equation (4.48) into the definition of D_{\pm} for both right and left drives, we have

$$D_{q,\pm} = \frac{1}{4} \frac{1}{\int_{\text{Cell}} J_m^2 dA} \int_0^a r J_m(kr) dr \left[e^{i\frac{\pi}{4}(1-q)} \int_{-\pi/4}^{\pi/4} e^{\mp im \phi} d\phi + e^{i\frac{\pi}{4}(1+q)} \int_{\pi/4}^{3\pi/4} e^{\mp im \phi} d\phi \right] \quad (4.50)$$

If we define (same for either + and -)

$$D_0 = \frac{1}{4} \frac{1}{\int_{\text{Cell}} J_m^2 dA} \int_0^a r J_m(kr) dr \int_{-\pi/4}^{\pi/4} e^{\mp im \phi} d\phi \quad (4.51)$$

We can change variables in the last integral of (4.50), and we can rewrite it

in terms of D_0 , this leads to

$$D_{q,\pm} = D_0 \begin{bmatrix} e^{i\frac{\pi}{4}(1-q)} & \mp e^{i\frac{m}{2}\pi} e^{i\frac{\pi}{4}(1+q)} \\ 0 & 0 \end{bmatrix} \quad (4.52)$$

which can be written as

$$\vec{D}_q = D_0 e^{i\frac{\pi}{4}(1-q)} \begin{bmatrix} 1 + i^{(q-m)} \\ 1 + i^{(q+m)} \end{bmatrix} \quad (4.53)$$

Next, we have to work on \vec{P} , which doesn't depend on the rotation sense q .
According to the definition of \vec{P} ,

$$\vec{P} = \frac{1}{\int_{\text{Pickup}} dA} \begin{bmatrix} \int_{\text{Pickup}} J_m(kr) e^{im\phi} dA \\ \int_{\text{Pickup}} J_m(kr) e^{-im\phi} dA \end{bmatrix} \quad (4.54)$$

or defining

$$P_0 = \frac{\int_{\text{Pickup}} J e^{\pm im\phi} d\phi}{\int_{\text{Pickup}} dA} \quad (4.55)$$

we get

$$\vec{P} = P_0 \begin{bmatrix} 1 \\ 1 \end{bmatrix} \quad (4.56)$$

Obviously, (4.54) has nothing to do with the rotational drive. We can substitute equations (4.44), (4.53) and (4.54) into (4.41). This gives, after some complex manipulation,

$$f_{\sigma q} = FD_0 P_0 e^{i\frac{\pi}{4}(1-q)} \left[1 + iq \cos \frac{m\pi}{2} + \sigma \left(q \sin \theta \sin \frac{m\pi}{2} + \cos \theta \left(\cos \phi_0 + iq \cos \left(\phi + \frac{m\pi}{2} \right) \right) \right) \right] \quad (4.57)$$

This is the result for the right drive ($q = 1$) or left drive ($q = -1$) for the shifted up ($\sigma = 1$) or down ($\sigma = -1$) mode. If we want to detect circulation, the $\sin \theta$ term in equation (4.57) will be the most interesting term. This only occurs in m odd terms.

For $m = 2k + 1$ ($k = 0, 1, 2, 3, \dots$) i.e. $m = 1, 3, 5, \dots$ equation (4.57) becomes

$$f_{\sigma q} = FD_0 P_0 e^{i\frac{\pi}{4}(1-q)} \left[1 + \sigma \left(q(-1)^k \sin \theta + \cos \theta \left(\cos \phi_0 - iq(-1)^k \sin \phi_0 \right) \right) \right] \quad (4.58)$$

A frequency independent " signal strength " can be defined as

$$S_{\sigma, q} = \frac{f_{\sigma, q}}{FD_0 P_0} \quad (4.59)$$

Equation (4.59) contains four equations, they are denoted by σ and q . The amplitudes of these signals can be found by multiplying their complex conjugate on both sides of these equations. This gives

$$\left| S_{\sigma,+1} \right|^2 = \left(1 + \sigma \cos \theta \cos \phi_0 \right) \left[1 + \sigma (-1)^k \sin \theta \right] \quad (4.60)$$

$$\left| S_{\sigma,-1} \right|^2 = \left(1 + \sigma \cos \theta \cos \phi_0 \right) \left[1 - \sigma (-1)^k \sin \theta \right] \quad (4.61)$$

Equations (4.60) and (4.61) give some information about the amplitude of the modes. It is easy to see that from those two equations the amplitude of RHD minus mode exactly equals the amplitude of LHD plus mode, and also that the amplitude of RHD plus mode should equal the amplitude of LHD minus mode, but the phases according to these equations are different. These results have been confirmed by our experiment, and are presented in chapter 6.

Now, if we take the ratio of the difference to the sum of the amplitude from equations (4.60) and (4.61) , after some algebra, we finally get

$$\gamma = (-1)^k \delta \sigma \frac{\left| S_{\sigma,+1} \right|^2 - \left| S_{\sigma,-1} \right|^2}{\left| S_{\sigma,+1} \right|^2 + \left| S_{\sigma,-1} \right|^2} = (-1)^k \delta \sigma \frac{R^2 - L^2}{R^2 + L^2} \quad (4.62)$$

Since this result holds for all odd modes, we can eliminate the all of the subscripts to make it easier to see. R and L are the amplitudes due to RHD and LHD respectively. The splitting due to the circulation in the resonator , γ , has been isolated in (4.62).

From the definition of the total splitting,

$$\delta^2 = \gamma^2 + \Delta^2 \quad (4.63)$$

it is easy to calculate the geometrical asymmetry splitting, which is

$$\Delta = \delta \frac{2|RL|}{R^2 + L^2} \quad (4.64)$$

For m even, i.e. $m = 2k$ with $k = 0, 1, 2, 3, \dots$ and doing the same process as above, we eventually get

$$f_{\sigma q} = F D_0 P_0 e^{i\frac{\pi}{4}(1-q)} \left[1 + iq(-1)^k \right] (1 + \sigma \cos \theta \cos \phi_0) \quad (4.65)$$

According to the equation (4.65), there is no " q " dependence in the amplitude of the signal. This result implies that the amplitudes of even modes do not change with the rotational drives applied to a single mode. We can explain this by the configuration of the modes. In order to couple the 90 degree phase relationship in time of the drive plates to the traveling wave, they must line up spatially with a similar phase relationship. This requires that if one drive is over a node, the other drive must be positioned over an antinode. Since the drive plates are rotated 90 degree with respect to each other, this can never happen for even m modes.

The equation (4.65), however, does have a " σ " dependence in sensitive to the circulation. This " σ " dependence goes like $\cos \theta$ which has less sensitivity when θ is small while the " q " dependence in the odd mode goes like $\sin \theta$ which has more sensitivity when θ is small. The experimental results shown in chapter 6 give exactly what we predict here.

Chapter 5 The Experimental Apparatus

This chapter discusses our experimental set up, including the refrigeration system, the third sound resonator, the electronic detection system and the way to acquire data and data analysis. Although this is a standard technique, some improvements have been made in this systems.

5.1. The Refrigeration System

The refrigerator we used in our laboratory is a home made, continuously operating refrigerator. The lowest temperature it can reach is around 30 mK . This was measured by carbon resistors which were calibrated with a ^3He melting curve thermometer [5.1]. A schematic illustration of the low temperature parts of the refrigerator is shown in Fig. 5.1. Cooling is achieved in a container called a mixing chamber. The process can be made continuous by circulating ^3He in the system by a pump at room temperature. Incoming ^3He gas is first pre-cooled and liquefied in the condenser 3 , which is attached to the ^4He pot, at about 1.4K . This temperature is reached by a pumped ^4He stage. The ^3He then enters the still heat exchanger at about 0.7K through a capillary which is called a condenser impedance to prevent gas from passing through and putting a heat load on the still. From there, the ^3He passes through a tubular heat exchanger and step exchangers where it is further cooled by counter-flow liquid before entering the mixing chamber. The mixing chamber was designed to be the place where the most of the cooling process takes place. For temperatures lower than 0.8K, mixtures of ^3He and ^4He separate into ^3He - rich and ^3He - dilute phases. This was discovered by Walters and Fairbank [5.2]. This means that a more powerful cooling process analogous to liquid evaporation is available at low temperatures. As we illustrate the mixing chamber in Fig. 5.1, the upper

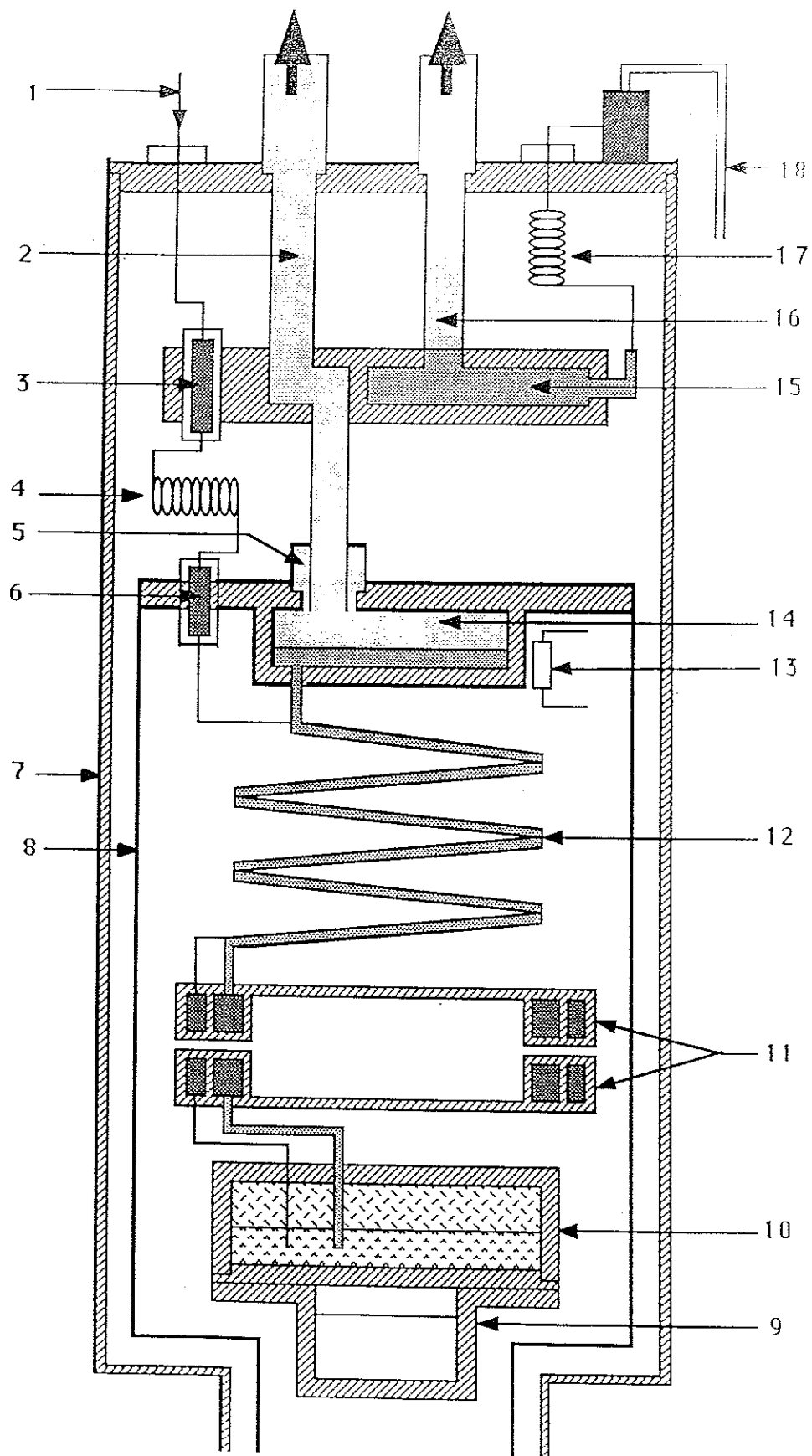


Fig. 5.1. A schematic illustration of a dilution refrigerator built in author's laboratory. 1. Helium -3 return line. 2. Still pump line. 3, 6. Return line condenser. 4. Condenser impedance. 5. Film burner. 7. Vacuum can. 8. Still shield. 9. Cell chamber. 10. Mixing chamber. 11. Step heat exchangers. 12. Counter - flow exchanger. 13. Still heater. 14. Still chamber. 15. Helium - 4 pot. 16. Helium - 4 pot pump line. 17. Helium - 4 pot impedance. 18. Helium - 4 intake.

portion is ^3He - rich phase which plays the part of the liquid. The lower portion is ^3He -dilute phase which plays the part of the vapor, and the osmotic pressure of the solution plays the part of the vapor pressure [5.3]. The driving process for dilution in the mixing chamber is caused by the depletion of ^3He from the dilute solution in equilibrium with the pure ^3He phase. The depletion actually occurs in the still where heat is applied to cause vaporization. At this stage the vapor pressure of ^3He is much higher than that of ^4He , and the gas given off is nearly pure ^3He which returns to the pump at room temperature. We also have put a film burner in the still pump line to avoid ^4He - film flow up the pump tube, since the superfluid helium film can go anywhere. As the ^3He is removed from the dilute solution in the still, ^3He diffuses through the stationary ^4He from the mixer to the still. In the mean time, more ^3He atoms pass through the phase boundary to compensate the loss of ^3He in the dilute phase, thereby cooling the mixing chamber. As this complete cycle goes on, the temperature at the mixing chamber will keep going down until it hits some limitation. The experimental cell chamber (see Fig. 5.2) was attached to the mixing chamber making very good thermal contact with it. The refrigerator was regulated by a heater in the cell chamber and a regulator at room temperature. This refrigerator has run off and on for almost six years and has achieved continuous running for more than three months without any problems.

5.2 The Cell Chamber

The cell chamber is attached to the mixing chamber, the last stage of the refrigerator. Fig. 5.2 shows a cross sectional view of the cell chamber. As we pointed out before, most of the cell chamber was filled by 8.16 grams of Alpha products (series number 00784) $1\text{ }\mu\text{m} \times 5\text{ }\mu\text{m}$ sliver flake. The powder was pressed in volume of about 2.224 cm^3 . A copper disk covered the

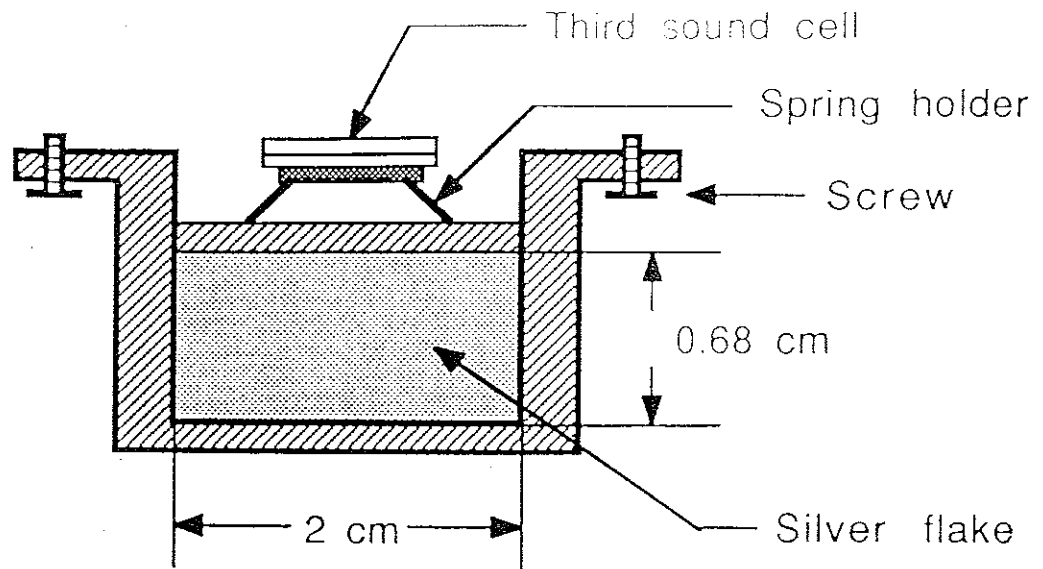


Fig. 5.2 Cross section view of the cell chamber

container by just pressing it in. On the top of the copper piece, the third sound cell was pressed against the bottom of the mixing chamber by a spring - like holder and then slowly tightening with screws as shown in Fig. 5.2. The top surface of the cell was coated by silver to provide good thermal contact with the mixing chamber, thereby minimizing the temperature fluctuations. The filling line, not shown in fig. 5.2, allows helium gas to be added to the chamber.

5.3 The Third Sound Resonator.

Fig. 5.3 shows two views of our third sound cell. It consists of two glass plates separated by a $8 \mu m$ gap and glued together with stycast 1266 epoxy. The inner of cell was coated with gold film about 1000 angstrom thick

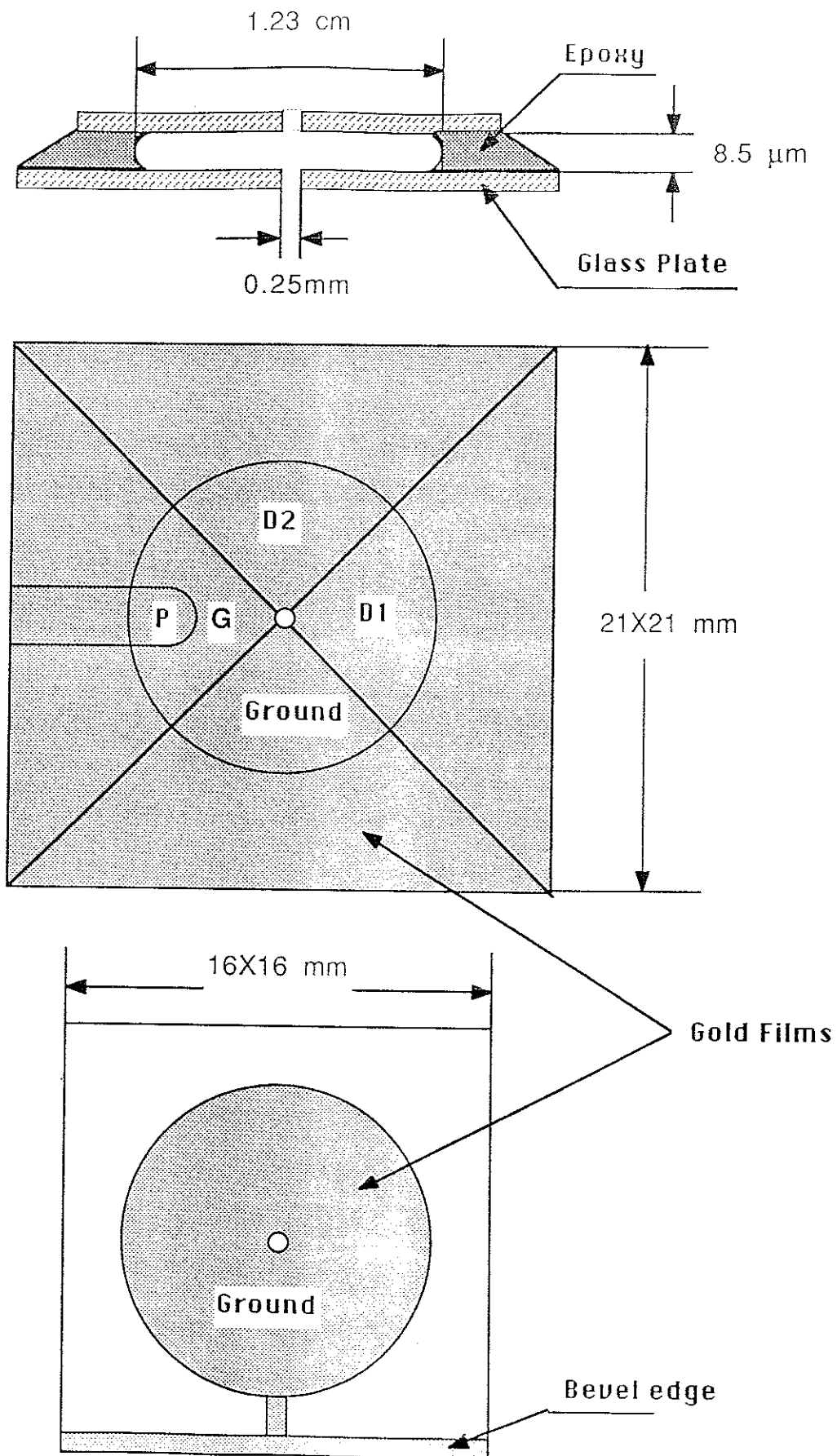


Fig. 5.3 The schematic drawing of third sound resonator.

using a vacuum evaporator. The initial resonator was made of glass coated with silver [5.4] but we finally changed to gold because we found that oxidation effected the cell's surface roughness when we had to leave the cell in the air for the gluing process. The resonator is defined by a bubble in the epoxy whose outer edge was fixed to be a 1.23 cm diameter circle by a small circular etch pit approximately 10 μm deep and 30 μm wide in the one of the plates. Small holes (about 0.25 mm diam) through the center of the circle in each plate allowed for a slight pressure to be applied during the gluing process and for sample access later. The cell electrodes act like a capacitor. Making both the driver and receiver transducers are electrostatic. Both of the electrodes were isolated from the surrounding gold by wires masks during the gold evaporation. Since helium is a dielectric material, the helium film inside the cell is pulled into a region of electric field, which is just the drive region when an oscillating voltage is applied. Changes in film thickness in the pick-up region will correspond to changes in capacitance. Thus the drive and pick-up are directly coupled to the mechanical degrees of freedom in the third sound modes. We have two regions used as drive transducers, one as a ground and one even smaller area which is used as a pick-up transducer. The electrodes were configured to couple efficiently with the $n=1, m=1$ mode but also to overlap considerably with many other modes. More details of these modes configurations can be found in Appendix A . The outer surface of the glass plates were deposited with silver film. This provided good thermal contact while mounted of the chamber. A 0.13 mm inner- diameter capillary provided sample access close to the hole of the cell. This played an important role in trapping a persistent current during filling of helium at low temperature. See Appendix B for the step by step process of making third sound cell.

Third sound was first measured using an optical method [5.5]. In this case, the third sound wave was excited in a horizontal film of helium II by

pulses of infrared radiation. The variations in thickness were measured by an ellipsometer. The disadvantage of this method is that the whole system is very complicated. A few years later, the temperature oscillations were measured by using superconducting bolometers [5.6]. In this way, a heater was used as a generator of third sound waves and a thermometer as a detector. The essence of this experiment is to measure the time of flight between where the wave was generated and where it is detected. This technique gives the third sound velocity only, it can not obtain the height oscillations.

The height oscillations of a wave can be detected capacitively. This work has been done by F. Ellis and co-workers [5.7]. In Fig. 5.4 , a third sound wave is propagated between two capacitor plates separated by a distance. In the drive side, most people use a heater as a generator, but in this work, we made a cell which had several perhaps crucial differences from the other groups. In this cell, an alternating voltage up to $10 V_{pp}$ was applied to the drive electrodes that produced a well defined force on the film at twice the drive frequency. The response of the film can be monitored as a modulation of the capacitance of the pick-up electrodes. This capacitance is converted into an electrical signal by using it in an L-C tunnel diode oscillator circuit phase locked to a reference synthesizer. The phase error is the demodulated signal and is detected with a two phase lock-in amplifier referenced to twice the drive frequency. As the drive frequency is varied, the film responds as a series of resonances, each corresponding to different modes. By recording those resonances, we can get all the information we need to study the superfluid helium films.

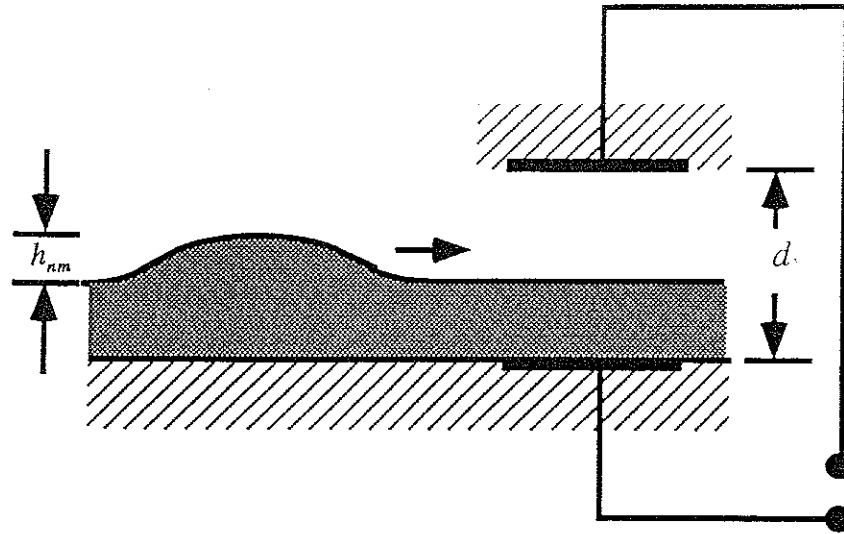


Fig. 5.4 The schematic drawing of capacitive detector.

5.4 The Tunnel Diode Oscillator (TDO)

Oscillators have been used as transducers for making capacitive measurements for a long time [5.8] because the frequencies can be measured with great accuracy. The most important advantages of TDO circuit are the simplicity of the circuit and a remarkable stability, especially at low temperature. In our system, an oscillator driven by a BD-7 tunnel diode was used to measure the third sound signal.

Typical I-V curves are shown in Fig. 5.5. For a tunnel diode at temperatures around 300, 77, and 4.2K. We can easily see that as the temperature is lowered, the properties of the tunnel diode become increasingly temperature independent. The negative slope region corresponds to a negative resistance. The diode is biased

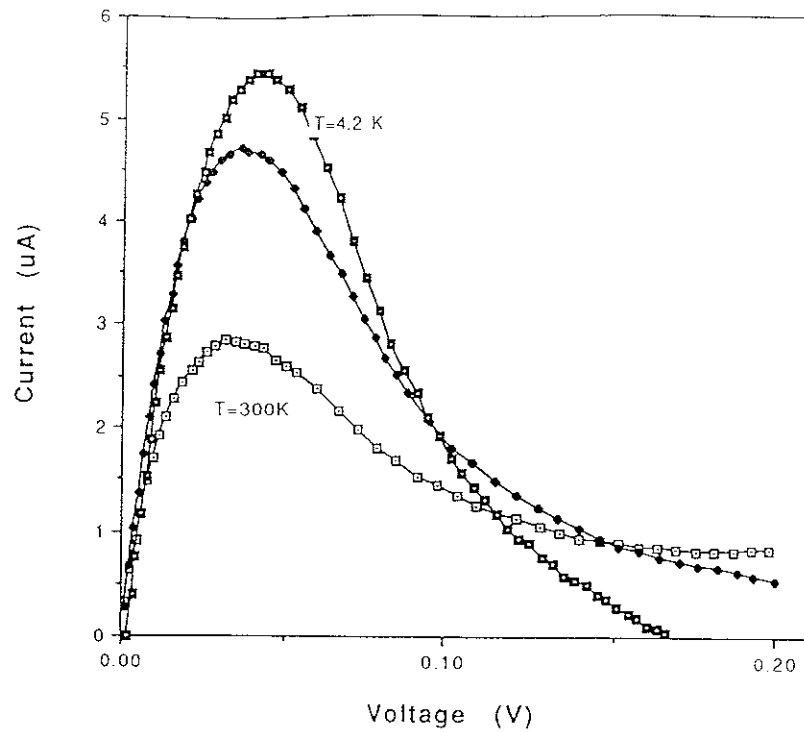


Fig. 5.5 Current-voltage characteristic curves for the BD-7 diode. It appears temperature dependent near room temperature, but changes their properties by only a few parts per million per kelvin below 4.2 K

with a DC current source located at room temperature to the inflection point on the negative slope, so that it acts as a negative AC resistance and therefore, cancels rf power dissipated in the LC circuit. A tunnel diode oscillator (TDO) circuit used in our laboratory is shown in Fig. 5.6 . The DC power is supplied by a room temperature current source and which was connected to the circuit through the same coaxial cable used to carry a small rf output signal from TDO. The inductor L is chosen to give the desired operating frequency of the LC circuit. X refers to the tapping fraction, the value of the tapping fraction X is dictated by the impedance of the LC circuit at resonance, Z_0 . For the desired condition of a critical oscillation, the impedance across the tap, $X^2 Z_0$ must be slightly greater than the effective negative resistance R_n . Since

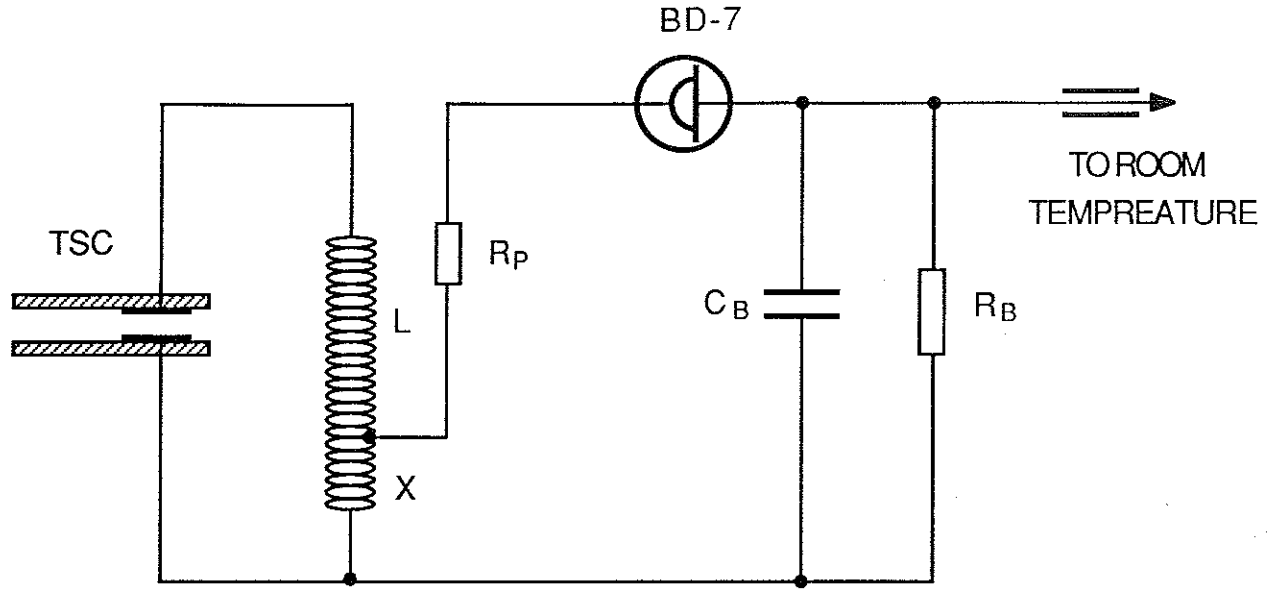


Fig. 5.6 Schematic diagram of a tunnel diode oscillator circuit.

impedance Z_0 and R_n depend on temperature, their values were not accurately known, so it had to be estimated and tested in order to get a proper working condition, R_P was needed to eliminate any parasitic oscillations formed by the lower portion of the inductor and the stray capacity of the diode, C_B was chosen for a good AC ground and R_B provided the proper DC bias for the tunnel diode.

In this work, the determination of all these parameters is dependant on the capacitance of the third sound resonator. The oscillation frequency of the LC circuit is about 76 MHz. This is corresponded to $Z_0 = 16 \text{ k} \Omega$. We then chose the negative resistance of the tunnel diode $R_n = 12 \text{ k} \Omega$, $R_B = 10 \text{ k} \Omega$, $C_B = 200 \text{ PF}$ and $X = 7.1$. The proper DC bias current was chosen to maximize the output signal at the operating temperature. In our system, the DC bias current through the tunnel diode is about $7 \mu \text{ A}$. The circuit oscillated at a bias voltage around 70 mV (see Fig. 5.5). The total bias current

should be then $7 \mu A + 70 mV / R_B = 17 \mu A$. The resistance R_p was usually not included because the wire resistance played the role of R_p which eliminated the parasitic oscillation. We did see the parasitic oscillation when we put the whole bias circuit down onto the mixing chamber. This was caused by having a shorter wire, which decreased R_p . The parasitic oscillation disappeared when we added an extra length of wire into the circuit.

5.5 The Phase Locked Loop. (PLL)

Accurate measurement of the signal frequency changes can be performed using the phase-locking technique. The standard phase-locking loop method uses a feedback loop to catch and follow the signal frequency. The accuracy of this method is limited mainly by the instability of the local oscillator, which is used as the reference signal. In order to minimize this error, a modification of this phase-locking technique has been used.

A block diagram of a standard phase-locked loop (also called the demodulator) is shown in Fig. 5.7. The mixer is a nonlinear circuit element that takes two input signals of frequency f_{TDO} and f_{VCO} and outputs a signal which consists of both the sum and difference of those frequencies. This signal then passes through a low pass filter which eliminates the sum frequency signal and the output goes into a voltage controlled oscillator (VCO) whose output frequency depends on the voltage input to it. If the frequencies f_{TDO} and f_{VCO} are very close, it is possible for the loop to "lock" to the f_{TDO} . This means that the frequency of the VCO matches and follows the frequency of the TDO.

In principle, this demodulator can be used in any oscillator system to convert the variations of the radio frequency to a proportional voltage variations which can be easily recorded. We made a significant

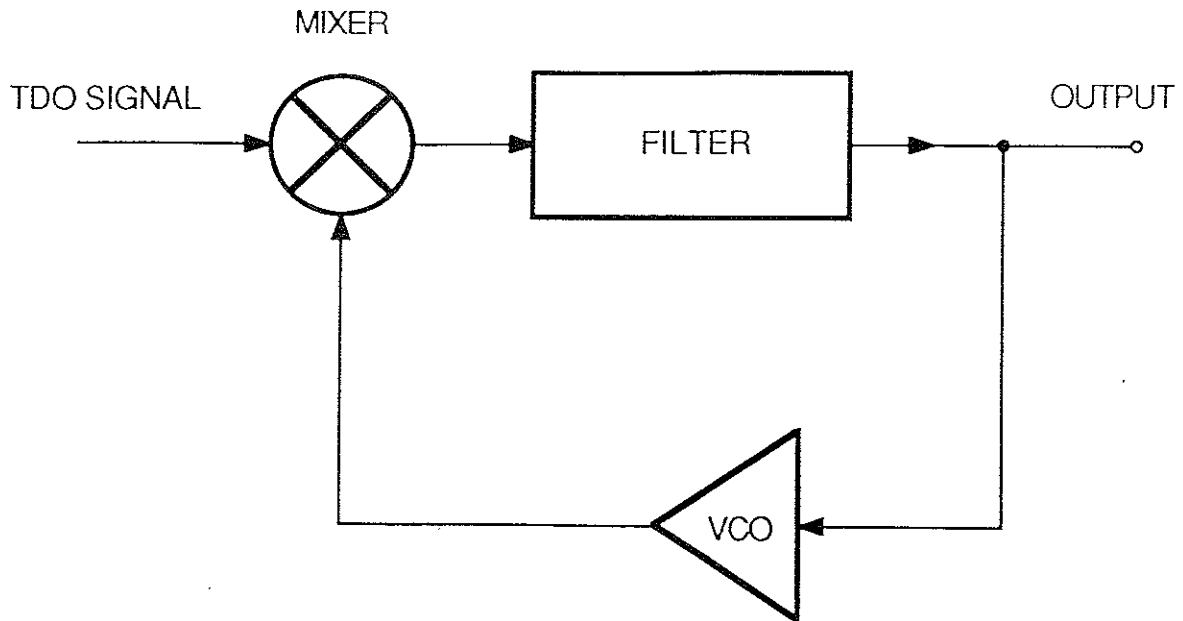


Fig. 5.7 Block diagram of the standard demodulator.

improvement to the PLL in order to satisfy our special requirements.

The PLL is pictured in Fig. 5.8. The difference between this loop and standard PLL is that instead of sending feed back signal directly to a VCO, it is sent back to the TDO which acts as the VCO. This gives us a fixed, and more stable reference oscillator. Since the frequency of TDO is dependent on the bias voltage (see Fig. 5.9) and we put the feedback signal together with the bias current in one cable line, it slightly changed the bias voltage, and hence leads to a change in the frequency of TDO. The loop is in a "locked" condition when the feedback signal cancels variations due to capacitance (This is identical to the frequency variations according to Fig. 5.9).

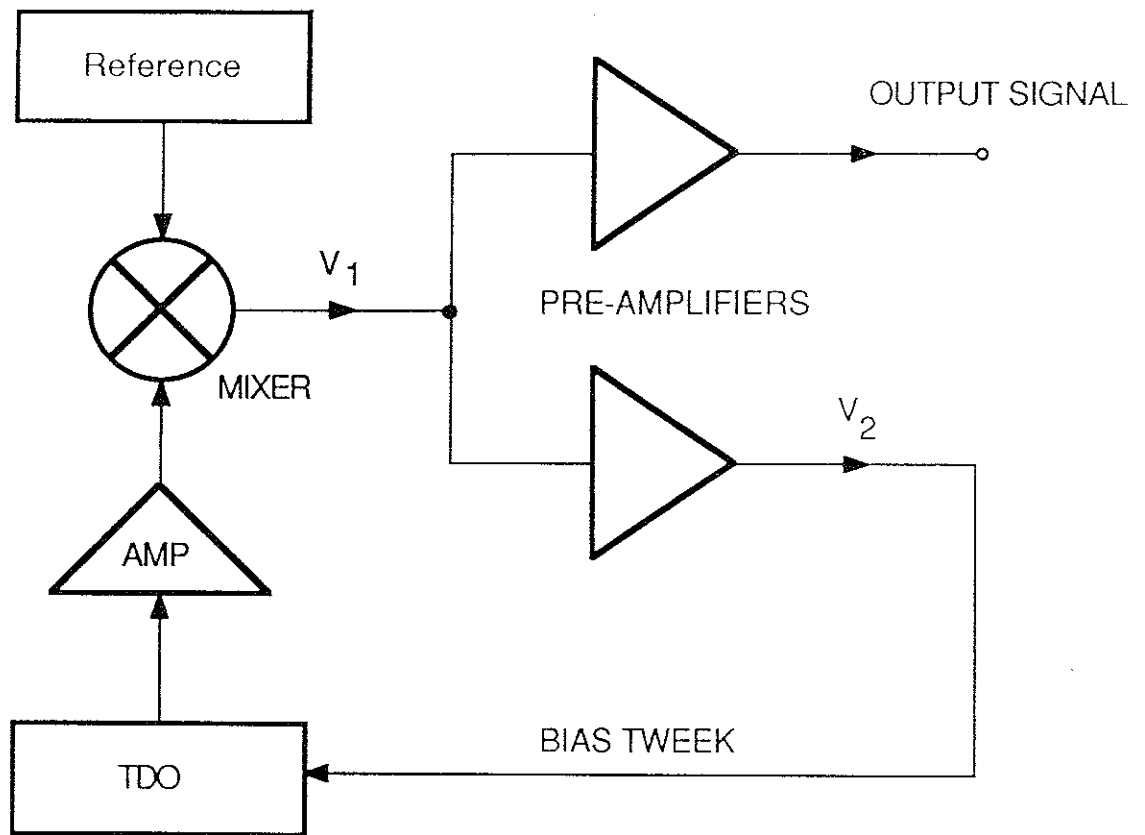


Fig. 5.8 Block diagram of a phase-lock loop (PLL) used in author's laboratory.

The frequency of TDO can be written as:

$$f_{TDO} = f_0 + \frac{\partial f}{\partial C_p} \Delta C_p + \frac{\partial f}{\partial V_{tweak}} V_2 \quad (5.1)$$

where f_0 is the natural oscillation frequency of TDO. The second term in equation (5.1) is the frequency deviation due to the capacitance change in the TDO. This capacitor is the detector of our third sound resonator, the third term is the effective VCO sensitivity.

If we assume :

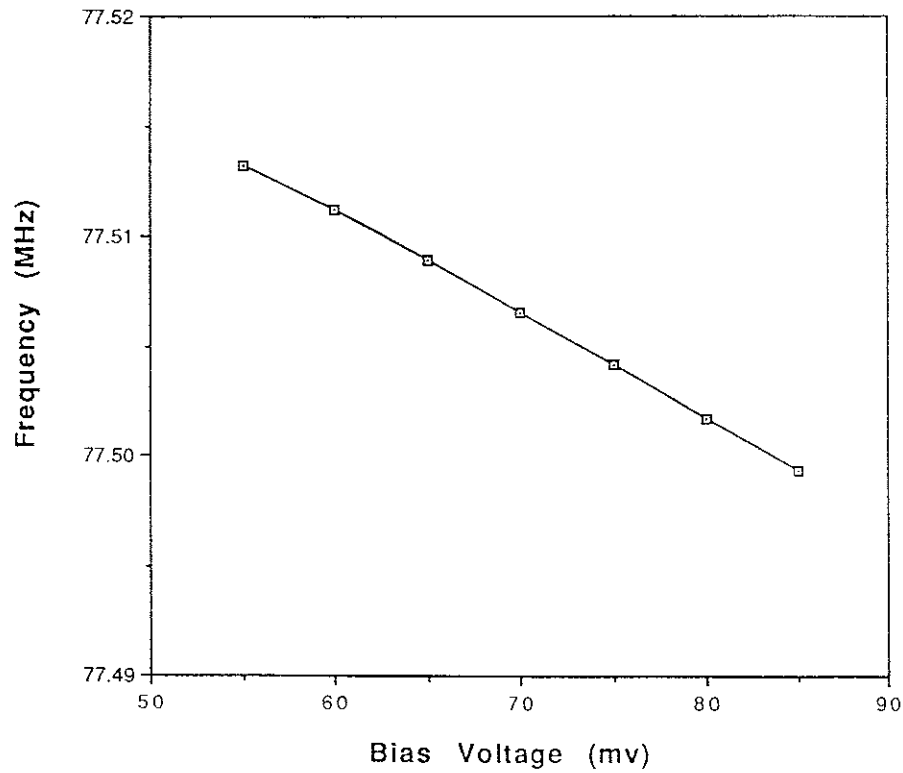


Fig. 5.9 Measurement of the bias voltage versus the frequency of tunnel diode oscillator (TDO).

$$f_{TDO} = f_0 + \Delta f \quad (5.2)$$

we have

$$\Delta f = \frac{\partial f}{\partial C_p} \Delta C_p + \frac{\partial f}{\partial V_{tweek}} V_2 \quad (5.3)$$

we can always introduce a time-dependent part like this :

$$\Delta f \equiv \Delta f \cdot e^{-i\omega t} \quad (5.4)$$

therefore,

$$V_1 = -2\pi V_0 \int_0^\infty \Delta f dt = \frac{i 2\pi V_0}{\omega} \Delta f \quad (5.5)$$

where V_0 is amplitude of mixed signal. Obviously,

$$V_2 = g V_1 \quad (5.6)$$

from Fig. 5.8 , g is just the gain factor between output V_2 and V_1 . So,

$$\Delta f = \frac{\partial f}{\partial C_p} \Delta C_p + \frac{\partial f}{\partial V_{tweek}} \cdot g \cdot \frac{i 2\pi V_0}{\omega} \Delta f \quad (5.7)$$

solving for Δf , we have :

$$\Delta f = \frac{\frac{\partial f}{\partial C_p} \Delta C_p}{1 - \frac{2\pi i V_0 g}{\omega} \cdot \frac{\partial f}{\partial V_{tweek}}} \quad (5.8)$$

And finally,

$$V_1 = \frac{2\pi V_0 \frac{\partial f}{\partial C_p} \Delta C_p}{-i\omega - 2\pi V_0 g \frac{\partial f}{\partial V_{tweek}}} \quad (5.9)$$

In the case of tight feedback, this corresponds to low frequency and high gain, we have,

$$V_1 = - \frac{\frac{\partial f}{\partial C_p} \Delta C_p}{g \frac{\partial f}{\partial V_{tweek}}} \quad (5.10)$$

$$V_2 = - \frac{\frac{\partial f}{\partial C_p} \Delta C_p}{\frac{\partial f}{\partial V_{tweek}}} \quad (5.11)$$

In the case of loose feedback, this corresponds to low gain at signal frequency and high gain at DC. Therefore,

$$V_1 = \frac{2\pi i V_0 \frac{\partial f}{\partial C_p} \Delta C_p}{\omega} \quad (5.12)$$

In either case, the output signal is directly related to the frequency changes due to the pick-up capacitance change.

The oscillator used as a reference here was an HP 8656B 0.1 - 999 MHz signal generator. The mixer was also made by Hewlett-Packard with series

number HP 10534A.

5.6. The Detection System of Third Sound Signal.

Fig. 5.10 shows the detection system of third sound cell. The Hewlett Packard (HP) 3325A frequency generator produced a voltage signal at a particular drive frequency that was run through an attenuator and a phase shifter (if applicable) to the drive parts of the third sound cell. The drive frequency was slowly swept by the frequency generator controlled by an HP 86B personal computer until a third sound resonance was excited in the cell, at twice the drive frequency. The TDO oscillator at pick-up side had a responds with a modulated frequency. This signal was sent to a SR440 RF amplifier, then to the mixer. The other input to the mixer come from the HP 8656B reference oscillator. The phase error signal was then split, entering two pre-amplifiers, as shown in Fig. 5.10. The pre-amplifier # 1 played the role of low pass filter and amplifier. Its output signal was sent back as feedback to the TDO as described earlier. The pre-amplifier # 2 was adjusted to allow only those frequencies in which we were interested in to be fed through to a two phase lock-in amplifier referenced to the output of the drive oscillator. The lock - in was set to monitor its input for a signal at twice the drive frequency. The amplitude of the this signal to the lock-in amplifier changed as the drive frequency was swept through a resonance. The output of the lock-in amplifier was recorded by a computer.

Fig. 5.11 shows the first detection of a third sound signal. The double resonance corresponds to a Doppler splitting of the third sound signal. Fig. 5.12 shows an actual resonance recorded by the computer. The marked points are the actual data points and the two solid curves are the fitting results which correspond to an in-phase and a quadrature signal. This data can be fit to Lorentzians to determine the relevant parameters, like the

quality factor Q , the resonance frequency f_0 , the amplitude of the resonance A , phase ϕ etc.

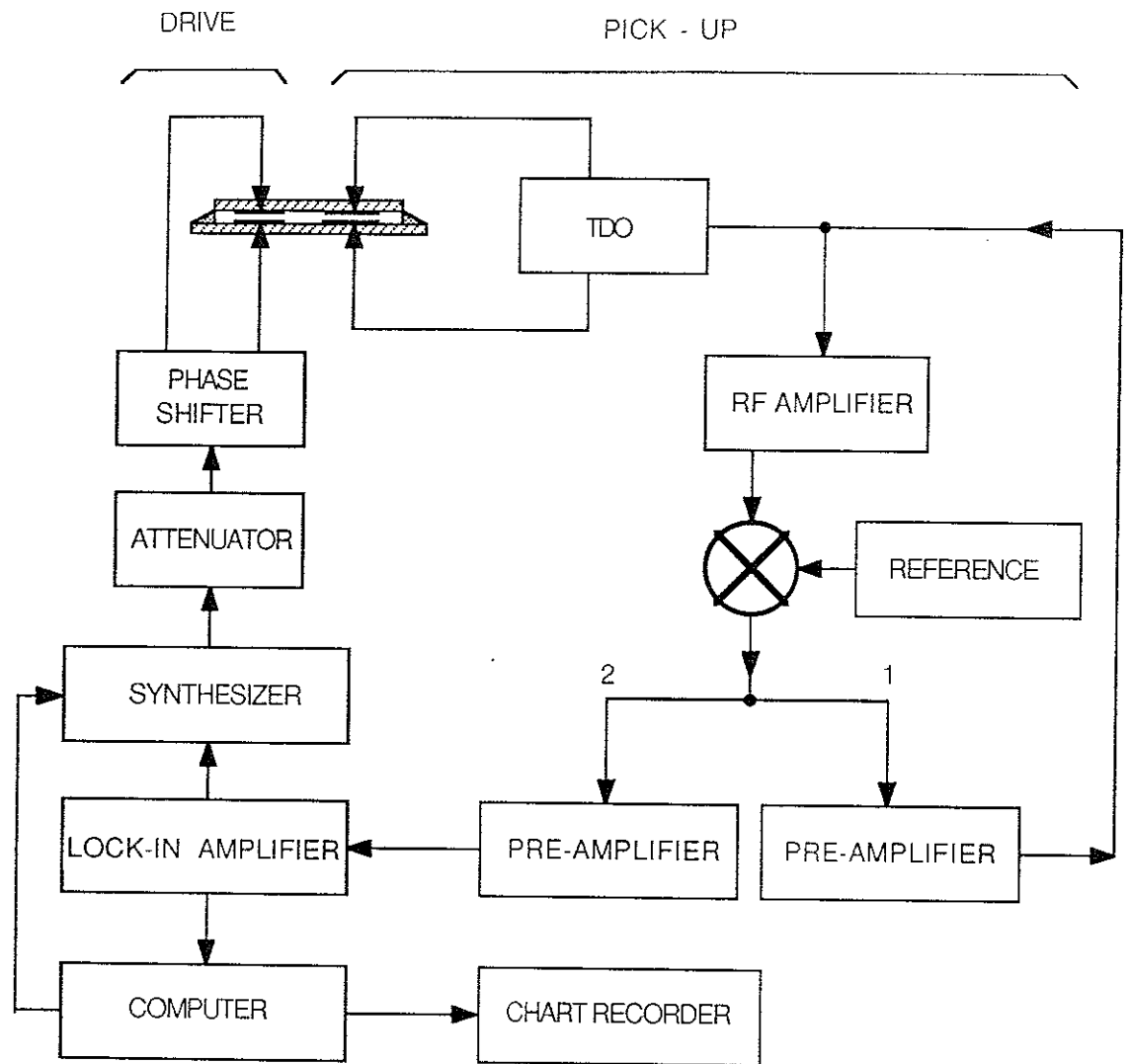


Fig 5.10 . Block diagram of third sound resonator detection system.

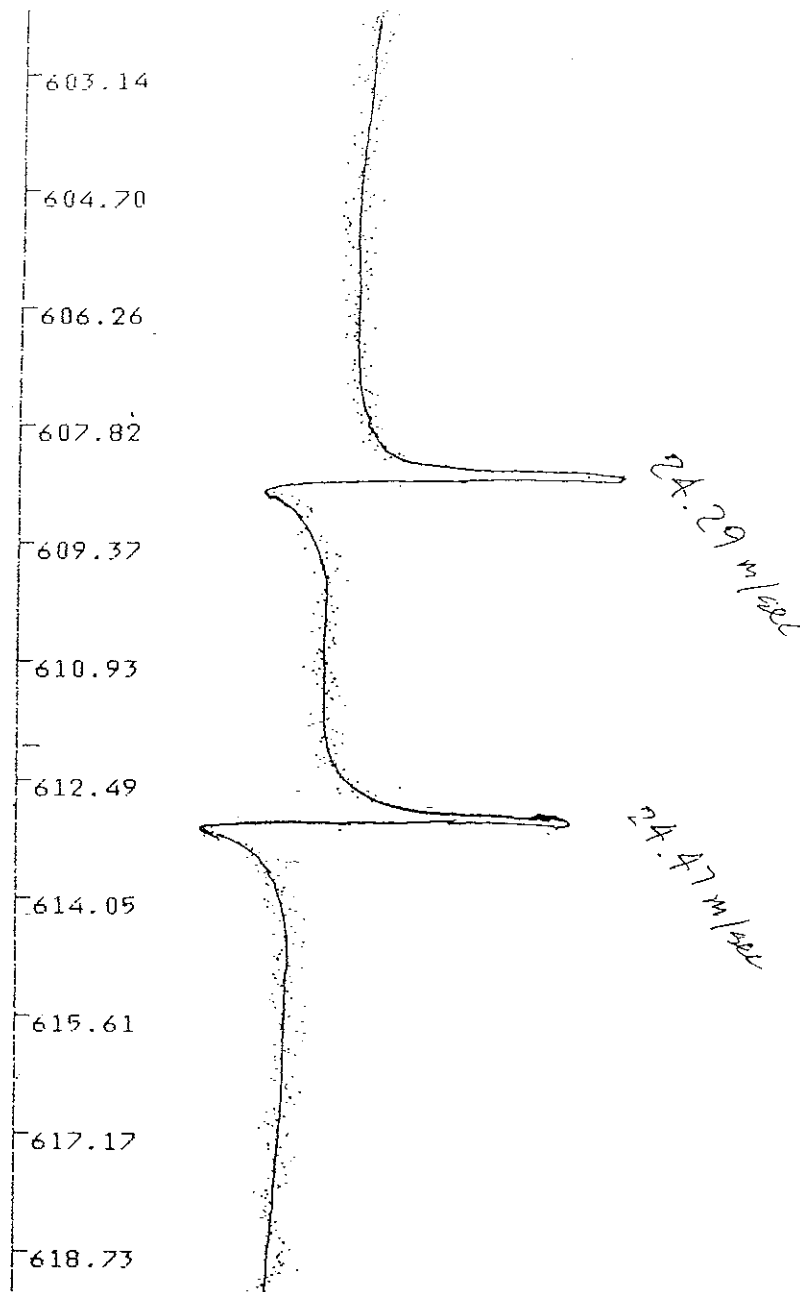


Fig. 5.11 The first split third sound signal recorded by a chart recorder.
The vertical scale is frequency.

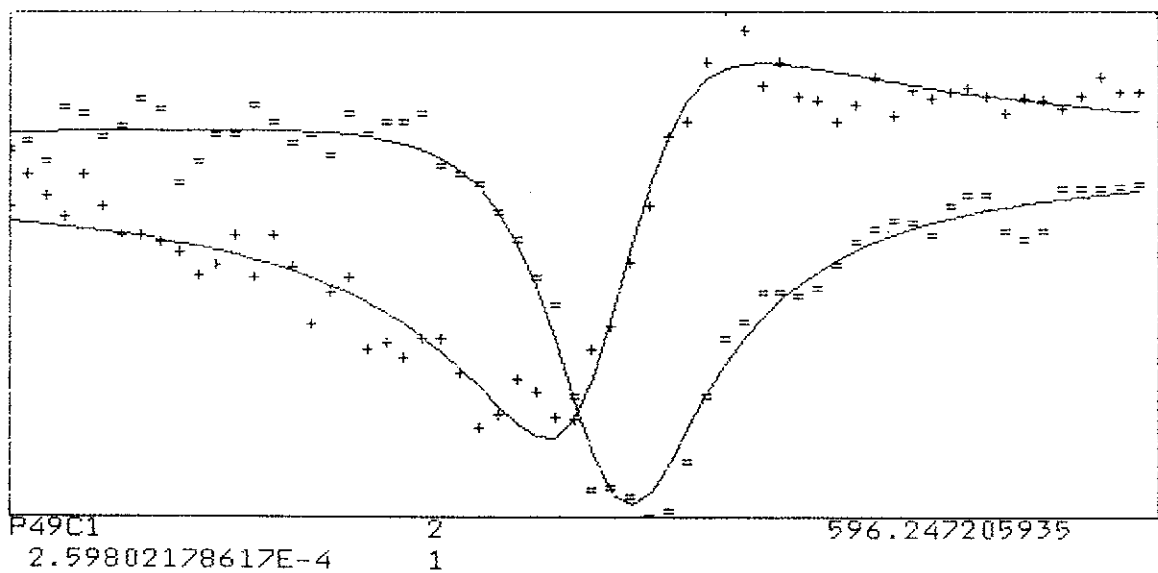
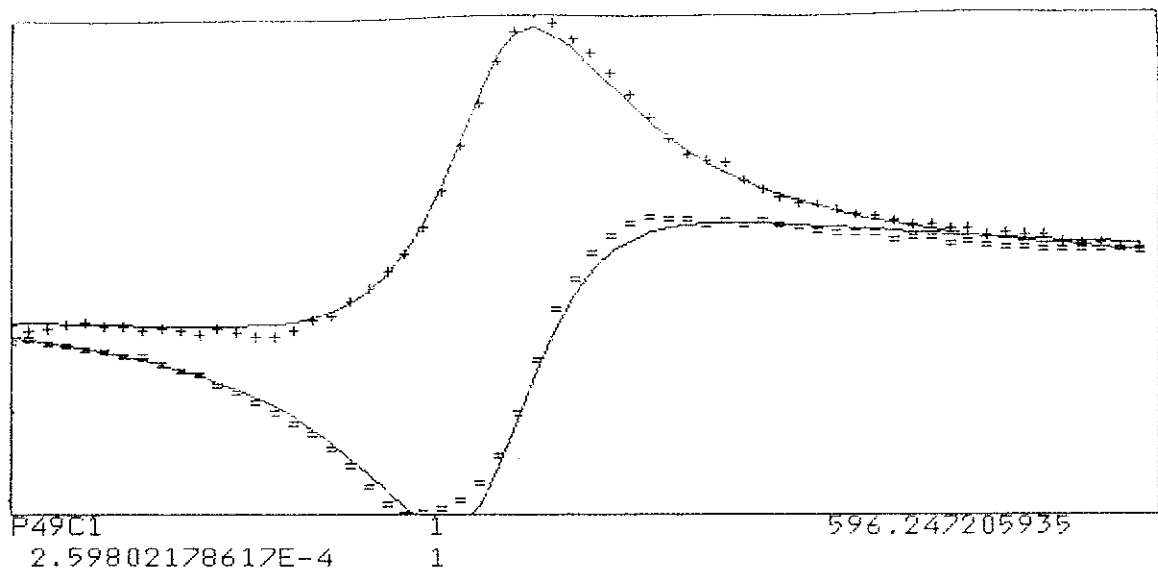


Fig. 5.12 Shows a resonance excited as the driven frequency sweeps through. The marked points and the actual data points "+" and "=" correspond to the real and imaginary part of the resonance, respectively. The solid lines are the fitting results.

Chapter 6 Results and Discussion

This chapter discusses our experimental results and some conclusions. We have measured superfluid circulations from three visible third sound modes and also detected a change in direction of these circulations after a warm up and cool down process. The mechanism of geometric asymmetry shift of modes will also be discussed.

6.1 Results from Non - Rotational Drive Technique.

From chapter 3, the effect on a resonant frequency in the presence of both circulation and geometric asymmetry splitting is

$$\omega = \omega_0 \left[1 \pm \sqrt{\left(\frac{\gamma_{nm} v_0 k}{\omega_0} \right)^2 + \Delta_m^2} \right] \quad (3.38)$$

It is important to note here that the geometrical splitting from (3.38) is a fixed ratio with respect to the two resonant frequency whereas the Doppler shift is a fixed difference. Because of this, equation (3.38) provides a clear

separation of the two effects via a plot of $\left(\frac{\Delta f}{f} \right)^2$ vs. $1/f^2$, assuming v_0 remains constant during gradual changes in film thickness (This is indeed true if you add the sample very slowly and would not change any film state). Hence the resonant frequency will change gradually, Also the trapping of flow velocity during a thickness change of this manner has been verified in other studies of persistent currents [6.1, 6.2] and in this thesis also. This allows us to investigate the presence of a circulation without a controllable method for changing the flow state. Such a plot is shown as Fig. 6.1.

From this data, one can easily find that the geometrical asymmetry splitting which was about $\Delta = 9.4 \times 10^{-4}$, and the velocity at the perimeter was $v_0 = 3.49 \text{ cm/s}$ based on the measurements of slope and intersection.

With this result, let us look at the data. Fig. 6.2 shows the $n=1$, $m = \pm 3$ modes observed with a third sound velocity of about 24 m/s. Shown are two different shifts of 14 % and 37 % calculated from equation (3.5) with $\gamma_{31} = 1.09$ for these modes. To a velocity at the perimeter v_0 of 4.86 cm/s in (a) and 12.25 cm/s in (b). In this case, between the two scans

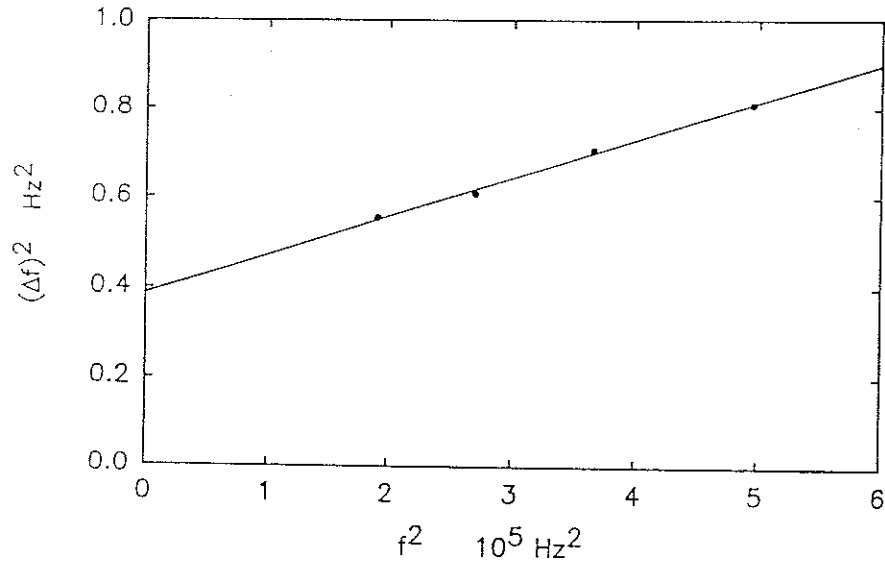


Fig. 6.1 The observed frequency shifts plotted vs resonant frequency as the film was thickened (frequency lowered) with a fixed flow state. Squaring the frequency scales gives a straight line plot expected from Eq. (3.38). For these data, the intercept gives a perimeter flow speed around $v_0 = 3.49 \text{ cm/s}$ and the slope gives the asymmetry shift $\Delta = 9.4 \times 10^{-4}$. The size of the fit circles represents the uncertainty of the data.

shown, the experiment was warmed up to 4 K, which is way above the superfluid transition temperature, part of the sample was removed, then cooled back down and the sample rapidly replaced. The resonator is located in the flow path between the fill capillary and the reservoir so trapping of a persistent current during this process is not surprising. Although the mere presence of a persistent current is a matter of chance, since we have no controllable way to produce it at this time (Later in this chapter, you will see that we do have some way to control this by controlling the cooling rate during warming up and cooling down process.) , history- dependent splitting occurring at the same third sound velocity rules out purely geometrical

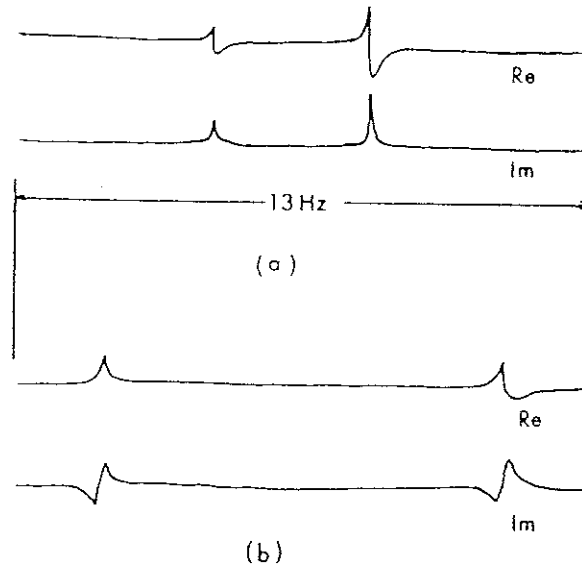


Fig. 6.2 Third sound resonances showing the circulation induced splitting of the $n=1, m=3$ mode. The sound velocity in both cases are 24 m/s yet the splitting is different reflecting different flow states. The resonance will remain split even with no flow because of geometrical asymmetry.

asymmetries. Geometrical asymmetry splitting should not change in the process warming up and cooling down. Further data confirms this in section 6.6. Based on the geometrical splitting we measured from Fig. 6.1 .

$\Delta = 9.4 \times 10^{-4}$, one can estimate from Fig. 6.2 that the splitting are 35 % rotational in (a) and 74 % in (b) . Clearly (a) was dominated by the geometrical splitting since the flow speed is small and (b) was dominated by the circulation splitting. This also accounts for the smaller splitting [Fig. 6.2 (a)] showing a more noticeable difference between the amplitudes of the split pair. The standing wave modes overlap the transducer differently according to the orientation of the asymmetry. This implies that (a) would have more standing wave components and this is indeed true from the above analysis. The rotating states couple to the transducer equally as shown in Fig. 6.2 (b).

We can now propose one possible explanation for the lack of splitting in other resonator experiments. If there is no degeneracy at $v_0 = 0$ (this means a geometric splitting at $v_0 = 0$), the circulation splitting is then second order in v_0 and would be visible only at larger velocities. There are two groups that claimed they did not observe mode splitting during their experiment. One is at UCLA and the other at Rutgers University, [3.4 , 6.2]. The cells they used have slight differences from ours and the detecting techniques are different. If they had their expected splitting about some order or even smaller than the geometrical splitting, there were definite difficulties in seeing the circulation splitting. This is quite possible, considering that this is still nine times smaller than the resonator in this work. Now, question arises : If the asymmetry is dominating, where is the other mode ? In other words, why could they not see the geometrical splitting ? Considering the typical size of the shift (3.24) , it is somewhat surprising that geometrical splitting of a circular resonator has not been previously reported. We believe the transducers themselves may be the cause of the geometrical asymmetry. They could force the modes into the

standing wave configurations, by either directly perturbing the uniformity of the substrate by their mere presence or indirectly through heating, as would be the case with thermal drives and pickups. If so, the modes would naturally split into one strongly coupled to the transducers and the other weakly coupled and hence not visible. This would be even more likely in a resonator where the transducers drastically differ from the surrounding surface.

One other explanation may be related to the topology of the resonator surface. In a resonator with one hole or no hole at all, the behavior of the velocity field near the $1/r$ singularity will undoubtedly disperse the flow field, since singly quantized vortices are the preferred state. Uncertainties in this regard are avoided in a multiply connected resonator such as this one used, where the singularity is avoided completely.

6.2 Results for Rotational Drive Technique.

The setting up of the rotational drive technique has been given in chapter 4. Now, we can record a resonance by scanning through it with drive on. Since the relay in the phase shifter box can reverse the two drives from one to another between scans, we can actually record four resonances in one group, that is, right hand drive for both plus and minus modes and left hand drive for both modes. The phase shift is not readjusted between scans because the phase change here is negligible. The behavior of the data were exactly matched our predictions. Fig. 6.3 shows an actual data file which was scanned through a resonance in four different situations by a two phase lock-in amplifier. From Fig. 6.3, if you compare two different drives acting on the same mode, obviously the left hand drive plus mode signal is bigger than the right hand drive plus mode signal (see (a) and (b) in Fig. 5.3). But for the minus mode this is exactly opposite (see (c) and (d)). This can be explained by

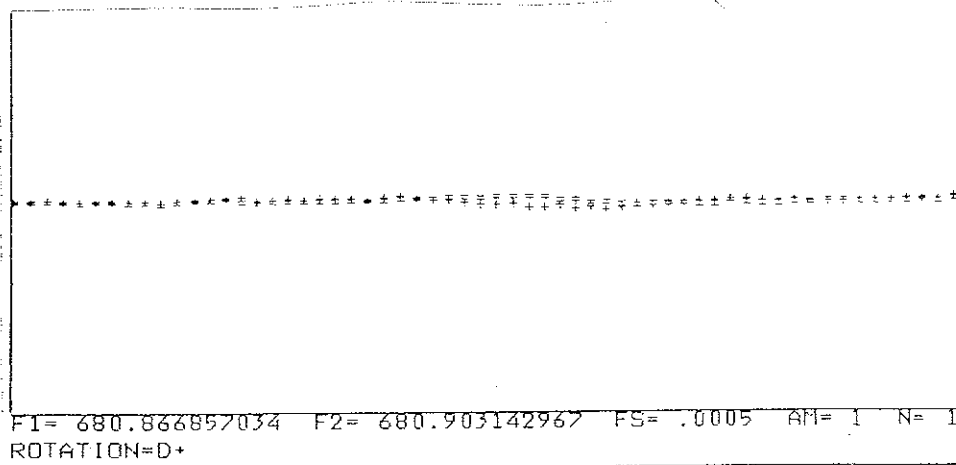
thinking that the left hand drive accelerates the plus mode, i.e. they are in the same direction and therefore decelerate the minus mode, so the left hand drive minus mode signal should be smaller. These results are also consistent with the calculations made in chapter 4. It is easy to see from equations (4.60) and (4.61) , that the amplitude of RHD minus mode is exactly equal to the amplitude of LHD plus mode, and also the amplitude of RHD plus mode is equal to the amplitude of LHD minus mode, but with different phases. Typical data is shown in Fig. 6.3 where (b) , (c) corresponds with the first case as the analysis above and (a) ,(d) for the second case. They exactly match the predictions we made.

This behavior was also seen for higher order third sound modes, such as $n=1, m=3, 5$ modes. This will be discussed later.

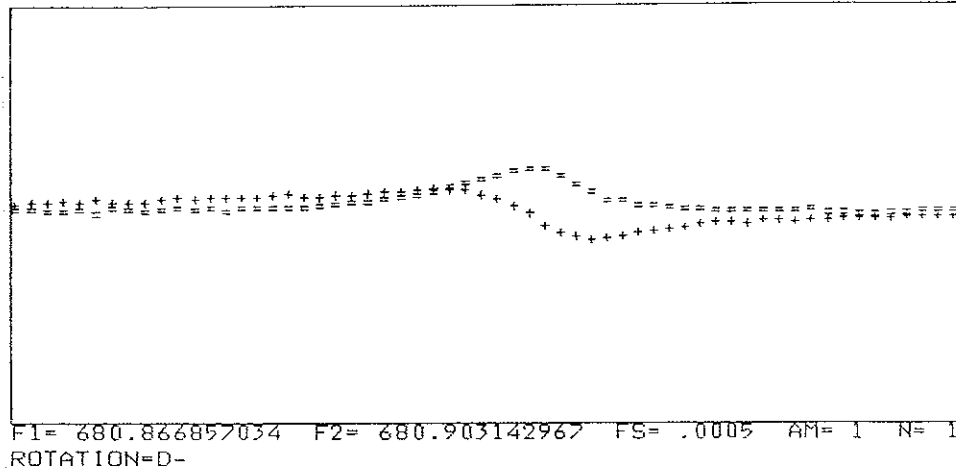
Now, we are going to describe these four resonants (They correspond to the plus and minus modes with right and left hand drive) and some interesting results from our calculations. The whole process can be explained as follows: The third sound resonant was recorded by a HP computer and fitted later by a fitting program in our mainframe computer (see Appendix E for details of the program). After we were convinced that the fitting curves match up to the actual data points (see, for example, Fig. 5.13), we then used equations (4.62) and (4.64) to calculate the actual splitting due to the circulation and geometrical asymmetry. As you may have noticed before, the total splitting is defined by

$$\delta^2 = \gamma^2 + \Delta^2 \quad (4.63)$$

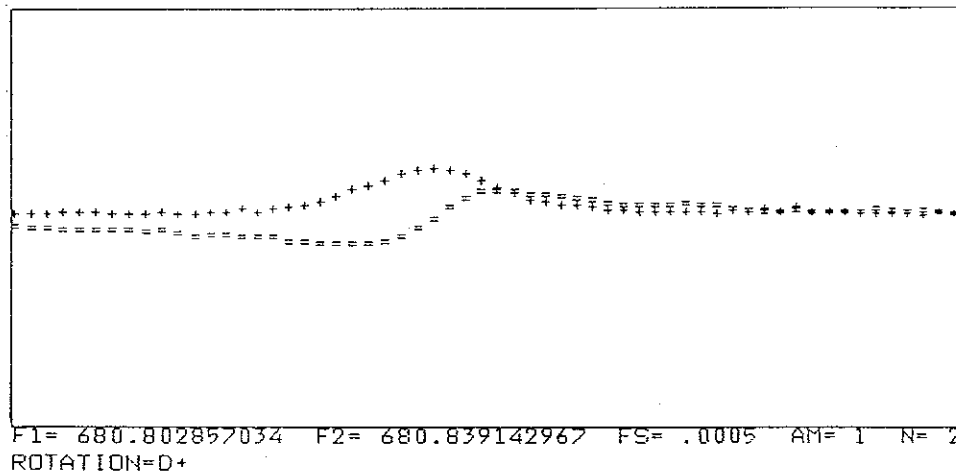
It also can be determined by the splitting of the two frequencies. The definition for the total splitting δ is :



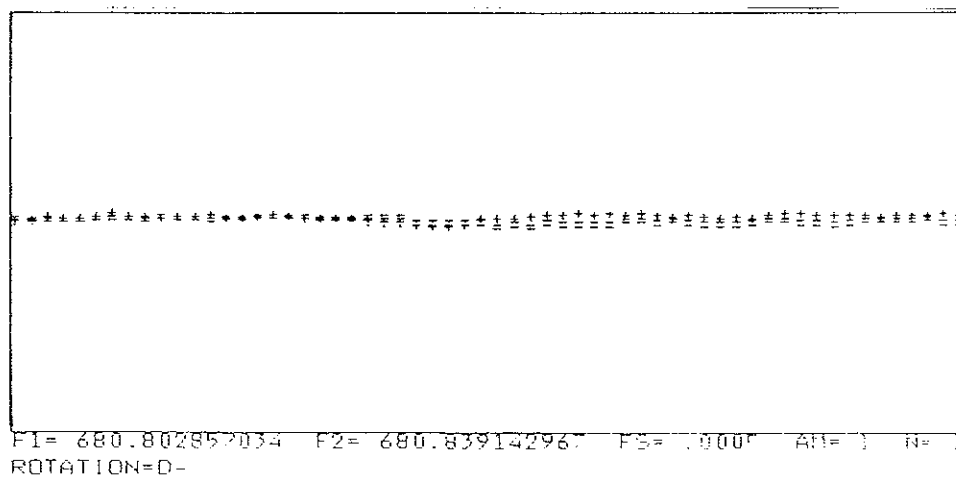
(a)



(b)



(c)



(d)

Fig. 6.3 The actual data file which was recorded by scan through the resonant at four different situations. The two curves in each resonant represent the in - phase and quadrature signal from the output of the lock - in amplifier. (a) RHD plus mode. (b) LHD plus mode. (c) RHD minus mode. (d) LHD minus mode.

$$\delta = \frac{f_+ - f_-}{f_+ + f_-} \quad (6.1)$$

where f_+ and f_- represent the frequencies of $\sigma = 1$ and $\sigma = -1$ mode respectively.

Using equations (4.62) , (4.64) and (6.1) , the mode shift due to the circulation and the geometric asymmetry splittings are calculated. Note, that in these calculations only part of the information from the recorded resonance is used, i.e. the amplitude of each resonance associated with the different drive situations. It is easy to calculate the circulation and the amplitude of geometric asymmetry shift, but there is no way of finding out the phase shift of geometric splitting, ϕ_0 . Only part of the theoretical calculation (4.62) can be tested using the experimental data. To convince ourselves that the results from equations (4.62) and (4.64) are reasonable, we did another analysis which started from equation(4.58). Obviously, (4.58) represents four equations. They correspond to the right and left drive, plus and minus modes respectively. There are three unknowns that we have to solve. They are A , the amplitude of the signal; θ , defined as

$$\sin \theta = \frac{\gamma}{\delta} \quad \text{and} \quad \cos \theta = \frac{\Delta}{\delta}$$

which represent circulation and geometric shift of the modes. ϕ_0 , is the geometric perturbation orientation. To solve these four equations with three unknowns is not easy. What we did the analysis is the following processes.

First, we recorded four frequency scans. After we fitted them with proper fitting parameters, we got the amplitude and phase for each resonance. They actually represent four points in the complex plane. To determine how well these points describe the resonances that occurred inside the resonator, consider the following question: Are the phases we measured the

actual phases of the resonances inside of the resonator ? The answer is no. In fact, the detection system introduces a phase shift. Therefore, the calibration of a phase lock loop (PLL) has been set up to measure both this phase shift and the amplitude gain each time we take data. This is discussed in Appendix E . Furthermore, since our resonant frequency is double the drive frequency (This is because the drive force is double the drive frequency), the lock-in amplifier used to measure the amplitude and phase of the resonance has to be set at $2f$ mode. The lock-in amplifier used to calibrate the PLL signal was set at f mode using an artificial signal to replace the real signal from the cryostat during the calibration. The lock-in reading between $2f$ mode and f mode has been found to have a 90 degree phase difference. Take this into account, the real signal at resonance is :

$$\text{Realresonance} = \frac{\text{Measured signal}}{\text{PLL calibration}} e^{i\frac{\pi}{2}}$$

Remember that the PLL calibration signal is a complex calibration measurement, The real phase of the resonance inside the resonator will be:

$$\text{Real Phase} = \text{Fitting Phase} - \text{Arctg}^{-1} (\text{PLLY}/\text{PLLX}) + 3.1415926/2$$

where PLLX (Y) is the X (Y) component of the lock-in reading. The fitting phase comes from the fitting results. The program used to do the fittings can be found in Appendix E.

Up to now, we have the "right" four data points in the complex plane. We also have four theoretical points from equation (4.58). By choosing the parameters (A, θ, ϕ) properly, we can let these four theoretical points get as close as possible to the four data points in the complex plane, respectively. A computer program which minimizes the mean square distance between

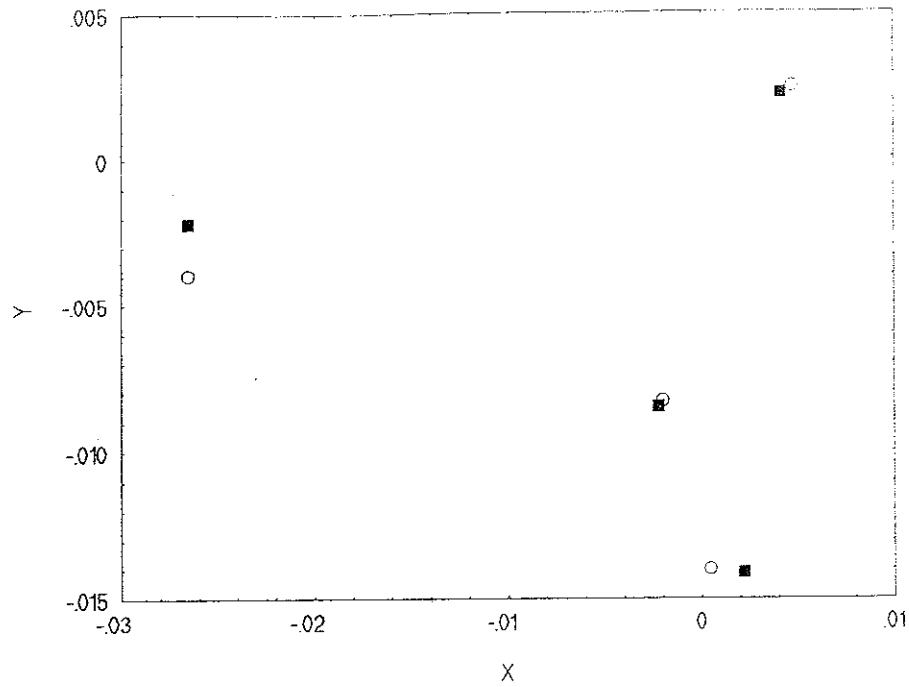


Fig. 6.4 A comparison of actual data points (open circle) with theoretical fitted points (dark square) .

corresponding points and then finds out the three parameters has been used in this analysis. Fig. 6.4. gives an example. The four open points are the actual data points, the four dark points are the theoretical ones calculated by the computer. Although they are not perfectly matched up, it is the best fit given by the computer. Once we have θ , it is not difficult to find γ and Δ according to the definition of θ . The measured and theoretically calculated amplitudes are consistent in (3,1) and (5,1) modes, but there is some deviation in (1,1) mode. The inconsistency in the (1,1) mode is within our experimental error limits since (1,1) mode has the greatest geometric asymmetry shift. This results in less sensitivity in detection of circulations

in the resonator.

Whenever possible both measured and theoretically calculated values are presented together.

6.2.1. Same γ for slow increase of film thickness.

Fig. 6.5 shows that a change in film thickness (hence third sound velocity) has almost no effect on the circulation speed for the (1,1) mode. Fig. 6.6 and Fig. 6.7 show basically the same things for the (3,1) and (5,1) mode respectively. Each point in the figures represents an average calculated from data taken by scanning through resonance with different driving voltages. All modes show that if we slowly increase the film thickness, the

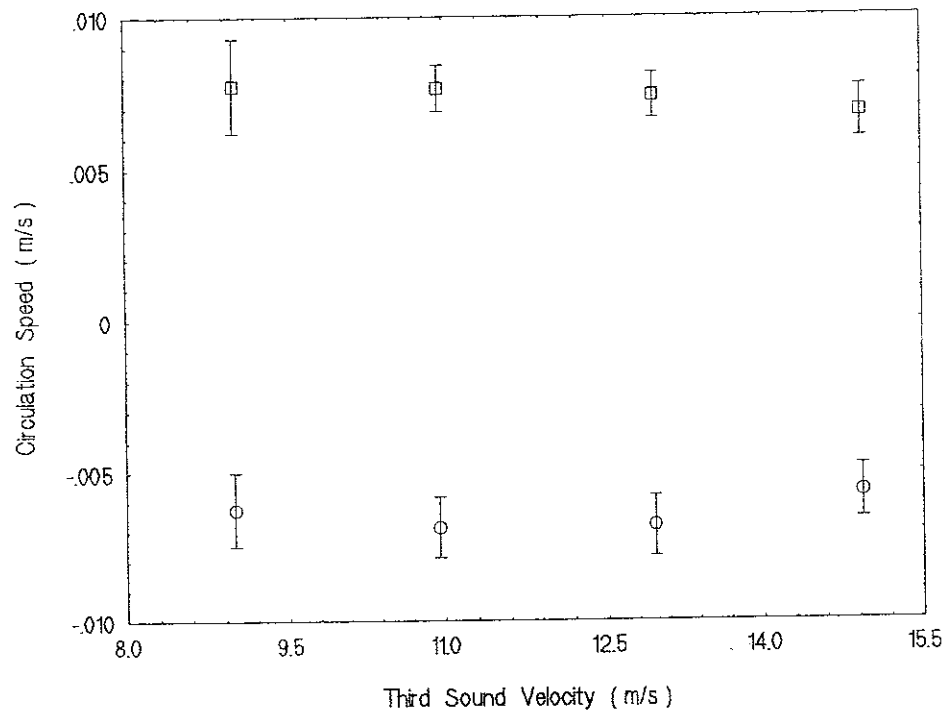


Fig. 6.5 A measurement of circulation with slowly changing of the film thickness for (1,1) mode. The square and circle points correspond to plus and minus mode respectively.

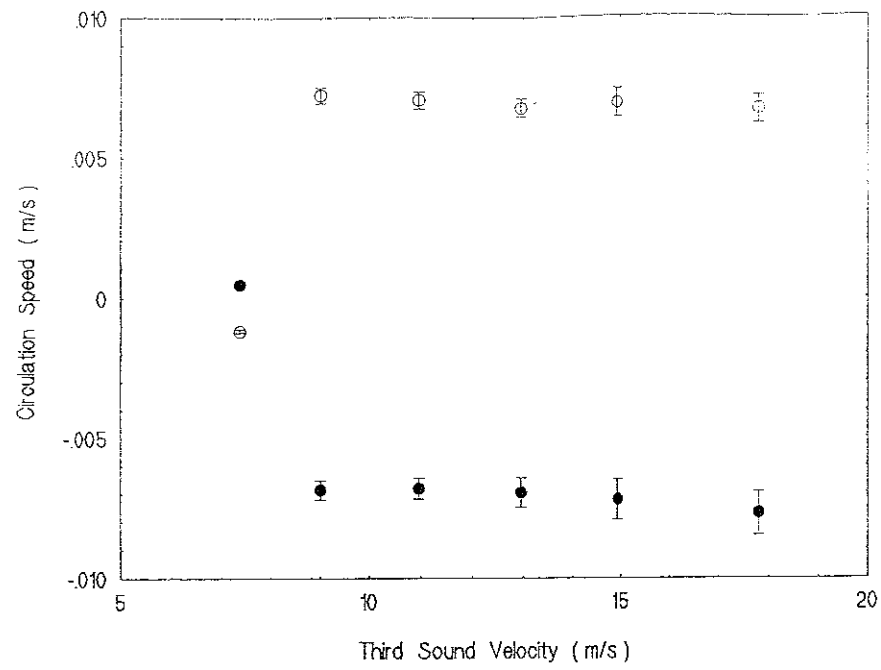


Fig. 6.6 A measurement of circulation vs changes of film thickness for (3,1) mode.

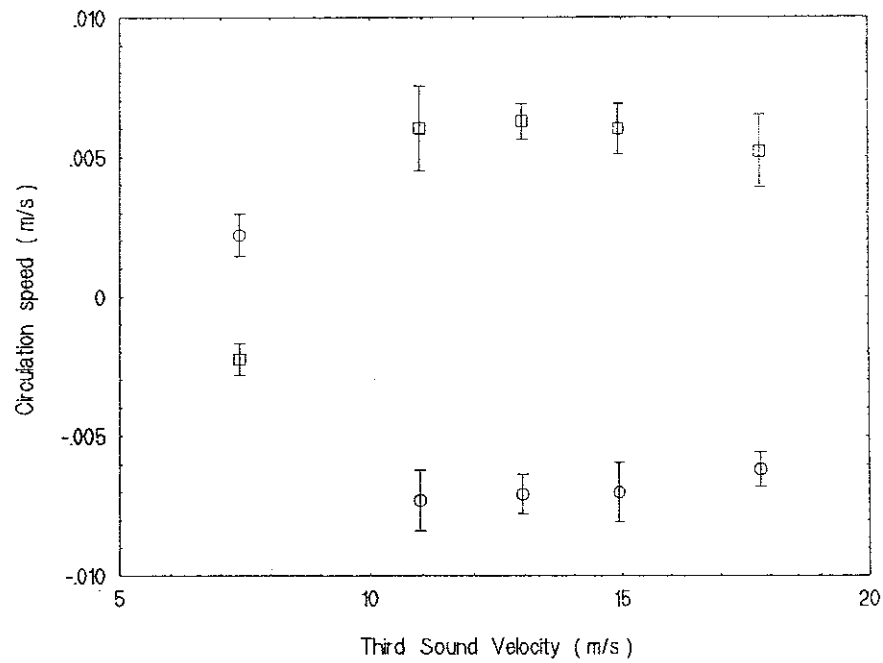


Fig. 6.7 A measurement of circulation vs changes of film thickness for (5,1) mode.

circulation does not change. But if we increase the film thickness rapidly, the circulation will change. Fig. 6.6 and Fig. 6.7 show that the circulation speed has a big jump at a third sound velocity of 7 m/s. This is because we added a large amount of helium gas into the resonator under high pressure, producing a circulation change. This is consistent with the analysis of trapping persistent currents in the cell. Circulations in a cell are usually generated by rotating a cryostat while cooling through the λ point of helium. Since we do not have such a device, the only way to get a circulation is to trap it by some kind of turbulence. How close the filling line is to the center hole of the cell seems to play an important role in this method. Experiments using the same cell as before, but with the filling line far away from the center hole, never showed a circulation. But after we made this change, we could easily see the circulation and we could even change it by different filling rates or different cooling rates through the critical temperature. The mechanism of this dramatic change is obvious, that more turbulence is brought into the cell which, therefore, introduced a circulation. Similarly, it is not surprising that the circulation does not change when helium is slowly added to the cell.

The results of this experiment provided us with an explanation of the contribution of the geometrical asymmetry splitting. The geometrical splitting changed in a random way during the process of increasing film thickness. This indicates that the cell's asymmetry is not the only cause of geometrical splitting. Dust sitting on the surface of the cell may also be an important factor in geometrical splitting. As the film thickness increases, the importance of capillarity on different dust sits will change. This will make a thickness dependent change in geometrical splitting. Another possible explanation is because the circulation in our cell may not be completely concentrated in the center. A non uniform distribution of pinned vortices may also cause a geometrical shift. Fig. 6.8 shows a geometric asymmetry

splitting versus third sound velocity. It clearly shows that the geometric asymmetry splittings are changing with film thickness.

6.2.2 Same γ for higher order third sound modes.

In the prior section, we showed the circulation speed versus third sound velocity for all three modes. If the results are examined carefully, it seems that the circulations are independent of third sound modes, since the results are all the same at certain film thicknesses. If the circulation is plotted versus all modes, you should get a straight line, according to our

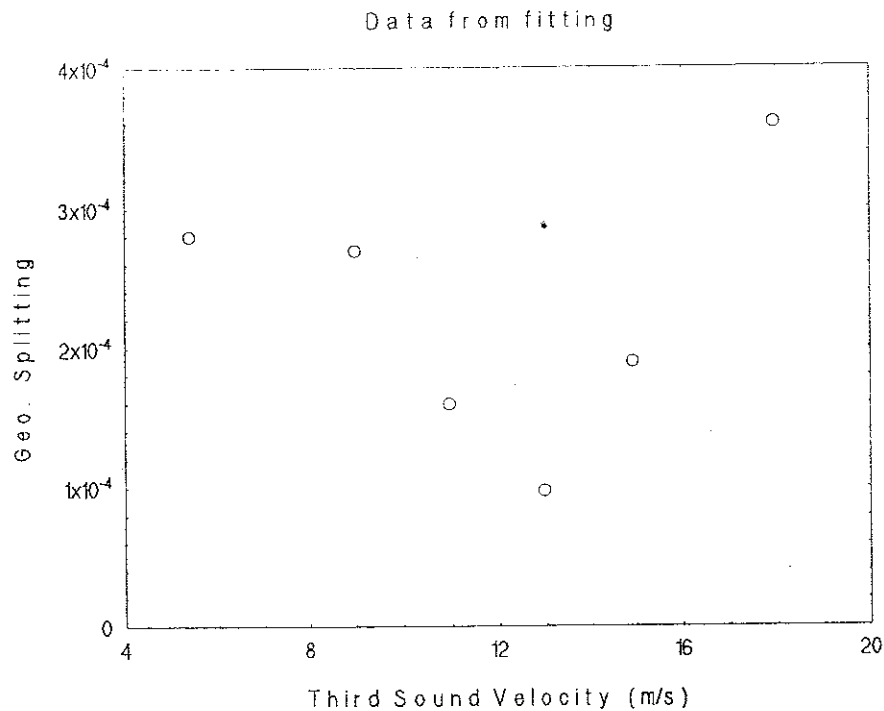


Fig.6.8 A measurement of geometrical asymmetry splitting versus changing of film thickness.

definition in Chapter 3 , which is

$$\gamma = \gamma_{nm} \frac{v(a)}{C_3} \quad (3.20)$$

but

$$C_3 = \frac{\omega}{k} = \frac{4 \pi f_D a}{X_{nm}} \quad (6.2)$$

so

$$\gamma = \frac{\gamma_{nm} v(a)}{4 \pi f_D a} X_{nm} \quad (6.3)$$

Obviously, if you plot γ versus X_{nm} , the slope will give the circulation speed $v(a)$ and the line will go across origin. The data shows that the lines are not exactly pass through the origin for either the calculation of amplitude or the fitting parameters. This reminds us that some solid body rotation may be involved in this case. The solid body rotation can be thought as uniformly distributed vortices rotating around center of the cell. The total circulation which was measured has two components, one is from circulation concentration at the origin, which means that most of the vortices are distributed in the center, and the other is solid body rotation. Therefore, if we model the total circulation with the two components described above, the total frequency shift due to the circulation is

$$\frac{\Delta \omega}{\omega} = \gamma = \gamma_{nm} \frac{v(a)}{C_3} + \gamma_u \frac{\omega_u}{\omega} \quad (6.4)$$

where ω_u is the solid body rotation frequency. Here γ_u is a constant which can be thought as the weighing of frequency shift due to solid body rotation

within each mode. The constant γ_u can be calculated from assuming that the flow field of the solid body rotation is

$$v(r) = \omega_u r \quad (6.4a)$$

The calculation of γ_u is given in Appendix D. Here we only show the result, which is

$$\gamma_u = \left[1 - \frac{2}{X_{nm}^2 - m^2} \right] m \quad (6.4b)$$

Rewriting equation (6.4) to a convenient form,

$$\frac{\Delta \omega}{\gamma_u} = \frac{\gamma_{nm} X_{nm}}{\gamma_u} \omega_c + \omega_u \quad (6.5)$$

where $\frac{v(a)}{a} = \omega_c$ is the frequency shift at the perimeter due to the center contribution of vortices. Therefore, the total number of vortices at center contribution can be written as

$$n_c = \frac{m_4 a^2}{\hbar} \omega_c \quad (6.6)$$

Next, let us find out how many vortices there are in uniform distribution. According to the definition:

$$\oint \vec{v}(r) \cdot d\vec{l} = \frac{n h}{m_4} \quad (6.7)$$

It is easy to get

$$\omega_u = \frac{v(r)}{r} = \frac{n_u \hbar}{m_4 a^2} \quad (6.8)$$

Here n_u is the total number of vortices in the uniform distribution. From (6.8) we have

$$n_u = \frac{m_4 a^2}{\hbar} \omega_u \quad (6.9)$$

Once we plot $\frac{\Delta \omega}{\gamma_u}$ versus $\frac{\gamma_{nm} X_{nm}}{\gamma_u}$ according to equation (6.5), we can easily determine ω_c and ω_u from the slope and intercept.

Fig. 6.9 and Fig. 6.10 are plots from amplitude calculation and fitting parameters respectively. Both results show that most vortices are concentrated in the center of the cell. The plot from the amplitude calculation shows fewer vortices in the uniform distribution, while the plot from the fitting parameters shows that about one half of the vortices are in the uniform distribution. We tend to believe the data from the fitting parameters because more information from the actual data is used, not only the amplitude but also the phase and all four resonances.

6.2.3 Some γ for both plus and minus modes.

Fig. 6.5, Fig. 6.6 and Fig. 6.7 in section 6.2.1 show measurements of circulation speeds at different film thickness for (1,1), (3,1) and (5,1) modes respectively. They also show that the circulation is the same for both plus and minus modes. Even when the total circulation made a big jump in

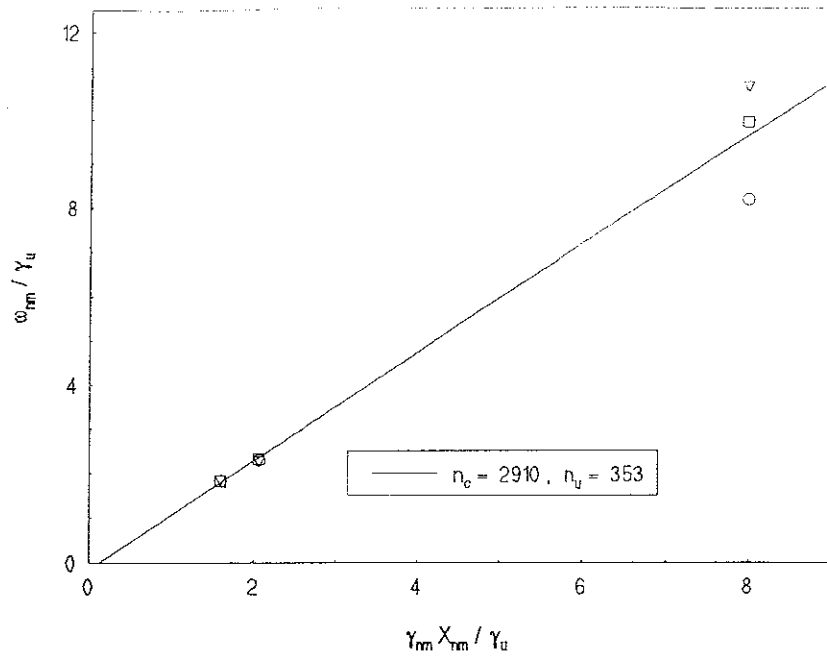


Fig. 6.9 A plot of equation (6.5) from the amplitude calculation and intercept . The negative intercept here means that the direction of solid body rotation is opposite the direction of the circulation. We can estimate the distribution of vortices.

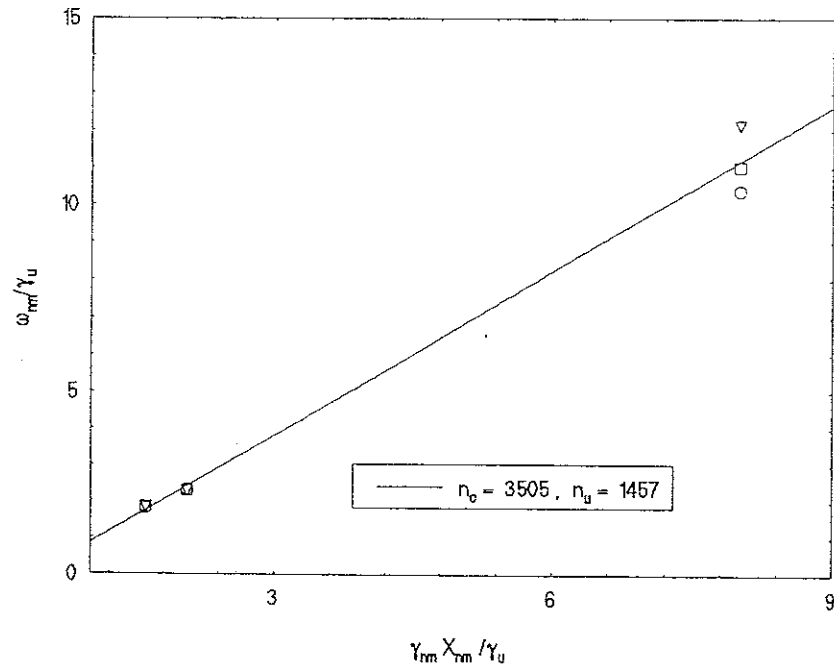


Fig. 6.10 A plot of equation (6.5) from the fitting parameters.

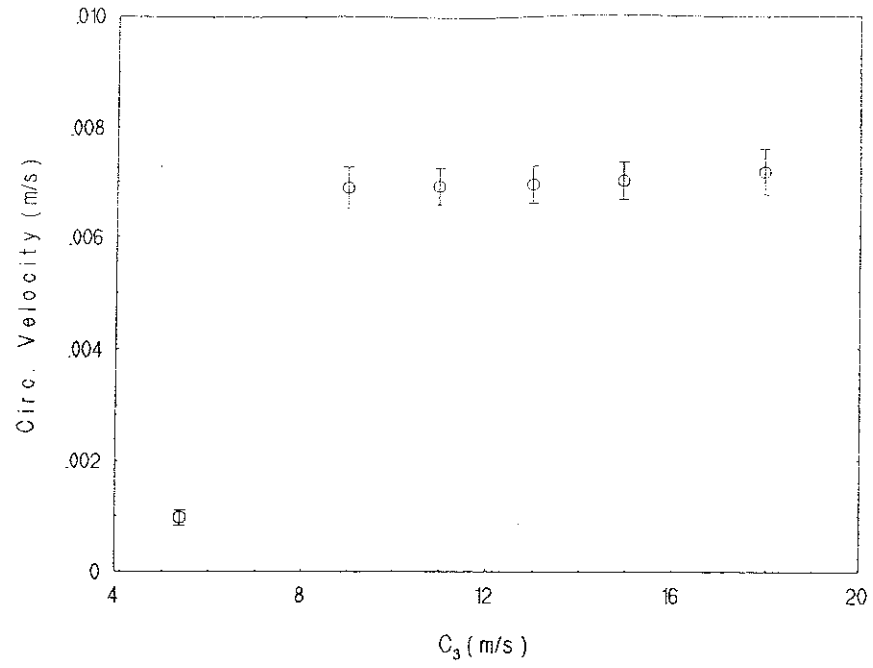


Fig. 6.11 A plot of theoretical fit results of circulation vs film thickness for (3, 1) mode.

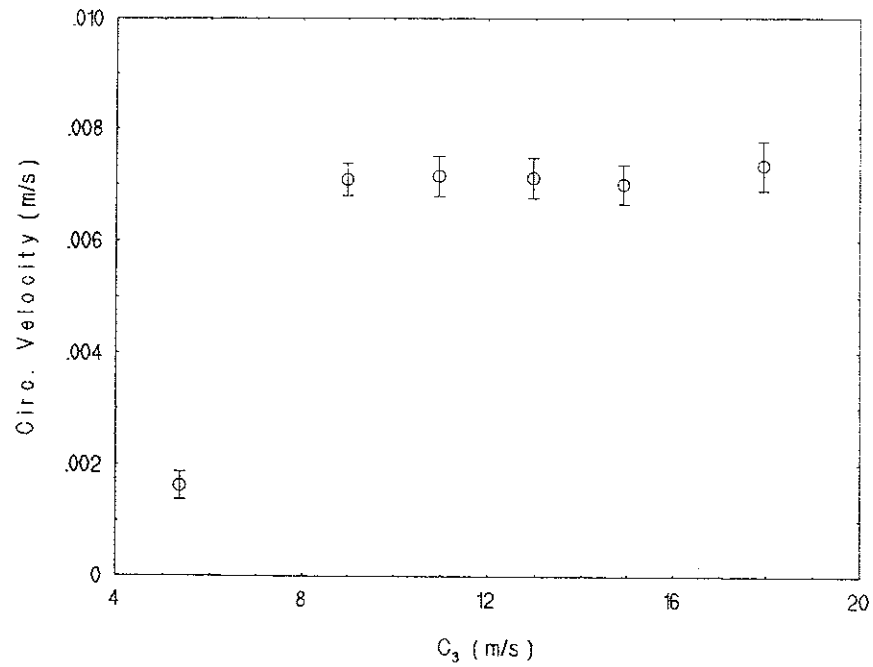


Fig. 6.12 A plot of theoretical fit results of circulation vs film thickness for (5, 1) mode.

Fig 6.6 and Fig. 6.7, measurements of circulation from plus and minus modes were still the same. The plus and minus sign in the figures only indicate the directions of the circulation relative to the drive, this is predicted in equation (4.62) of chapter 4. Fig. 6.11 and Fig. 6.12 are from the magnitude fitting results, as we discussed in the beginning of section 6.2 . There is only one curve in Fig. 6.11 and fig. 6.12 because we had already averaged the plus and minus modes when we analyzed the data. Comparing the two groups of figures, the results are consistent with the rotational drive technique.

6.2.4 No Amplitude Difference in (2,1) Mode.

In chapter 4 , we calculated the amplitude for all the modes and concluded that the amplitude of (2,1) mode is the same for either right or left drive. Fig. 6.13 shows experimental results of (2,1) plus and minus modes with two different drive situations. The upper branch is for plus mode with right and left drive and the lower branch is for minus mode. The amplitude which we measured for both driven situations had almost no difference. Although we made only three measurements at different third sound velocities, it clearly showed that the result of the calculations in chapter 4 are correct.

6.3 The Change of Circulations.

After the successful observation of circulations, we started to think about some ways to control the size of the circulation. As we pointed out before, our experimental device is not a rotating cryostat which is usually used to generate circulation. So generating or controlling a circulation was more difficult for us. Following the basic idea of generating these

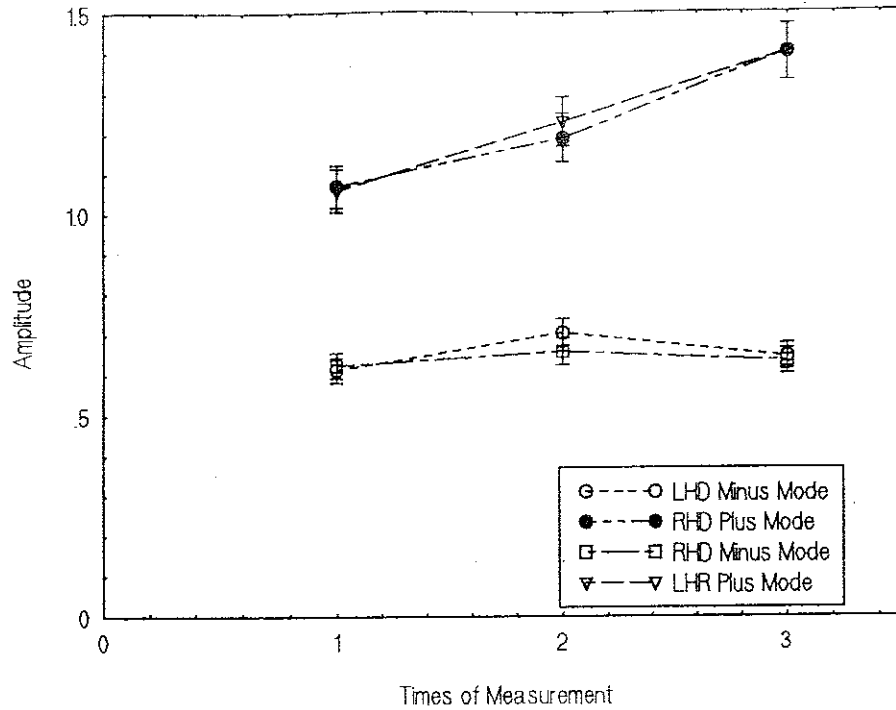


Fig. 6.13 A measurement of amplitude of $(2,1)$ mode with rotational drive technique. They show no differences in amplitude with right and left drives.

circulations, i.e. the amount of the circulation must be proportional to how much turbulence there is before you cool below the superfluid transition temperature. In another words, it is proportional to how many vortices are generated and enter into the cell. Based on this principle, we tried three methods to generate and control the circulation. Two of them worked pretty well, as we expected.

6.3.1 Changing Filling Rates.

This is a direct confirmation that the trapped circulation is proportional to the external turbulence. Remember the filling line is positioned just outside of the center hole of the cell, Different filling rates will give different turbulence. It usually gives a big circulation in the resonator when we fill the sample with a big filling pressure. We have also compared the experimental results with the filling line away from the center hole. This clearly makes a big difference in the resulting circulation speed. Although we have not measured the details of the relationship between the filling pressure and circulation speed, qualitatively speaking, they are proportional to each other.

6.3.2 Changing Cooling Rates.

This is the way to change circulation without changing film thickness. The procedure we followed was to warm up the cell above the superfluid transition temperature, then, cool it back down at different cooling rates. The mechanism of circulation changes can be described in the following manner: As the temperature warms to above the superfluid transition temperature, the primary circulation in the cell is eliminated due to the viscosity of normal fluid, Excitations in the film will be generated and more turbulence will be created, since the equilibrium between the film inside the cell and the outside of the helium reservoir is destroyed. This process can also be understood by the creation of more vortices in the cell which generate a rotational field inside the cell. As the cell is cooled, the vortices will look for reunion with their antipairs. How many pairs of vortices will get reunited is dependent on how fast the whole system is cooled through the transition temperature. Once it goes through this temperature, the circulation will stay at a constant rate, since the fluid now is superfluid. Based on this analysis, measurements of circulations before we warmed up and after we cooled back

down, along with their cooling rates were taken.

Fig. 6.14 and Fig. 6.15 show the total mode splitting versus the cooling rate at the third sound velocities 10.45 m/s and 12.62 m/s respectively. Each point in these figures corresponds to one warm up and cool down process. Although Fig. 6.14 and Fig. 6.15 correspond to different third sound velocities and hence different film thickness, they all show that the total mode shift tends to increase for larger cooling rates. The total splitting is the combination of geometric shift and circulation shift. The geometric shift should not change during the warm up and cool down process since the film thickness remains the same. Only thing that could change is the circulation state. Fig. 6.16 shows a measurement of geometric splitting versus cooling rate. Although this is somewhat noisy, it does show that the geometric asymmetry shift changes only with film thickness changes, no matter how fast the cooling rate is. In comparison with these results, Fig. 6.17 shows the circulation changes with the cooling rate. In conclusion, we have found a way to change our circulation state by controlling the cooling rate. A rough relationship between circulation and cooling rate has been set up and plotted out for further reference.

Another feature observed was a change in the direction of the direction change of the circulation. Fig. 6.18 shows a split mode which changed its direction of circulation after the warm up and cool down procedure. The amplitude of the mode switched over indicating a direction change. From the calculation this represents a sign change between the plus mode and minus mode.

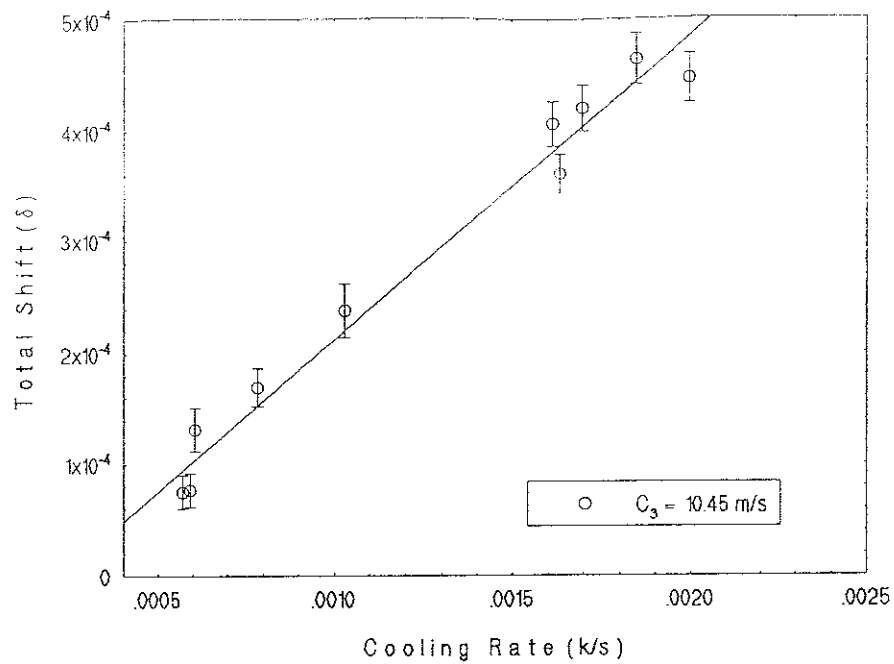


Fig. 6.14 A measurement of total splitting vs cooling rate at the third sound velocity 10.45 m/s .

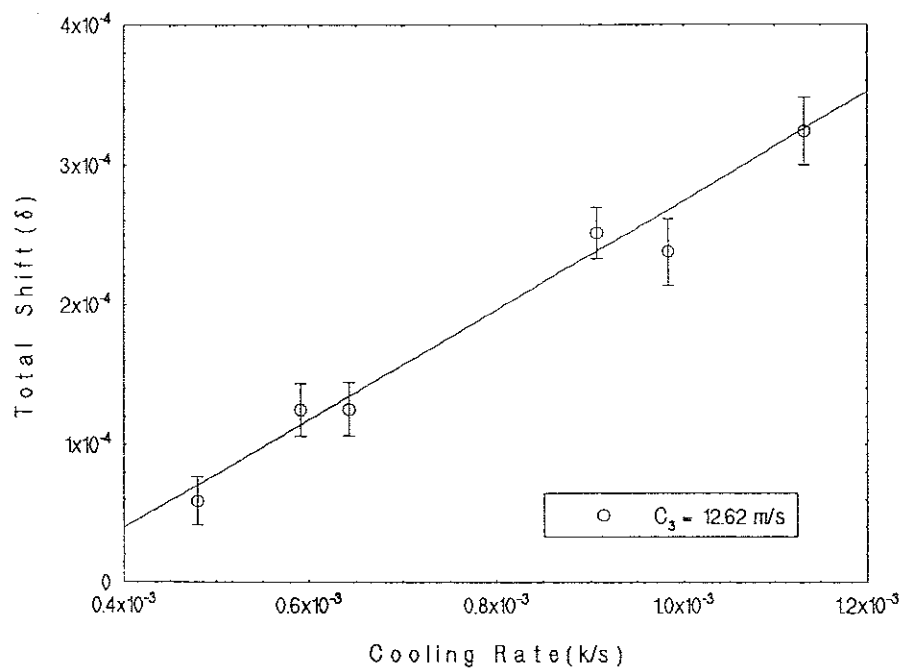


Fig. 6.15 A measurement of total splitting vs cooling rate at the third sound velocity 12.62 m/s .

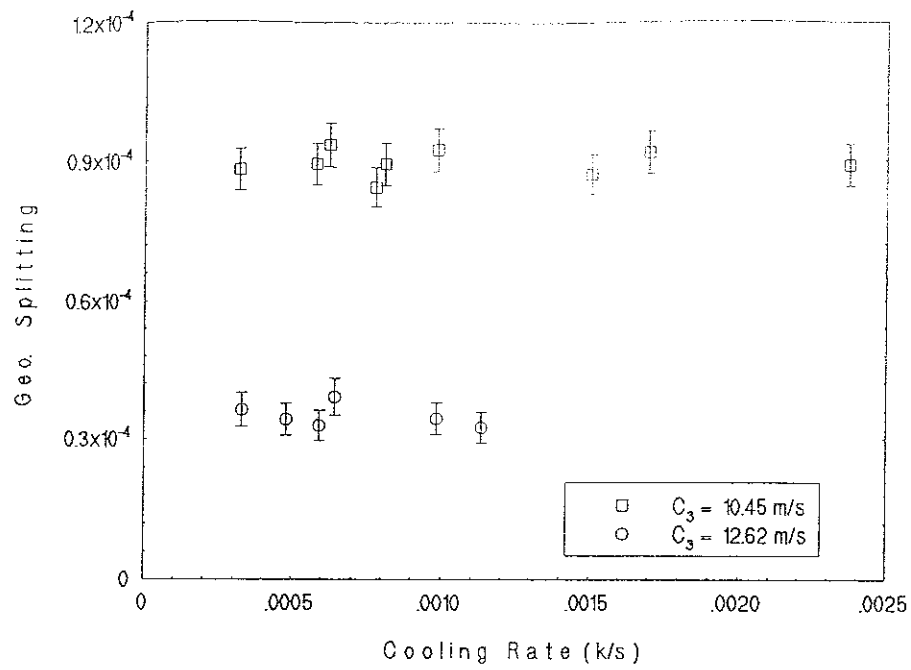


Fig. 6.16 A plot of geometrical splitting vs cooling rate at two different film thickness. It seems stay a level at different cooling rates.

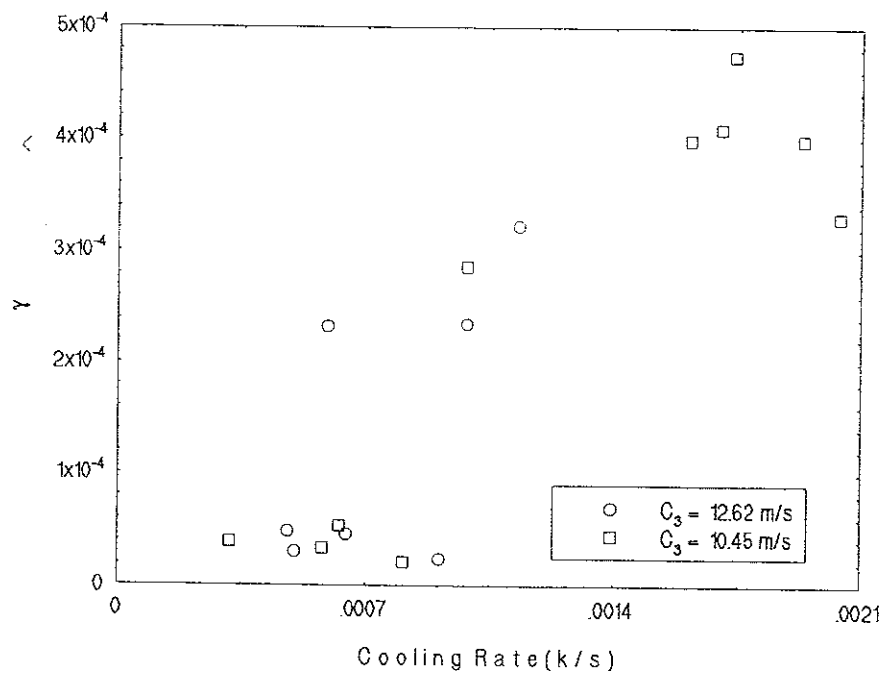


Fig. 6.17 A plot of circulation vs different cooling rates.

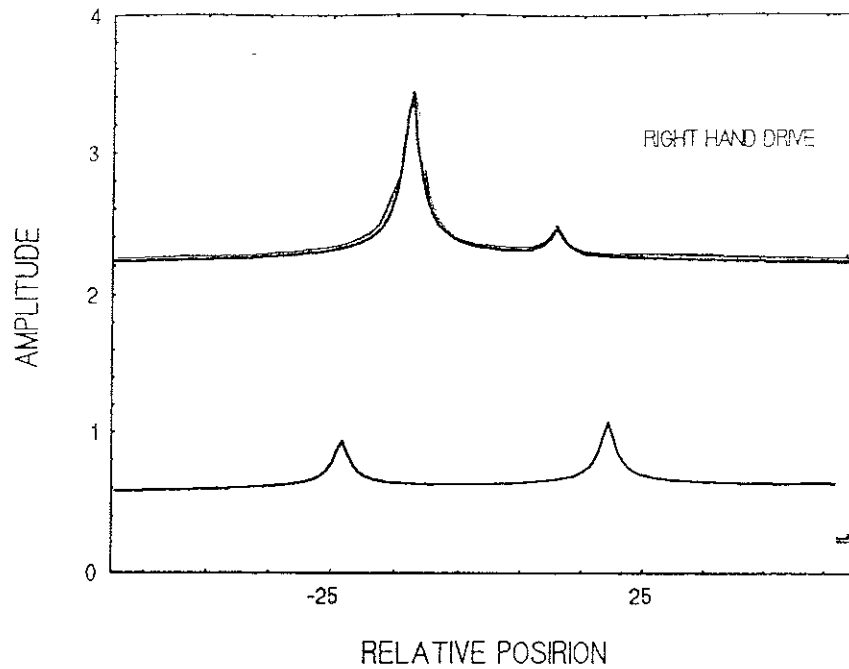


Fig. 6.18 Shows that the direction of circulation changes after a warm up and cool down procedure.

6.3.3 Circulation not Changed by Vary of Drive Voltage.

The third method tried to change the circulation state through a large drive voltage or an external disturbance. We drove the third sound resonance with a much larger drive voltage than usual. No changes in circulation state were observed. This may imply that the drive voltage is still not high enough (we only gave 10 V peak to peak). We did not want to short out our resonator, so we did not pump enough energy into the cell to change the state of circulation. But in any case, there should be a way to change the circulations inside a cell if the amplitude can be made high enough. Also, no changes were observed after banging on the cryostat. However, which some other group did see a change in circulation in bulk helium after hitting their cryostat.

6.4 Quantization

In the beginning of this chapter, we have talked about other groups that had observed single quanta in bulk liquid helium, but no one has observed them in the helium films. We tried to reach this goal in this work but unfortunately we were not successful. The lowest circulation velocity we have seen so far is beyond 10^{-5} m/s. This corresponds to the quanta number around 61. The reasons we could not see a single quanta at this time are :

- 1). We must get rid of geometric asymmetry shift or at least decrease it by about a factor of 10 in order to detect single quanta, since the total mode splitting is dominated by geometric splitting at small circulation speed. To reach this goal, one way is to try to " tune " away the geometric asymmetry splitting. This is possible, some work has been done in this laboratory. For details of work, see reference [6.3]. The other way is to get lucky, since the different resonators can have different geometric asymmetry splittings.

- 2). We can make a smaller cell. This is a difficult thing to do, from the calculation, the number of quanta is proportional to the size of the cell and the velocity of the film flow. Therefore, decreasing the diameter of the cell will definitely help this.

- 3). We must increase the sensitivity of the experimental system in order to detect such small circulation. The rotational drive technique may not work in this case because resonances overlap too much so the difference between two split modes can not be detected.

One other technique we can use to detect a small circulation is the measurement of mode decay after we drive up the resonance. Since we drive two split modes at the same time, when we remove drive, both modes will decay simultaneously, but the decay frequencies will jump over two modes. Fig. 6.19 shows two decays at different time scales. From the beat of the decay,

we can easily measure the frequency difference for both modes, and therefore, we can measure the total mode splitting. Then we need to measure the amplitude of the resonance for one bigger mode (either plus or minus mode). From that we can find out the circulations. According to this, if a geometric asymmetry splitting was 10 times smaller than what we have now, we could see the single quanta. The way to identify a single quanta is to detect at least one beat during the third sound decay. The decay time for the third sound is

$$\tau_{decay} = \frac{2Q}{\omega} \quad (6.10)$$

while the characteristic time for one beat is

$$\tau_{Beat} = \frac{1}{\Delta \omega} \quad (6.11)$$

The observation condition is

$$\tau_{Beat} = \tau_{Decay} \quad (6.12)$$

this will require

$$Q \geq \frac{1}{2} \frac{C_3}{v(a)} \quad (6.13)$$

So suppose we can have circulation speeds up to 5×10^{-6} , which is less than 10 times smaller than the geometric asymmetry splitting at the third sound velocity around 10 m/s, then the Q's we need are about one million. However, we have already had such value of Q's at the third sound

velocity 10.4 m/s , but the geometric asymmetry splitting is at 10^{-5} scale. Therefore, we do need to eliminate the geometric asymmetry splitting.

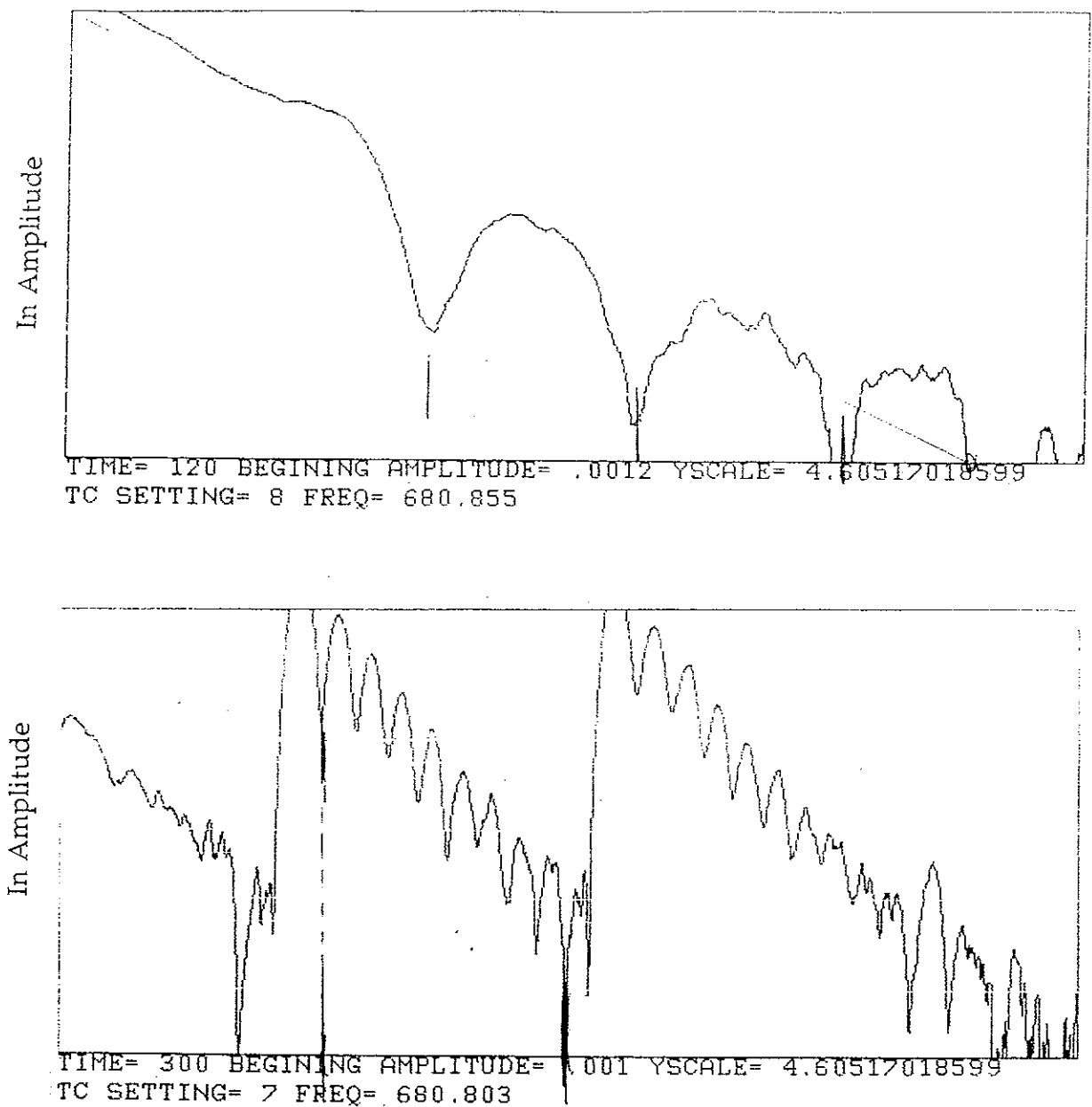


Fig. 6.19 Shows two decays of the third sound resonance. The beat is due to the overlapping of two split mode. The total splitting can be determined from the beat frequency.

SUMMARY

In summary, we have developed the rotational drive technique in both theory and experiment. The data has shown that the calculations are consistent with the experimental results. We also have made for the first time, measurements of circulation in a third sound resonator. The observation of circulation changes during the procedure of warm up and cool down provided a rough method to control the circulations inside third sound cell. The investigation of geometric asymmetry splitting in the third sound cell is very helpful for the further study of the helium film in the resonator. If the geometric asymmetry splitting can be removed, observation of single quanta in the two dimensional film becomes possible.

Appendix A

Modes Configuration of Third Sound Resonator

Third sound is a surface wave, it must obey some wave equations. To figure out how its modes are configured, our first task is to derive the wave equations which satisfies the third sound velocity. Recall equations in chapter 2,

$$\rho \frac{\partial h}{\partial t} + (\rho_s) d \frac{\partial v_{sx}}{\partial x} = 0 \quad (2.16)$$

$$\frac{S}{d} \frac{\partial h}{\partial t} + \frac{C}{T} \frac{\partial T}{\partial t} = 0 \quad (2.20)$$

$$\frac{\partial v_{sx}}{\partial t} = -f \frac{\partial h}{\partial x} + S \frac{\partial T}{\partial x} \quad (2.23)$$

Taking derivative on both sides of (2.23) respected to x,

$$\frac{\partial^2 v_{sx}}{\partial t \partial x} = -f \frac{\partial^2 h}{\partial x^2} + S \frac{\partial^2 T}{\partial x^2} \quad (A-1)$$

the time derivative of equation (2.16) is

$$\rho \frac{\partial^2 h}{\partial t^2} + (\rho_s) d \frac{\partial^2 v_{sx}}{\partial x \partial t} = 0 \quad (A-2)$$

Combined equations (A-1) and (A-2) yield,

$$\frac{\partial^2 h}{\partial t^2} = -\frac{\langle \rho_s \rangle}{\rho} d \left[-f \frac{\partial^2 h}{\partial x^2} + S \frac{\partial^2 T}{\partial x^2} \right] \quad (\text{A-3})$$

It is easy to rewrite equation (2.20) like:

$$\frac{S}{d} \frac{\partial h}{\partial x} = -\frac{C}{T} \frac{\partial T}{\partial x} \quad (\text{A-4})$$

Taking a derivative respected to x on both sides of equation (A-4)

$$\frac{S}{d} \frac{\partial^2 h}{\partial x^2} = -\frac{C}{T} \frac{\partial^2 T}{\partial x^2} \quad (\text{A-5})$$

Substituted (A-5) into (A-3) one has

$$\frac{\partial^2 h}{\partial t^2} = \frac{\langle \rho_s \rangle}{\rho} \left[f d + \frac{TS^2}{C} \right] \frac{\partial^2 h}{\partial x^2} \quad (\text{A-6})$$

Rewrite this ,

$$\frac{\partial^2 h}{\partial x^2} - \frac{1}{\frac{\langle \rho_s \rangle}{\rho} \left[f d + \frac{TS^2}{C} \right]} \frac{\partial^2 h}{\partial t^2} = 0 \quad (\text{A-7})$$

For three dimensional case, one can change (A-7) to :

$$\left[\nabla^2 - \frac{1}{C_3} \frac{\partial^2}{\partial t^2} \right] h = 0 \quad (\text{A-8})$$

The solution of equation (A-8) can be found in any mathematical physics books,

$$h(r, \phi) = \sum_m h_m J_m(kr) e^{i m \phi} \quad (\text{A-9})$$

we can add the time dependent part as

$$h(r, \phi, t) = \sum_m h_m J_m(kr) e^{i m \phi} e^{-i \omega t} \quad (\text{A-10})$$

where $J_m(kr)$ is the m th Bessel function of the first kind. $m=0, \pm 1, \pm 2, \pm 3, \dots$ the azimuthal quantum number. One important point we have to make explicit here is that the solution (A-10) has assumed that the wave functions are finite at the origin, this implies that Bessel functions of the second kind, $Y_m(x)$ are not allowed. This is not precisely the case since we have a hole in the center of the cell, but since it is small, so Y_m can be neglected. The presence of the hole also eliminates any J_0 modes.

The boundary conditions that link the solutions of the top plate to the bottom plate are (see figure A1) [A.1]

$$h_{\text{Bottom}}(r, \phi) \Big|_{r=a} = h_{\text{Top}}(r, \phi) \Big|_{r=a} \quad (\text{A-11})$$

$$\frac{\partial}{\partial r} h_{\text{Bottom}}(r, \phi) \Big|_{r=a} = - \frac{\partial}{\partial r'} h_{\text{Top}}(r', \phi) \Big|_{r'=a} \quad (\text{A-12})$$

Equation (A-11) requires that the surface be continuous across the corner in the third sound resonator. Equation (A-12) requires a smooth surface across the corner. So the plates must have some angular dependence in order to satisfy the continuous and smooth requirements of equations (A-11) and (A-12). The boundary conditions lead to two possible type of modes : node modes and antinode modes.

In node modes the amplitude is zero at the edge of the cavity. Equation

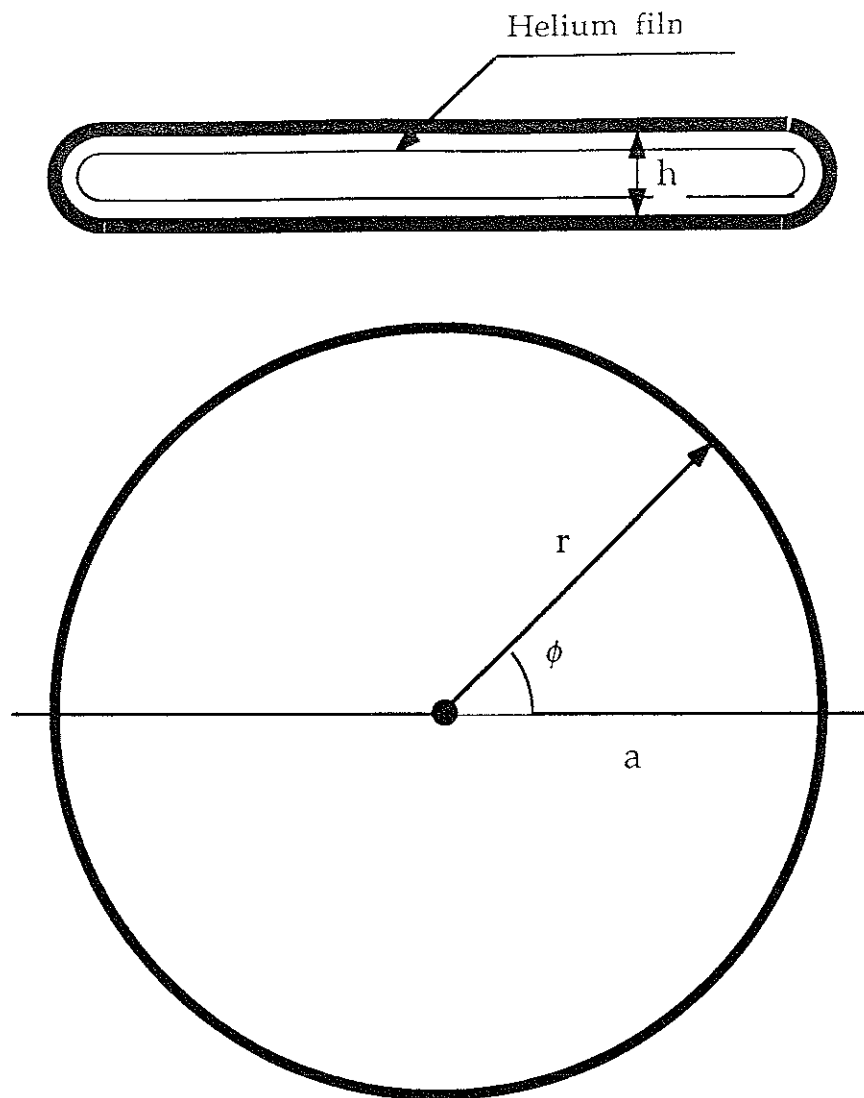


Fig. A - 1. Basic geometry of a pancake shaped cell used to calculate mode configuration of a TSR.

(A-12) requires the top plate to be 180 degrees out of phase with the bottom plate. These modes have resonant frequencies given by the zero crossings of the Bessel function.

$$\omega_{nm} = \frac{C_3 W_{nm}}{a} \quad (A-13)$$

where m is the angular number, W_{nm} is the n th zero of the m th Bessel function $J_m(x)$.

In antinode modes the amplitude of the wave is a local maximum at the edge of the cell. The resonant frequencies of these modes are

$$\omega_{nm} = \frac{C_3 X_{nm}}{a} \quad (A-14)$$

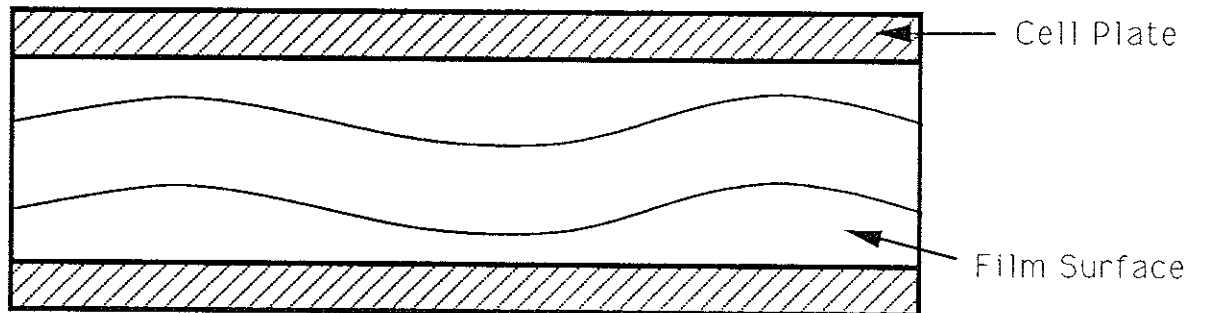


Fig. A - 2. The node mode. It has a 180 degrees phase difference between top and bottom plates. This is not a detectable mode.

where X_{nm} is the n th zero of the derivative of the m th Bessel function (i.e. $J'_m(X_{nm})=0$). In those modes the top and bottom surfaces resonant in phase with one another.

The capacitive detector can not detect the node modes because of the 180 degrees phase difference between each plate. (see Fig. A-2 for details of the film surface). The antinode modes, however, are in phase on the top and bottom plates; the surface of the film illustrated in Fig. A-3.

The third sound resonator is designed to detect the first few antinode modes. A listing of the first few resonator modes are shown in table A-1. The cell that we were used in the experiment has a very good sensitivity and has already detected $n=1, m=1, 2, 3, 5, 6, 7, 9, 10, 11$ and $n=2, m=1$ modes so far.

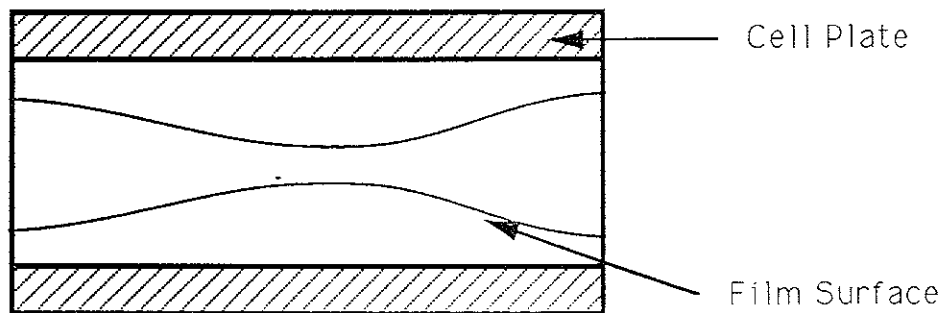


Fig. A - 3 . The antinode mode. The films on the top and bottom plates are in phase. This is a detectable mode.

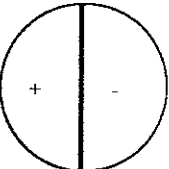
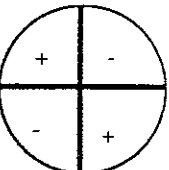
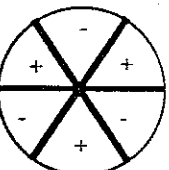
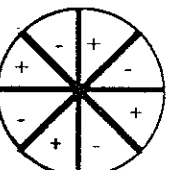
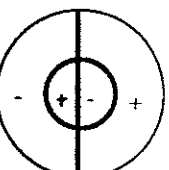
MODE (m,n)	Xnm	RELATIVE AMPLITUDE	NODE LINES	COMMENTS
(1,1)	1.84118	2.02E+01		First mode Detectable.
(2,1)	3.05424	1.32E+01		Detectable, but rotational drive has no effect.
(3,1)	4.20119	5.32E+00		Detectable, but it start to reduce capacitor's sensitivity.
(4,1)	5.31755	0		The opposite polarities reduce a lot the capacitor's sensitivity
(1,2)	5.33144	2.39E+00		Same reason as above, but still detectable.

Table A - 1 Modes of third sound resonator.

Appendix B

Making a Third Sound Resonator

Building a third sound resonator is the crucial part of this experiment. Basically, we want the gap between two capacitor plates to be as small as possible and still be able to have a 10 V peak to peak drive voltage that does not short out. The surface of the cell has to be as smooth as possible either on the primary glass surface or after evaporation. The hole in the center of the resonator should be small but this is limited by the technique we used. The time that the cell sets in the air should be as short as possible in order to decrease oxidation. Following is the step by step process of making a third sound cell.

B1. Choosing Material.

The glass used was micro slides, 1 mm thick. Cutting it into two sizes, one 16×16 mm and other 21×21 mm. After cutting, you have to look at it carefully under the microscope. No cracks, scratches and defects were allowed on the surface. As these will definitely increase the dissipation in the film. Try to get a "perfect glass piece".

B2. Drilling a Hole.

The hole was drilled mechanically. The tricky part of this technique is to make a drill. We used two sizes Cu Ni tubes, one outside dimension exactly fit into the other inside dimension. Soldering the joint allowed for

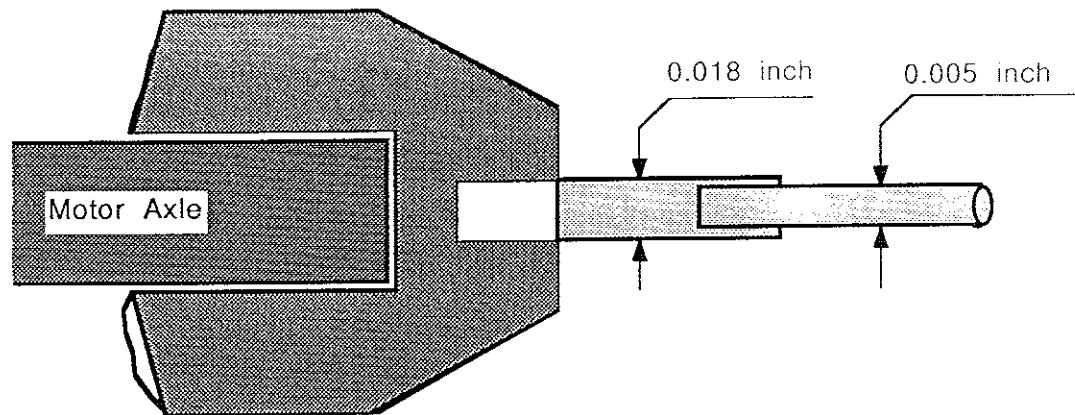


Fig. B - 1. Schematic drawing of a home made driller used to drill small hole on the third sound cell.

easy changing of the "bit". The small end was our drill and other end soldered to a holder. Figure B - 1 illustrate this device. The small tube is used to grind through the glass with the help of a fine abrasive and water.

B3. Etching Circle on the Small Piece.

- 1). Clean up the glass surface, using an Alconox detergent wash first, then a distilled water rinse. Then, dropping into 50 % NH_4OH for a few second, and rinse again. Finally, rinse in methanol as a final cleaning step.

- 2). Set glass flat on a surface spinning at about 3600 RPM. Wipe the surface again using methanol to make sure nothing was setting on the surface.

- 3). With the spinner off, apply several drop of shipley S1400-31 photo

resist and then start to spin about 5 to 10 seconds. This will guarantee that the covered film was uniform and the right thickness.

4). Bake in an oven for 20 to 30 minutes at temperature about 95 to 105 Centigrade so that the photo resist will get harder.

5). Expose 15 minutes at about 20 cm away from the Hg-Arc lamp with a circular masked film on. We only allowed a circular ring to get exposed.

6). Develop in 5 % NaOH for 20 to 30 second. This removes the photoresist in the exposed region.

7). Rinse in distilled water and blow dry with air. Look again under the microscope to make sure the photo resist was removed completely from the exposed area.

8). Etch 10 to 15 second in pure hydrofluoric acid, again rinsing immediately. in water. This etches the glass forming the etch pit.

9). Check under microscope to make sure the etched circle is good, no bridge crossing over. This is very important in preventing the glue from crossing during the gluing process.

B4. Evaporating Process.

1). Cut a bevel in one side of the etched piece. Then polished the beveled surface by sand paper. The reason for this is that we want to deposit gold on the bevel surface in order to make a solder joint between two plates.

2). Clean up the surface again by methanol in order to make good deposition.

3). Mask both pieces with thin wires formed in the correct shape of the electrodes.

4). Evaporate with a thickness monitor. In this work, getting 1000 angstrom thick film corresponded to 4 KHz change of the crystal oscillator

monitor.

B5. Gluing Process.

1). Place the two plates together face by face and put four $10\ \mu\text{m}$ plastic stripes on each side. Line up the center hole by sending light through from the bottom. Then carefully put a weight about 44 grams on the top to minimize the gap. Check to see there is no short between the plates after it has set. This time glue only four points at the corners with stylast 2850 GT epoxy.

2). Check again to see there is no short between the plates again when it dry. Measure capacitance, calculate the gap to check that the gap is uniform or not.

3). The second application of glue is a very important process. We have to watch it under microscope while the glue is sucked in around all edges through capillarity. The inside of the cell is pressurized about 800 torr through the hole in order to stop glue from winking across the etched circle. By adjusting pressure that we apply, one can control the glue and let it stop at the etched circle.

4). After the glue is completely dry, check the capacitance again to make sure that the glue was not sucked into the cell.

B6. Treatment About the Outside of the Cell.

In order to let cell have good thermal contact with the refrigerator, a thick silver film was deposited on both of the outsides of the cell. This silver made direct contact with the refrigerator as described in chapter 5.

Appendix C

Calculation of the Response of the TSR to a Drive

Our pancake shape third sound resonator can be treated as three capacitors in series, as shown in Fig. C-1, the bottom and top plates are covered with helium film which has height h . The cell can be thought of as two capacitors filled with dielectric material with dielectric constant ϵ , and the vacuum in between just like another capacitor with dielectric constant ϵ_0 . The capacitance for any small area dA can be written as

$$\frac{1}{C} = \frac{1}{C_1} + \frac{2}{C_2} \quad (C-1)$$

with
$$C_1 = \frac{\epsilon_0 d A}{d - 2h} \quad C_2 = \frac{\epsilon d A}{h} \quad (C-2)$$

where C_1 is the part of the capacitance from the vacuum inside, and C_2 from the helium films. d is the gap of the resonator, h is the height of the helium films. The total capacitance over the pickup area is :

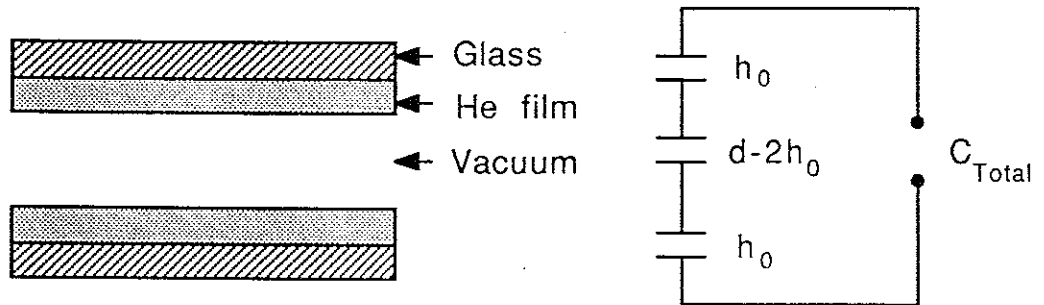


Fig. C - 1 Shown a resonator just like three capacitor in series.

$$C_{Total} = \int_{pickup} \frac{\epsilon_0 d A}{d - 2h \left(1 - \frac{\epsilon_0}{\epsilon} \right)} \quad (C-3)$$

As we described in Chapter 2, h can be written as :

$$h = h_0 + h_{nm} \psi_{nm}(r, \phi) \quad (2-28)$$

with h_0 the static film thickness, h_{nm} the changes from h_0 and

$$\psi_{nm}(r, \phi) = J_m(k_{nm} r) \cos m \phi$$

the wave function which described the third sound wave on the helium surface.

Using Taylor expansion and equations (2-28) , the equation (C-3) becomes

$$\begin{aligned} C_{Total} &= \frac{\epsilon_0 A}{d} \left[1 + \frac{2h_0}{d} \left(1 - \frac{\epsilon_0}{\epsilon} \right) \right] + \frac{2\epsilon_0 h_{nm} \left(1 - \frac{\epsilon_0}{\epsilon} \right)}{d^2} \int_{pickup} \psi_{nm} dA \\ &= C_0 + C_h + C_{nm} \end{aligned} \quad (C-4)$$

obviously, C_0 is the capacitance corresponding to empty cell (i.e. $h=0$) . C_h is the capacitance due to the static shift of the film. C_{nm} is the change in capacitance which response to a driven third sound resonance.

The integral in (C-4) can be normalized to the whole cell in order to simplify the calculations later on. So, we define :

$$\langle \psi_{nm} \rangle_{P,D} = \frac{\int_{P,D} \psi_{nm} dA}{\int_{cell} dA} \quad (C-5)$$

where P, D here represent pickup and drive. Therefore, one can write C_{nm} as

$$C_{nm} = \frac{\epsilon \pi a^2}{d} \frac{2 h_{nm}}{d} \left[1 - \frac{\epsilon_0}{\epsilon} \right] \langle \psi_{nm} \rangle_P \quad (C-6)$$

noticed here that C_{nm} is a function of the various modes since ψ_{nm} represent the Bessel function which are different for different modes.

Now, one can start to calculate h_{nm} . For a capacitor with applied electric field E , in the case of $\omega=0$, the force per unit mass applied to the helium film can be written as

$$f = \frac{1}{2} \frac{(\epsilon - \epsilon_0)}{\rho h'} \nabla(E^2) \quad (C-7)$$

where ρ is density of helium, h' is the height change of the film due to the electric field from the static film. Therefore,

$$h' = \frac{1}{2} \frac{(\epsilon - \epsilon_0)}{\rho f} \nabla(E^2) \quad (C-8)$$

We can also write the electrostatic energy as

$$E_{nm} = \int_{D_{drive}} \frac{1}{2} (\epsilon - \epsilon_0) E^2 h' dA \quad (C-9)$$

the electrostatic force will be balanced by van der Waals force when the films is in equilibrium. So, one can write Van der Waals energy as

$$E'_{nm} = \int \frac{1}{2} \rho f (h')^2 dA \quad (C-10)$$

with $h' = h_{nm} \psi_{nm}(r, \phi)$ and $E_{nm} = E'_{nm}$, we have (for $\omega = 0$)

$$h_{nm} = \frac{(\epsilon - \epsilon_0) E^2 \int_D \psi_{nm} dA}{\rho f \int_{cell} \psi_{nm}^2 dA} \quad (C-11)$$

For the case of $\omega \neq 0$ one can use the model of a mass on a spring, this leads:

$$h_{nm} = \frac{(\epsilon - \epsilon_0) E^2 \int_D \psi_{nm} dA}{\rho f \int_{cell} \psi_{nm}^2 dA} \frac{1}{1 - \left(\frac{\omega_0}{\omega}\right)^2 - \frac{i}{Q}} \quad (C-12)$$

But

$$\begin{aligned} \int_{cell} \psi_{nm}^2 dA &= \int_0^a J_m^2(k_{nm} r) r dr \int_0^{2\pi} d\phi \\ &= \int_0^1 J_m^2(X_{nm} r) a^2 r dr \int_0^{2\pi} d\phi \\ &= \pi a^2 \left(1 - \frac{m^2}{X_{nm}^2}\right) J_m^2(X_{nm}) \end{aligned} \quad (C-13)$$

the force acting on the film can be written as a function of third sound velocity and film thickness, i.e.

$$f = \frac{C_3^2}{\frac{\rho_s}{\rho} h} \quad (C-14)$$

If the drive voltage can be written as:

$$V_{drive} = V_D \cos \omega t$$

and then

$$E^2 = \frac{V_D^2}{d^2} \frac{1 + \cos 2\omega t}{2} = E_0^2 + \frac{1}{2} \frac{V_D^2}{d^2} \cos 2\omega t \quad (C-15)$$

so the square of the effective drive field will be

$$E_e = \frac{1}{2} \frac{V_D^2}{d^2} \quad (C-16)$$

substituting (C-5), (C-13), (C-14), and (C-16) into (C-6) one finally has

$$\frac{\Delta C}{C} = \frac{C_{nm}}{C} = \frac{\left(1 - \frac{\epsilon_0}{\epsilon}\right) \langle \psi_{nm} \rangle_P}{d} \frac{\frac{\rho_s}{\rho} (\epsilon - \epsilon_0) V_D^2 h \langle \psi_{nm} \rangle_D}{\rho d^2 C_3^2 \left(1 - \frac{m^2}{X_{nm}^2}\right) J_m^2(X_{nm})} \frac{1}{1 - \left(\frac{\omega_0}{\omega}\right)^2 - \frac{i}{Q}} \quad (C-17)$$

Appendix D

Calculation of Mode Splitting

The calculation that we present here is a summary of reference [D.1]. The calculation, however, gives the general results of a frequency splitting due to an arbitrary flow field in the disk shaped resonator. I have decided to present this result here since it gives a universal result for this kind of problem. I would like to thank Professor Ralph Baierlein here for his kind help.

Start again from our equations of motion in Chapter 4.

$$\frac{\partial \vec{v}'}{\partial t} = -g \nabla h' - \vec{\nabla} (\vec{v}_0 \cdot \vec{v}') \quad (3.17)$$

$$\frac{\partial h'}{\partial t} = -h_0 (\vec{\nabla} \cdot \vec{v}') - h' \vec{\nabla} \cdot \vec{v}_0 - \vec{v}_0 \cdot \nabla h' \quad (3.18)$$

If we define :

$$U \equiv \left\{ h', \left(\frac{h_0}{g} \right)^{\frac{1}{2}} \vec{v}' \right\} \equiv \{ u_0, \vec{u} \} \quad (D-1)$$

Here g is van der Waals force. The equation (3.17) and (3.18) with new variables are

$$\frac{\partial u_0}{\partial t} = -\sqrt{g h_0} \vec{\nabla} \cdot \vec{u} - \vec{\nabla} \cdot (\vec{v}_0 u_0) \quad (D-2)$$

$$\frac{\partial \vec{u}}{\partial t} = -\sqrt{gh_0} \nabla u_0 - \vec{v}_0 \cdot \nabla \vec{u} - \vec{u} \cdot \nabla \vec{v}_0 \quad (\text{D-3})$$

We can write these two equations in a 2×2 matrix form.

$$\begin{aligned} \frac{\partial}{\partial t} \begin{pmatrix} u_0 \\ \vec{u} \end{pmatrix} &= \begin{pmatrix} 0 & -\sqrt{gh_0} \vec{\nabla} \cdot \\ -\sqrt{gh_0} \nabla & 0 \end{pmatrix} \begin{pmatrix} u_0 \\ \vec{u} \end{pmatrix} + \begin{pmatrix} -\vec{\nabla} \cdot (\vec{v}_0 & 0 \\ 0 & -\vec{v}_0 \cdot \nabla - (\nabla \vec{v}_0) \cdot \end{pmatrix} \begin{pmatrix} u_0 \\ \vec{u} \end{pmatrix} \\ &= \alpha \begin{pmatrix} u_0 \\ \vec{u} \end{pmatrix} + \beta \begin{pmatrix} u_0 \\ \vec{u} \end{pmatrix} \end{aligned} \quad (\text{D-4})$$

This is equivalent to

$$\frac{\partial U}{\partial t} = \alpha U + \beta U \quad (\text{D-5})$$

Let $U_\alpha e^{-i\omega_\alpha t}$ satisfy $-i\omega_\alpha U_\alpha = \alpha U_\alpha$. If β is a small perturbation, then $U e^{-i\omega t}$ satisfies equation (D-5) to first order if we add a perturbation term, i.e. let

$$U = (U_\alpha + \delta U) e^{-i(\omega_\alpha + \Delta \omega) t} \quad (\text{D-6})$$

Substituting this into equation (D-5) leads to

$$-i \Delta \omega U_\alpha - i \omega_\alpha \delta U = \alpha \delta U + \beta U_\alpha \quad (\text{D-7})$$

The second order terms have already been dropped in equation (D-7).

Using the scalar product with U_α^* in (D-7) and our boundary conditions,

$$\vec{u} \cdot d\vec{s} = 0 \quad (D-8)$$

where $d\vec{s}$ = element of arc length but with direction of outward normal to boundary. After algebra, we finally have :

$$\begin{aligned} \Delta \omega = \frac{1}{\int u_0 u_0^* da} \left\{ \int u_0^* \vec{v}_0 \cdot \nabla u_0 da - \frac{ih_0 g}{2\omega_0^2} \int (\nabla u_0^* \times \nabla u_0) \cdot (\nabla \times \vec{v}_0) da \right. \\ \left. + \frac{ih_0 g}{2\omega_0^2} \oint (\vec{v}_0 \cdot \nabla u_0) \nabla u_0^* \cdot d\vec{s} \right\} \end{aligned} \quad (D-9)$$

Where the first two integrals inside of brackets are integrated over the inner surface of the cell, and the last one in the brackets is integrated around the perimeter enclosing the cell area.

If $u_0 = J_m(k_{nm} r) e^{im\phi}$ and $\vec{v}_0 = v_0(r) \hat{\phi}$, we have

$$\begin{aligned} \Delta \omega = \frac{m}{\int J_m^2 da} \left\{ \int J_m^2 \frac{v_0(r)}{r} da - \frac{h_0 g}{2\omega_0^2} \int 2 \frac{J_m dJ_m}{r dr} \hat{z} \cdot (\nabla \times \vec{v}_0) da \right. \\ \left. + \frac{h_0 g}{2\omega_0^2} \oint v_0(r) \frac{J_m dJ_m}{r dr} \hat{r} \cdot d\vec{s} \right\} \end{aligned} \quad (D-10)$$

If the flow field is

$$v_0(r) = v_0(a) \frac{a}{r} \quad (D-11)$$

then $\vec{\nabla} \times \vec{v}_0 = 0$ anywhere except at the origin. The third sound cell geometry has no origin because we have a hole in the center of the cell. So we can ignore the second integral in equation (D-10). The line integral in the equation (D-10) can be evaluated by substituting in our boundary condition. So the integral is zero at the $r = a$ circle required by the boundary condition

$$\frac{dJ_m}{dr} = 0; \text{ the integral is}$$

$$-2\pi a v_0(a) \lim \left[\frac{J_m dJ_m}{r dr} \right] = -\frac{1}{2} \pi k_{nm}^2 a v_0(a) \delta_{m1} \quad (\text{D-11a})$$

this equation hold for r goes to zero, around the perimeter of a little hole at the center of the cell. This term is not zero only for the (1,1) mode after taking a limit.

The final result of equation (D-10) is

$$\frac{\Delta \omega}{\omega_0} = \frac{v_0(a)}{C_3} \frac{2m X_{nm}}{(X_{nm}^2 - m^2) J_m^2(X_{nm})} \left[\int_0^{X_{nm}} \frac{J_m^2(x)}{x} dx - \frac{1}{8} \delta_{m1} \right] \quad (\text{D-12})$$

where $X_{nm} = k_{nm} a$. If the flow field describes solid body rotation, then

$$v_0(r) = \omega_u r \quad (\text{D-13})$$

where ω_u is the solid body rotation frequency. The third integral in the brackets of equation (D-10) yields zero at this case when the boundary conditions are applied. The second integral, however, is not zero because of

$$\vec{V} \times \vec{v}_0 = 2 \omega_u \hat{z} ; \quad (D-14)$$

substituting (D-14) into (D-10) and solving for $\Delta \omega$, we have

$$\Delta \omega = \left[1 - \frac{2}{X_{nm}^2 - m^2} \right] m \omega_u \quad (D-15)$$

The total frequency shift due to the circulation and solid body rotation is

$$\frac{\Delta \omega}{\omega_0} = \gamma_{nm} X_{nm} \frac{v(a)}{a} \left[1 - \frac{2}{X_{nm}^2 - m^2} \right] m \omega_u \quad (D-16)$$

One point I have to make here is that we had originally calculated this perturbation a slightly different way. Our original calculation differs from Dr. Baierlein's in the last term in equation (D-12). We have $-0.150 \delta_{m-1}$ instead of $-0.125 \delta_{m-1}$ which he has. The main reason for this difference is that we dropped off the second order terms before we did the perturbation where as in reference [D.1], this was done after. Although the two results are similar, I tend to believe his results and have used it in the analysis presented in this thesis.

Appendix E

Data Taking and Fitting Programs

Appendix E gives all programs used for taking data and data analyses in this work. For a complete description of these programs, please see the comments at the beginning of the programs.

```

C*****
C  THIS IS THE FITTING FUNCTION USED BY A LEAST-SQUARES
C  FITTING ROUTINE. PASSED VALUE OF I IS USED TO FLAG THE REAL
C  OR COMPLEX PART SINCE THE FITTING ROUTINE IS NOT SET UP
C  FOR COMPLEX DATA TYPES. THE FUNCTION IS THAT OF A MASS
C  ON A SPRING ASSUMING EXP(-iWT) TIME DEPENDENCE.
C*****

```

```

      FUNCTION FUNCTN(X,I,A)
      IMPLICIT REAL*8 (A-H,P-Z)
      DIMENSION X(200),A(10)
      COMMON NPTS

```

```

      IF (2*I.GT.NPTS) THEN

```

```

C  IMAGINARY PART

```

```

      PHI=A(4)-1.5707863
      FUNCTN=A(6)
      ELSE

```

```

C  REAL PART

```

```

      PHI=A(4)
      FUNCTN=A(5)
      ENDIF

      U=2*A(2)*(1-X(I)/A(1))
      FUNCTN=FUNCTN+A(3)*(U*COS(PHI)-SIN(PHI))/(U+1)

      RETURN

```

END

```
C *****
C SUBROUTINE FDERIV(X,I,A,DELTA,NTERMS,DERIV)
C IMPLICIT REAL*8 (A-H,P-Z) DIMENSION X(200), A(NTERMS),
C DELTAA(NTERMS),DERIV(NTERMS) COMMON NPTS
C *****
      IF(DELTA(1).NE.0) THEN

C NUMERIC DERIVATIVE

      DO J=1,NTERMS
        A(J)=A(J)+DELTA(J)
        FPLUS=FUNCTN(X,I,A)
        A(J)=A(J)-DELTA(J)
        DERIV(J)=(FPLUS-FUNCTN(X,I,A))/DELTA(J)
      ENDDO
      ELSE

      IF (2*I.GT.NPTS) THEN

C IMAGINARY PART

        PHI=A(4)-1.5707863
        DERIV(5)=0
        DERIV(6)=1
      ELSE

C REAL PART

        PHI=A(4)
```

```

DERIV(5)=1
DERIV(6)=0
ENDIF

FMU=1-(X(I)/A(1))
U=2*A(2)*FMU
FDEN=U*U+1
DFDU=2*A(3)*((2-FDEN)*COS(PHI)+2*U*SIN(PHI))/FDEN**2

DERIV(1)=DFDU*A(2)*X(I)/A(1)**2
DERIV(2)=DFDU*FMU
DERIV(3)=(U*COS(PHI)-SIN(PHI))/FDEN
DERIV(4)=A(3)*(-U*SIN(PHI)-COS(PHI))/FDEN

END IF
RETURN
END

```

```

C*****
C  A PROGRAM USED TO FIND PARAMETERS OF THE ROTATIONAL
C  DRIVE CRESPONSE FUNCTION BY MINIMIZING THE MEAN
C  SQUARE DIFFERENCES BETWEEN THE DATA OBTAINED FROM
C  FITS TO THE RESONANCES AND POINTS CALCULATED FROM
C  THE RESPONSE FUNCTION SCALC. BOTH DATA AND
C  CALCULATIONS ARE COMPLEX.
C  THE PROGRAM USES MINIMIZATION ROUTINE "AMOEBA"
C  FROM NUMERICAL RECIPES, P.292
C
C                      LAST MODIFIED 7/92
C*****

```

```

      PROGRAM FLIPFIT
      IMPLICIT REAL*8 (A-H,O-Z)
      COMMON NDIM,SZ,M
      DIMENSION P(10,10),Y(10)
      DIMENSION A(10),B(10),SZ(10)
      COMPLEX*8 SCALC,SIGC
      COMPLEX*8 SIGDAT(-1:1,-1:1)

C  GET INITIAL PARAMETERS - LOOP TERMINATED BY ^Z

      INPAR=1
      DO WHILE(INPAR.EQ.1)

      TYPE 7,'INPUT AMPLITUDE, THETA, AND PHI > '
7      FORMAT('$',A)
      READ(*,*,END=1)(A(I),I=1,NDIM)

C  CHECK VALUE

      FVAL=FUNK(A)

```

```

        FVAL=SQRT(FVAL-1)/2
        TYPE*, ' FUNCTION= ',FVAL
        TYPE*
    END DO

C    FILL UP P ARRAY WITH CUBICAL SIMPLEX BASED ON GUESSED
C    POINT Y GETS THE FUNCTION VALUES AT THOSE POINTS.

1      DO I=1,NDIM+1
        DO J=1,NDIM
            IF(J.EQ.I)THEN
                P(I,J)=A(J)+SZ(J)
            ELSE
                P(I,J)=A(J)
            END IF
            B(J)=P(I,J)
        END DO
        Y(I)=FUNK(B)
C    TYPE*,I,Y(I)
    END DO

        FTOL=(A(1)/1000.)**2
        TYPE*,FTOL
        ITER=0

        CALL AMOEBA(P,Y,NDIM,FTOL,ITER)

C    PRINT RESULTS (SMALLEST OF THE SIMPLEX POINTS)

        MIN=1

```

```

DO I=1,NDIM+1
IF(Y(I).LT.Y(MIN))MIN=I
END DO

```

```

DO I=1,NDIM
    A(I)=P(MIN,I)
END DO

```

C DON'T ALLOW NEGATIVE DELTA...

```

IF(COS(A(2)).LT.0)THEN
    A(2)=3.1415926-A(2)
    A(3)=A(3)+3.1415926
END IF

```

C REDUCE ANGLES TO -PI TO PI

```

A(2)=REDUCE(A(2))
A(3)=REDUCE(A(3))

```

```

DO I=1,NDIM
    TYPE 2,I,A(I)
2      FORMAT('  A(',I2,')=',1PE10.2)
END DO
DO IP=-1,1,2
    DO IQ=-1,1,2
        SIGC=SCALC(A(1),A(2),A(3),IP,IQ,M)
        WRITE(*,10)IP,IQ,SIGC
10     FORMAT(2X,2I5,2X,F10.4,2X,F10.4)
    END DO
END DO

```

```

        TYPE*
        FVAL=SQRT(Y(MIN)-1)/2
        TYPE*,'FUNCTION VALUE=',FVA
    STOP
END

```

```

C*****
C    FUNCTION TO BE MINIMIZED. A(I) ARE THE FUNCTION'S
C    PARAMETERS, AND SZ(I) SHOULD BE ROUGHLY THE
C    CHARACTERISTIC LENGTH SCALE FOR EACH PARAMETER. SET
C    NDIM TO HOW MANY PARAMETERS ARE USED. IN THIS CASE,
C    THREE PARAMETERS ARE USED: A(1)=AMP, RELATED TO THE
C    OVERALL STRENGTH OF THE RESONANCES; A(2)=THE, THE RATIO
C    OF THE CIRCULATION TO TOTAL SHIFT; AND A(3)=PHI, THE
C    GEOMETRICAL CIRCUMMETRY ORIENTATION. THE DATA IS IN A
C    FILE SIGDAT. DAT AND FUNCTION SCALC IS THE THEORETICAL
C    RESULT.
C*****

```

```

        REAL*8 FUNCTION FUNK(A)
        IMPLICIT REAL*8 (A-H,O-Z)
        COMMON NDIM,SZ,M
        COMPLEX*8 SIGC,SIGD
        COMPLEX*8 SCALC
        COMPLEX*8 SIGDAT(-1:1,-1:1)
        DIMENSION A(10),SZ(10)
        DATA NDIM,SZ/3,1,1,1,1,7*1./
        DATA IFIRST/1/

```

```

C    READ IN DATA THE FIRST TIME CALLED

```



```
IF(IFIRST.EQ.1)THEN
```

```
OPEN(1,FILE='SIGDAT.DAT',STATUS='OLD',CARRIAG  
ECONTROL='LIST')
```

```
READ(1,*)M
```

```
DO IP=-1,1,2
```

```
DO IQ=-1,1,2
```

```
READ(1,8)SIGDAT(IP,IQ)
```

8

```
FORMAT(2F10.3)
```

```
END DO
```

```
END DO
```

```
IFIRST=0
```

```
CLOSE(1)
```

```
END IF
```

```
AMP=A(1)
```

```
THE=A(2)
```

```
PHI=A(3)
```

C SUM UP THE ABSOLUTE ERRORS

```
FUNK=0
```

```
DO IP=-1,1,2
```

```
DO IQ=-1,1,2
```

```
SIGC=SCALC(A(1),A(2),A(3),IP,IQ,M)
```

```
SIGD=SIGDAT(IP,IQ)
```

```
FUNK=FUNK+CABS(SIGD-SIGC)**2
```

```
END DO
```

```
END DO
```

```
FUNK=FUNK+1
```

```
RETURN
```

END

C THIS FUNCTION REDUCES ANGLES TO -PI TO PI

REAL*8 FUNCTION REDUCE(X)

IMPLICIT REAL*8 (A-Z)

PARAMETER (PI=3.14159265,TPI=6.28318531)

DO WHILE(X.LE.-PI)

X=X+TPI

END DO

DO WHILE(X.GT.PI)

X=X-TPI

END DO

REDUCE=X

RETURN

END

C*****

C THIS FUNCTION RETURNS CALCULATED VALUES FOR THE
C COMPLEX RESONANT AMPLITUDE FOR A ROTATIONAL DRIVE.
C AMP=AMPLITUDE CIRCULATION=(TOTAL SHIFT)*SIN(THE)
C GEOMETRIC SHIFT=(TOTAL SHIFT)*COS(THE) PHI=GEOMETRIC
C ASYMMETRY SPACIAL PHASE IP=+1/-1 FOR UPPER/LOWER
C MODE IQ=+1/-1 FOR RIGHT/LEFT DRIVE M=1,2,3... MODE M
C VALUE

C SEE H. LUO, 1992.

COMPLEX*8 FUNCTION SCALC(AMP,THE,PHI,IP,IQ,M)
IMPLICIT REAL*8 (A-H,O-Z)

C ONLY ALLOW +/-1 FOR IQ, IP

IF ((ABS(IP).NE.1).OR.(ABS(IQ).NE.1)) THEN
SCALC=CMPLX(0, 0)
RETURN
END IF

K=(M-1)/2

IF (MOD(K,2).EQ.0) THEN
SGK=1.
ELSE
SGK=-1.
END IF

IF (MOD(M,2).EQ.1) THEN

C ODD M VALUES...

C=IP*(IP+IQ*SGK*SIN(THE)+COS(THE)*COS(PHI))
D=IP*(-COS(THE)*IQ*SGK*SIN(PHI))
SCALC=CMPLX(C*AMP,D*AMP)

ELSE

C EVEN M VALUES...

C=1.+COS(THE)*COS(PHI)

```
        SCALC=CMPLX(C,C*SGK*IQ)
        SCALC=(0, 0)
    END IF
```

C FIX UP COMMON FACTOR OF 1 OR i...

```
        IF (IQ.EQ.-1) SCALC=CMPLX(0,1.)*SCALC
```

```
        RETURN
```

```
    END
```

References

Chapter 1

- [1.1] J. Wilks, The Properties of Liquid and Solid Helium. (Oxford University Press 1967)
- [1.2] K. R. Atkins, Liquid Helium. (Cambridge University Press, 1959)
- [1.3] W.E. Keller, Helium - 3 and Helium - 4. (New York, 1969)
- [1.4] J. F. Allen and H. Jones, *Nature* 141 , 243 (1938)
- [1.5] E. Zaremba, W. Kohn, *Phys. Rev. B* 13 , 2270 (1976)
- [1.6] J. G. Brisson II , Third Sound Studies of Helium on Molecular Hydrogen , Ph. D. thesis. (Harvard University, 1990)
- [1.7] L. D. Landau, *J. Phys. Moscow*, 5 , 71 (1941)
- [1.8] W. F. Vinen, *Proc. Roy. Soc. A* 260 , 218 (1961)
- [1.9] D. E. Rutherford, Fluid Dynamics , Section 24, (Oliver and Boyd, 1959)
- [1.10] S. C. Whitmore, W. Zimmermann, *Phys. Rev. Lett.* 15 , 389 (1965)
- [1.11] J. B. Mehl and W. Zimmerman, Jr., *Phys. Rev. Lett.* 14 , 815 (1965)
- [1.12] J. D. Reppy and D. Depatie, *Phys. Rev. Lett.* 12 , 187 (1964)
- [1.13] W. M. Van Alphen, R. deBruyn Ouboter, *Physica* 39 , 109 (1968)
- [1.14] R. P. Henkel, G. Kukich and J.D. Reppy in Proc. of the 11th International Conference on Low Temp. Phys. , J. F. Allen etc. eds. (Univ. of St. Andrews Press, St. Andrews, Scotland, 1968)
- [1.15] F. Wagner, *J. Low Temp. Phys.* 13 , 185 (1973)
- [1.16] T. G. Wang and I. Rudnick in Proc. of the 13th International Conference on Low Temp. Phys. W. J. O'sullivan, K. D. Timmerhaus and E. F. Hammel, eds. (Plenum, New York, 1974)

- [1.17] M. Kim and W. I. Glaberson in Proc. of the 17th International Conference on Low Temp. Phys. U. Eckern, A. Schmid etc. eds. (Elsvier Science Publisher B. V. 1984) P. 299
- [1.18] W. F. Vinen, Proc. Roy. Soc. (london) A260 , 218 (1961)

Chapter 2

- [2.1] L. Tisza, Nature, 141 ,913 (1938)
- [2.2] L. D. Landau, J. Phys. Moscow 5 , 71 (1941)
- [2.3] J. Brooks, R. Donnelly, J. Phys. Chem. Ref. Data 6 , #1 (1977)
- [2.4] F. London, Phys. Rev. 54 , 947 (1938); F. London, Nature 141 , 663 (1938)
- [2.5] J. C. Findlay, A. Pitt, H. Grayson-smith and J. O. Wilhelm, Phys. Rev. 54 , 506 (1938)
- [2.6] D. R. Tilley, J. Tilley, Superfluidity and Superconductivity , Second Edition (University of Sussex Press, 1986)
- [2.7] K. R. Atkins, Phys. Rev. 113 , 962 (1959)
- [2.8] I. Rudnick, K. A. Shapiro, Phys. Rev. Lett. 9 , 191 (1962)
- [2.9] D. R. Tilley, J. Tilley, Superfluidity and Superconductivity , Second Edition (University of Sussex Press, Chapter 6.5 1986)
- [2.10] K. R. Atkins, Can. J. Phys. 31 , 1165 (1953)
- [2.11] K. R. Atkins, Phys. Rev. 113 , 962 (1959)
- [2.12] E. Sabisky, C. Anderson, Phys. Rev. A 7 , 790 (1973)
- [2.13] L. Landau, E. Lifshitz, Statistical Physics , Third Edition, Part 2, (Pergamon Press, New York (1980)
- [2.14] D. R. Tilley, J. Tilley, Superfluidity and Superconductivity , Second Edition (University of Sussex Press 1986)
- [2.15] L. Landau, E. Lifshitz, Fluid Mechanics , Second Edition (Pergamon Press, New York 1980)

- [2.16] I. Khalatnikov, Introduction to the Theory of Superfluidity ,
(Benjamin, New York 1965)
- [2.17] K. R. Atkins, I. Rudnick, Progress in Low Temp. Phys. , Vol. VI ,
Chapter 2, (North Holland Amsterdam 1970)
- [2.18] Private communication with Prof. F. M. Ellis.
- [2.19] D. J. Bergman, Phys. Rev. A 3 , 2058 (1971)

Chapter 3

- [3.1] F. M. Ellis, R. B. Hallock, Rev. Sci. Instrum. 54 , 751 (1983)
- [3.2] S. Voltz, K. Gillis and J. M. Mochel, Rev. Sci. Instrum. 56 , 444
(1985)
- [3.3] T. Wang, I. Rudnick, in Proc. of the 13th International Conference
on Low Temp. Phys. (LT-13) , (Plenum, New York, 1974)
- [3.4] M. Kim, W. I. Glaberson, in Proc. of the 17th International
Conference on Low Temp. Phys. (LT-17) , (North-Holland,
Amsterdam, 1984)
- [3.5] J. Markus, I. Rudnick, Physica B 107 , 409 (1981)

Chapter 4

- [4.1] S. J. Putterman, Superfluid Hydrodynamics , (North Holland /
American Elsevier, 1974)

Chapter 5

- [5.1] See Todd S. Holbrook, Unpublished thesis, Wesleyan University.
(1989)
- [5.2] G. K. Walters and W. M. Fairbank, Phys. Rev. 103 , 262 (1956)

- [5.3] H. London, G. R. Clarke and E. Mendoza, Phys. Rev. 128 , 1992 (1962)
- [5.4] F. M. Ellis and H. Luo, Phys. Rev. B, 39 , 2703 (1989)
- [5.5] C. W. F. Everitt, K. R. Atkins and A. Denenstein, Phys. Rev. 136 , A1494 (1964)
- [5.6] I. Rudnick, R. Kagiwada, J. Fraser and E. Guyon, Phys. Rev. Lett. 20 , 430 (1968)
- [5.7] J. Brooks, F. M. Ellis and R. B. Hallock, Phys. Rev. Lett. 40 , 240 (1978)
- [5.8] Van Degrift, Rev. Sci. Instrum. , 46 , 599 (1975). F. M. Ellis, J. S. Brooks and R. B. Hallock, Rev. Sci. Instrum. , 52 , 1051 (1981)

Chapter 6

- [6.1] K. L. Telschow, R. B. Hallock, Phys. Rev. B 27 , 3068 (1983)
- [6.2] R. P. Henkel, E. N. Smith and J. D. Reppy, Phys. Rev. Lett. 23 , 1276 (1969)
- [6.3] Todd Holbrook, M.A. Thesis, Wesleyan University, (1989)

Appendix

- [A.1] F. M. Ellis, Ph. D. Thesis, University of Massachusetts at Amherst, (1983)
- [D.1] See the calculation made by Dr. Ralph Baierlein.